HOKKAIDO UNIVERSITY

Title	Structural Analysis of Novel Halogen-Rich Argyrodite and Verifying the Applicability as a Solid Electrolyte for All-Solid-State Batteries
Author(s)	増田, 直也
Degree Grantor	北海道大学
Degree Name	博士(工学)
Dissertation Number	甲第16386号
Issue Date	2025-03-25
DOI	https://doi.org/10.14943/doctoral.k16386
Doc URL	https://hdl.handle.net/2115/94874
Type	doctoral thesis
File Information	MASUDA_Naoya.pdf

Hokkaido University Collection of Scholarly and Academic Papers : HUSCAP

Structural Analysis of Novel Halogen-Rich Argyrodite and Verifying the Applicability as a Solid Electrolyte for All-Solid-State Batteries

Naoya Masuda

February 2025

Doctoral Thesis at Hokkaido University

Structural Analysis of Novel Halogen-Rich Argyrodite and Verifying the Applicability as a Solid Electrolyte for All-Solid-State Batteries

Contents

1. General introduction

1.1 Background

Over the years, various high-performing lithium-ion rechargeable batteries have been developed to address global warming [1] and realize a sustainable carbon-neutral society [2]. The demand for these batteries over the next 10 years is expected to grow intensively. Under this circumstance, the development of safer lithium-ion batteries with higher energy density is required because current commercialized lithium-ion batteries generally consist of flammable liquid electrolyte. The flammability of the liquid electrolyte is the main factor causing low safety of the current commercialized batteries. In case of electric vehicle, this flammability also limits the design of battery package. To ensure vehicle safety, it is necessary to install a cooling system, which limits the ability to improve energy density.

All-solid-state lithium-ion batteries are considered a promising next-generation solution [3, 4] to deliver more energy than that of their conventional counterparts comprising liquid electrolytes and more safety due to comprising of non-flammable solid electrolyte [3, 4]. All-solid-state batteries contain a cathode, anode, and solid electrolyte (SE). Their properties depend mostly on the characteristics of the SE [5]. Unfortunately, these batteries have low-rate capabilities and energy densities, partly because of the lack of suitable SEs that exhibit higher ionic conductivities than those of liquid electrolytes [6]. Recently both oxide and sulfide SEs have been reported as candidate materials for all-solid-state batteries.

In the oxide SEs, perovskite-type $Li_{0.34}La_{0.51}TiO_{2.94}$ [7], sodium-superionic conductor (NASICON)-type $Li_{1.5}Al_{0.5}Ge_{1.5}(PO_4)_3$ [8] and garnet-type $Li_7La_3Zr_2O_{12}$ [9] have been reported to exhibit high lithium-ion conductivity around 10^{-5} S/cm. Some garnet-type

solid electrolytes with Zr^{4+} partially replaced by Ta^{5+} or Li^{+} partially replaced by Ga^{3+} have the high lithium-ion conductivity of around 10^{-3} S/cm [10, 11] close to that of liquid electrolytes (~10^{-2} S/cm). To utilize the oxide SEs practically, the high sintering temperature is required. This sintering process limit the application of oxide SEs to scalable all-solid-state batteries. Low ionic conductivity of oxide SEs also limit the application to the all-solid-state batteries up to now. On the other hand, recent studies on sulfide SEs have shown that batteries containing SEs comprising phosphorus sulfide are promising [12] for scalable all-solid-state batteries because of their higher ionic conductivities,[13] mechanical softness,[14] and facile processing without high-temperature sintering.[15]

The development of sulfide SEs began almost 40 years ago. The initial reports of ionic conductivity in sulfide SEs were glassy Li_2S-GeS_2, Li_2S-P_2S_5-LiI and Li_2S-SiS_2 showing conductivities in the range of 10^{-4} S/cm at room temperature [16-22]. Since then, novel sulfide SEs have been reported around the world. There are mainly three types of SE, the first type is Li_2S-P_2S_5-based material, the second type is $Li_{10}GeP_2S_{12}$-based material, and the third type is argyrodite-based material.

1.2 Li_2S-P_2S_5-based SEs

In the Li_2S-P_2S_5 system, SEs have conventionally synthesized by mechanical milling of Li_2S and P_2S_5 and subsequent heat treatment. After sintering, the mixtures of amorphous and crystal are obtained. These mixtures of glass and ceramics (GC) showed high ionic conductivity. Specifically, $Li_7P_3S_{11}$ exhibited high ionic conductivity (3.2 mS/cm) [23-26]. Among this system, Li_3PS_4 have also been studied as well as $Li_7P_3S_{11}$. Li_3PS_4 is comprised of PS^{4-} tera-hedra and have several different crystal structures depending on the orientation of this tetra-hedra. Whereas γ- Li_3PS_4 shows low ionic conductivity ($3\times10^{-}$

^{7} S/cm), β-Li3PS4 shows relatively high ionic conductivity (10^{-4} – 10^{-3} S/cm). In case of α- Li_3PS_4, this crystal structure is only stable at higher than 746 K and shows high ionic conductivity [24, 27-29].

Ionic substitutions have been employed in the Li_2S-P_2S_5 system to enhance the ionic conductivities. As the cation substitutions, Ni, Sn, Mo and As have been selected to substitute with P in Li_2S-P_2S_5 system and improved ionic conductivity [30-33]. As the anion substitutions, I and Se have been substituted. [34-37]. Both cations and anions substitution also have been employed in 0.4LiI-0.6Li_4SnS_4 [38] to enhance the ionic conductivity.

1.3 $Li_{10}GeP_2S_{12}$-based SEs

$Li_{10}GeP_2S_{12}$-based SEs have been investigated and inspired from crystalline thio-lithium supeionic conductor (thio-LISICON) type SEs in the Li_4GeS_4-Li_3PS_4 system. This type of sulfide SEs have been investigated with the concept of high-polarizing anions with sulfur, which are more favorable than oxides in enhancing lithium-ion conductivity. In 2001, crystalline thio-LISICON type SE in the Li_4GeS_4-Li_3PS_4 system was investigated and showed high ionic conductivity (2.2 mS/cm) [39]. After several studies [40-44], crystalline $Li_{10}GeP_2S_{12}$ (LGPS) type SE with high ionic conductivity (12 mS/cm) was reported in 2011 [45]. Maximum entropy method (MEM) analysis revealed that lithium ions conduct pseudo 1-dimensionally along c-axis [45]. Ionic substitutions have been employed in LGPS type to enhance the ionic conductivity. Si and Cl substituted LGPS type SE ($Li_{9.54}Si_{1.74}P_{1.44}S_{11.7}Cl_{0.3}$) showed highest ionic conductivity (25 mS/cm) in 2016 [4]. The MEM calculations showed that the lithium ions conduct 3-dimensionally within a unit cell. The ionic conductivity of $Li_{9.54}Si_{1.74}P_{1.44}S_{11.7}Cl_{0.3}$ was enhanced due to the

extended lithium-ion conduction path different from that of LGPS.

Other ionic substitutions have been employed intensively after the investigation of LGPS to enhance the ionic conductivity, resulting in the enhanced performance of all-solid-state batteries [46-64].

1.4 .1 introduction of argyrodite-based SEs

Argyrodite structures, such as quenched Ag_8TiS_6 [65] and Cu_8GeS_6 [66] with cubic structure [66, 67], have been investigated due to high ionic conductivities. It had previously reported that Ag_7AlSe_6 with a cubic lattice at high temperature showed high ionic conductivity due to randomly distributed Ag with site vacancy [68]. This report suggested high Ag^+ and Cu^+ conductivity in many argyrodite with a cubic structure. Deiseroth et al. have extended this idea to investigate novel high lithium-ion conductors with cubic argyrodite structure. They have reported in 2008 [69] that halogen-substituted argyrodite Li_6PS_5X (X=Cl, Br and I) exhibited high ionic conductivity (~10^{-3} S/cm) with cubic structure at room temperature. Because Li_7PS_6 with cubic structure is only stable at high temperature [70], they synthesized stable cubic argyrodites at room temperature by substituting Li_7PS_6 with halogen species. Hereafter, the argyrodite is denoted as $Li_{7-\alpha}(PS_4)(S_{2-\alpha}X_\alpha)$ to distinguish the sulfide anions that form the PS_4 tetrahedra from those present at the 4a and 4d sites (Figure 1). To enhance the ionic conductivity further, ionic substitutions and quenching method have been employed in $Li_7(PS_4)(S_2)$-based system. However, fundamental crystal structure of cubic argyrodite is still unknown [71]. For example, the reported crystal structure of $Li_{6.0}(PS_4)(S_{1.0}Cl_{1.0})$ was unambiguous, because it is difficult to quantify the lithium amount and site by XRD [72] and it is also known that separating S and Cl in the same Wyckoff site is challenging [73,74]. Conventionally,

Cl/S is considered as psedo-single atom in the mixed anion system [73,74]. Furthermore, the constraint of lithium occupancy is not precise in Rietveld refinement. If the amount of lithium is calculated from this refined data, the composition should be $Li_{6.94}(PS_4)(S_{1.0}Cl_{1.0})$. But the composition from this constraint is contradict to the composition of $Li_{6.0}(PS_4)(S_{1.0}Cl_{1.0})$.

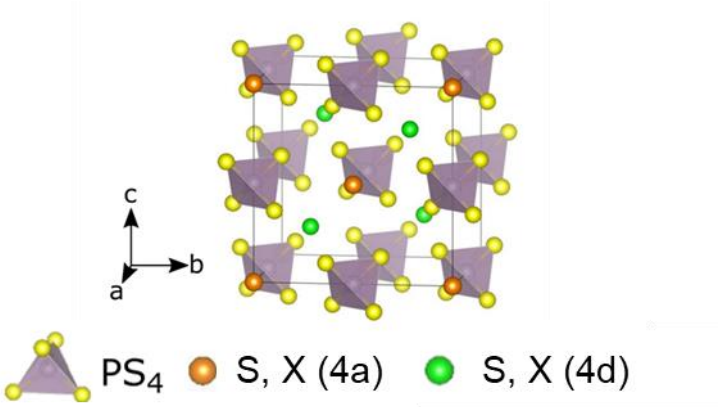

Figure 1. The framework structure of cubic argyrodite. Lithium should be distributed between above structure, but still not clear where lithium should be located.

Table 1. Reported Rietveld refinement result of $Li_{6.0}(PS_4)(S_{1.0}Cl_{1.0})$.

Atom	Fractional coordinates			Wyckoff	Occupancy	U_{iso}
	X	Y	z			($Å^2$)
Li	0.1761	0.1761	0.0217	48*h*	0.5784	0.1360
P	0. 5	0.5	0.5	4*b*	1.00	0.0344
S(0)	0.6220	0.6220	0.6220	16*e*	1.00	0.0488
S(1)	0.25	0.25	0.25	4*c*	0.4938	0.0352
Cl(1)	0.25	0.25	0.25	4*c*	0.5062	0.0352
S(2)	0.0	0.0	0.0	4*a*	0.6493	0.0400
Cl(2)	0.0	0.0	0.0	4*a*	0.3507	0.0400

1.4.2 Ionic substitution in $Li_{7(}PS_4)S_2$-based system

The substitution of both cations and anions have been employed in $Li_7(PS_4)(S_2)$-based system to enhance the ionic conductivity. For cation substitutions, Al, B, Si and Ge have been selected [75] to substitute with P in the 4b site of $Li_7(PS_4)(S_2)$. By increasing the amount of substituted cations, the primitive lattice changed from orthorhombic phase to cubic phase gradually. These phase transitions caused by cation substitutions enhanced ionic conductivities of these materials. Among these materials, $Li_{7.3(}Ge_{0.3}P_{0.7}S_4)S_2$ showed highest ionic conductivity (2 mS/cm) with cubic argyrodite structure. As another cation substitutions, Fe has been selected to substitute with Li in $Li_7(PS_4)(S_2)$. By changing the amount of substituted Fe, crystal structure changed from orthorhombic to cubic and enhanced ionic conductivity up to 0.14 mS/cm, which is higher than that of cubic $Li_7(PS_4)(S_2)$ (about 0.01 mS/cm) [76].

For anion substitutions, Se, Cl, Br and I have been utilized for substitution. $Li_{6.0}(PS_4)(S_{1.0}X_{1.0})$ (X=Cl, Br and I) and $Li_6(PS_4)(S_{1.0-x}Se_x)I$ showed high ionic conductivities [77-80] having cubic structure at room temperature. Unfortunately, $Li_7(PSe_4)Se_2$ have orthorhombic crystal structure at room temperature which is the same as $Li_7(PS_4)(S_2)$ at room temperature, resulting in low ionic conductivity at room temperature [70, 81].

Other ionic substitutions have been employed intensively after the first report of halogen-substituted cubic argyrodite $Li_{6.0}(PS_4)(S_{1.0}X_{1.0})$ (X=Cl, Br and I). Both cation and anion substitutions [$Li_{6.6}(Si_{0.6}Sb_{0.4}S_4)(S_{1.0}I1_{1.0})$, $Li_{6.6}(P_{0.4}Ge_{0.6}S_4)(S_{1.0}I_{1.0})$ and $Li_{6.5}(Sb_{0.5}Ge_{0.5})(S_{1.0}I_{1.0})$, etc.] have been employed to enhance the ionic conductivities up to 18.4 mS/cm.[82-84].

1.4.3 Quenching enhanced ionic conductivity in $Li_{6.0}(PS_4)(S_{1.0}Br_{1.0})$

Quenched $Li_{6.0}(PS_4)(S_{1.0}Br_{1.0})$ after sintering using liquid N_2 showed high ionic conductivity (2 mS/cm) compared to the same composition sample with slow-cooling treatment (0.5 mS/cm). Quenched samples have random distribution of Br/S at 4a and 4d site confirmed by neutron powder diffraction. The Br/S ions preferably occupied randomly in 4a and 4d site, as the cooling rate increased. The Li ions occupied several sites (48h, 24g, 48h') around 4d site like cage structure in these materials. The long-range Li conduction happened when Li conducted from the 48h' site in the cage to the 48h' site in the neighbor cage via 24g and 48h site by MEM analysis. It is not yet revealed but experimental data showed the randomness of anion distribution in $Li_{6.0}(PS_4)(S_{1.0}Br_{1.0})$ triggered short conduction path between cages, resulting in high ionic conductivity. [85, 86]

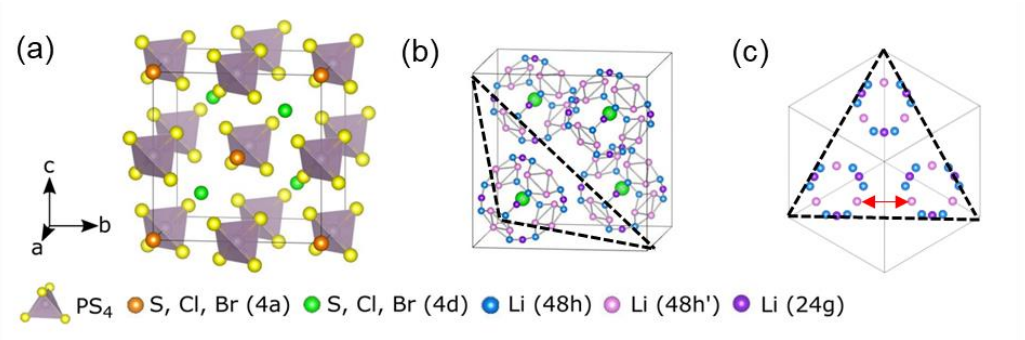

Figure 2. (a) The framework structure of cubic argyrodite. (b) Lithium and 4d site are illustrated in cubic argyrodite structure. (c) Corresponding (111) plane is extracted and displayed as a vertical view. Red arrow represents to the conduction path between cages.

1.4.4 Halogen-rich argyrodite

Among sulfur-based SEs having cubic argyrodite structure, recently halogen-rich argyrodites have exhibited high ionic conductivity. Especially, various compositions of a quasi-ternary system, $Li_7(PS_4)(S_2)$–$Li_5(PS_4)(Cl_2)$–$Li_5(PS_4)(Br_2)$, have been reported [6,

12-15, 81, 85-97]. However, the investigated compositions have highly limited ternary plots (Figure 3). Although $Li_{5.3}(PS_4)(S_{0.3}Cl_{1.0}Br_{0.7})$ [87] exhibits enhanced ionic conductivity (up to 24 mS/cm) (Figure 3), the composition required for the highest conductivity has not been investigated thus far. Therefore, investigating the composition of a ternary system to obtain a high lithium-ion conductivity remains an important research topic. In addition, the crystal structure and the Li-ion conduction mechanism in argyrodite is yet to be revealed; however, several researchers have proposed different crystal structures and different conduction paths[83, 85, 86, 98-103]. It is essential that the relationship between the lithium-ion conduction mechanism in argyrodite and the crystal structure is elucidated to understand the fundamental diffusion mechanism.

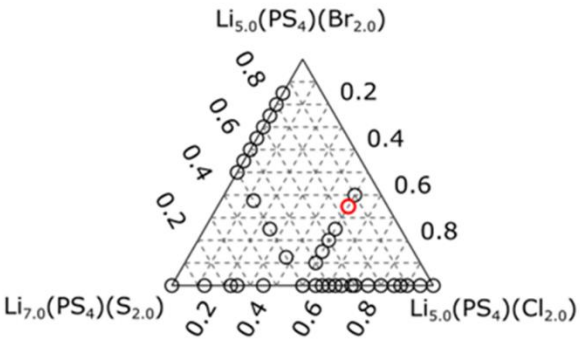

Figure 3. Open circles are investigated compositions in references. Ionic conductivities of these compositions are also reported. Red circle denotes composition with highest conductivity (24 mS/cm), $Li_{5.3}(PS_4)(S_{0.3}Cl_{1.0}Br_{0.7})$.[87]

1.5 The stability of sulfur-based SEs in the all-solid-state batteries and the enhancement of discharge capacity

The high stability of SE is necessary to enhance the performance of the all-solid-state batteries. Even if the ionic conductivity of SE is high, the poor stability of SE during cycling causes low capacity, high resistance and low durability[104-127]. The all-solid-state batteries consist of cathode, separator and anode. The stability of SE against cathode

active materials (CAMs) and carbon additive (CA) in cathode layer, the stability of SE within the voltage window during charge/discharge and the stability of SEs against anode are essential to enhance the performance of the all-solid-state batteries.

Among these stabilities of SE, especially in cathode layer, it had previously been reported that the stability of SE against CAM was calculated from impedance spectra of an all-solid-state battery using equivalent circuit model. Impedance spectra of Li−In | β-Li_3PS_4 | β-Li_3PS_4–$Li(Ni_{0.8}Co_{0.1}Mn_{0.1})O_2$ during cycling were fitted using the equivalent circuit of 4 parallel resistances and constant phase elements (CPE). From the fitting results, the interfacial resistance of CAM and SE corresponding to around 1000 Hz was extracted and compared the resistance increase at each cycle. The interfacial resistance of CAM and SE changed more drastically than other interfacial resistances in the same charge/discharge cycle. The interfacial resistance of CAM and SE also increased as cycle number increased, although other interfacial resistances are almost the same before and after cycling. The interfacial resistance of CAM and SE increased from 100 to 300 Ω during 2 cycles, however the bulk/grain boundary resistance of SE and the interfacial resistance of SE and anode are constant during 2 cycles. The reason of increased interfacial resistance is confirmed by X-ray photoelectron spectroscopy (XPS). The bridged P-S-P in $P_2S_7^-$ units and oxidic phosphorus were detected after 50 cycles, although there is no evidence of forming these materials before cycling. These results indicate that the stability of β-Li_3PS_4 against $Li(Ni_{0.8}Co_{0.1}Mn_{0.1})O_2$ is poor [128].

For the practical usage of all-solid-state battery, it is necessary to enhance the discharge capacity. Various attempts have been made on the cathode and anode side to enhance the capacity. Among these methods, especially for cathode side, the CAMs with wide operational voltage window [$Li(Ni_{0.8}Co_{0.1}Mn_{0.1})O_2$, $Li(Ni_{0.6}Co_{0.2}Mn_{0.2})O_2$, etc.] [128-

129] and adding CA to the cathode have been investigated [104-127]. Several studies have attempted to enhance the capacity of various sulfide solid electrolytes using a carbon additive (CA) to increase the electronic conductivity of the cathode [104-127]. The discharge capacity of the Li | β-Li_3PS_4 | $Li(Ni_{0.6}Co_{0.2}Mn_{0.2})O_2$–β-$Li_3PS_4$ battery increased with a CA-modified cathode. However, the capacity retention rate was ~85% after 50 cycles [108]. Similarly, the retention rate of the In-Li | $Li_{6.0}(PS_4)(S_{1.0}Cl_{1.0})$ | $Li(Ni_{0.6}Co_{0.2}Mn_{0.2})O_2$–$Li_{6.0}(PS_4)(S_{1.0}Cl_{1.0})$ battery was 79% after 50 cycles [127]. With a CA, the capacity decreased with repeated cycles, although the initial capacity was high [108]. The decreased capacity after cycling was likely related to a decomposition reaction of SE, although the mechanism remains unclear [131, 132]. These results showed that the capacity retention rate gradually decrease after cycling with a CA modification.

From these results, especially in cathode, the high stability of SE is desirable to enhance the capacity and cycle durability.

1.6 Objectives and outline of the thesis

The objectives of this thesis are to investigate the structure of novel halogen-rich argyrodite in a ternary system, $Li_7(PS_4)(S_2)$–$Li_5(PS_4)(Cl_2)$–$Li_5(PS_4)(Br_2)$, with high lithium-ion conductivity and elucidate the lithium conduction path inside crystal structure. Other objectives of this thesis are to examine the stability of novel argyrodite material inside all-solid-state battery and to enhance the capacity of all-solid-state battery comprising $Li(Ni_{0.8}Co_{0.1}Mn_{0.1})O_2$, novel argyrodite and lithium metal anode. The crystal structure of novel argyrodites were determined by the Rietveld refinement of Synchrotron X-ray diffraction and neutron diffraction. The lithium-ion conduction path in novel

argyrodites were investigated by analyzing bond valence sum (BVS) and maximum entropy method (MEM) of neutron diffraction. The stability of novel argyrodite in the all-solid-battery was examined by separating the stability in cathode layer, separator layer, and anode layer, respectively. The enhancement of discharge capacity was investigated using CA to the cathode by evaluating impedance spectra before and after cycling.

This thesis consists of 5 chapters as follows.

Chapter 1

The background, the objectives and the contents of this thesis are described in this chapter.

Chapter 2

The investigation of the crystal structure of novel halogen-rich argyrodite in a ternary system, $Li_7(PS_4)(S_2)$–$Li_5(PS_4)(Cl_2)$–$Li_5(PS_4)(Br_2)$, with high lithium-ion conductivity and the lithium conduction path in novel argyrodite structure are described in this chapter. The 44 compositions in a ternary system to obtain a high lithium-ion conductivity were examined. Both synchrotron X-Ray diffraction and neutron diffraction were measured among these compositions with high ionic conductivity to elucidate the crystal structure of novel argyrodite. Lithium conduction path of various compositions is calculated using BVS and MEM analysis. The stability of halogen-rich argyrodite against Li metal anode was investigated to confirm the potential of novel halogen-rich argyrodite for high-capacity battery. The cycling behavior of the all-solid-state battery comprising $Li(Ni_{0.8}Co_{0.05}Al_{0.15})O_2$, novel halogen-rich argyrodite and carbon anode was investigated to confirm that the battery performance using conventional active materials and novel

halogen-rich argyrodite.

Chapter 3

The stability of novel argyrodite in the all-solid-state battery comprising $Li(Ni_{0.8}Co_{0.1}Mn_{0.1})O_2$, novel halogen-rich argyrodite and lithium metal anode and the battery performance are described in this chapter. The discharge capacities of the batteries using three different compositions of $Li(Ni_{0.8}Co_{0.1}Mn_{0.1})O_2$ and novel argyrodite were measured to examine the suitable cathode mixture composition. The ionic and electronic conductivities of cathode mixtures were investigated to explain the different discharge capacity of the batteries using three different cathode compositions. The stability of novel argyrodite against $Li(Ni_{0.8}Co_{0.1}Mn_{0.1})O_2$ was investigated by analyzing impedance spectra during 50 cycles and X-Ray diffraction (XRD).

Chapter 4

The chapter reports the enhancement of discharge capacity of all-solid-state battery comprising $Li(Ni_{0.8}Co_{0.1}Mn_{0.1})O_2$, novel halogen-rich argyrodite and lithium metal anode by adding CA to the cathode. The discharge capacities and cycle durability of the batteries using different ratio of CA in cathode were measured to investigate the suitable ratio of CA in cathode and to enhance the discharge capacity and cycle durability. The ionic and electronic conductivities of cathode mixtures were investigated to explain the effect of CA in cathode on discharge capacity. The stabilities of novel argyrodite against $Li(Ni_{0.8}Co_{0.1}Mn_{0.1})O_2$ and CA were investigated by analyzing impedance spectra during 50 cycles.

Chapter 5

This chapter summarizes all the conclusions in this thesis.

References

[1] M. Z. Jacobson, *Energy Environ. Sci.*, **2**, 148, (2009).

[2] M. A. Hannan, M. S. H. Lipu, A. Hussain, and A. Mohamed, *Renew. Sustain. Energy Rev.*, **78**, 834-854, (2017).

[3] J. Janek and W. G. Zeier, *Nat. Energy*, **1**, 16141, (2016).

[4] Y. Kato, S. Hori, T. Saito, K. Suzuki, M. Hirayama, A. Mitsui, M. Yonemura, H. Iba, and R. Kanno, *Nat. Energy*, **1**, 16030, (2016).

[5] S. Boulineau, J. M. Tarascon, J. B. Leriche, and V. Viallet, *Solid State Ionics*, **242**, 45, (2013).

[6] P. Wang, H. Liu, S. Patel, X. Feng, P.-H. Chien, Y. Wang, and Y. Y. Hu, *Chem. Mater.*, **32**, 3833-3840, (2020).

[7] Y. Inaguma, C. Liquan, M. Itoh, T. Nakamura, T. Uchida, H. Ikuta, M. Wakihara, *Solid State Commun.,* **86**, 689-693, (1993).

[8] J. Fu, *Solid State Ionics,* **104**, 191-194, (1997).

[9] R. Murugan, V. Thangadurai, W. Weppner, *Angew. Chem. Int. Ed.*, **46**, 7778-7781, (2007).

[10] Y. Li, J. T. Han, C. A. Wang, H. Xie, J. B. Goodenough, *J. Mater. Chem.,* **22,** 15357-15361, (2012).

[11] C. Bernuy-Lopez, W. Jr. Manalastas, J. M. Lopez del Amo, A. Aguadero, F. Aguesse, J. A. Kilner, *Chem. Mater.,* **26**, 3610-3617, (2014).

[12] X. Feng, P. H. Chien, Y. Wang, S. Petel, P. Wang, H. Liu, M. Immediato-Scuotto, and

Y. Y. Hu, *Energy. Stor. Mater.*, **30**, 67, (2020).

[13] P. Adeli, J. D. Bazak, K. H. Park, I. Kochetkov, A. Huq, G. R. Goward, and L. F. Nazar, *Angew. Chem. Int. Ed.*, **58**, 8681, (2019).

[14] P. Adeli, J. D. Bazak, A. Huq, G. R. Goward, and L. F. Nazar, *Chem. Mater.*, **33**, 146, (2021).

[15] M. Suyama, A. Kato, A. Sakuda, A. Hayashi, and M. Tatsumisago, *Electrochim*. *Acta*, **286**, 158, (2018).

[16] M. Ribes, B. Barrau, J. L. Souquet, *J. Non-Cryst. Solids,* **271**, *38–39*, (1980).

[17] R. Mercier, J. P. Malugani, B. Fahys, G. Robert, *Solid State Ionics,* **5**, 663, (1981).

[18] H. Wada, M. Menetrier, A. Levasseur, P. Hagenmuller, *Mat. Res. Bull.,* **18**, 189, (1983).

[19] J. H. Kennedy, Z. Zhang, *J. Electrochem. Soc.,* **135**, 859, (1988).

[20] J. H. Kennedy, Z. Zhang, *Solid State Ionics*, **28**, 726, (1988).

[21] Z. M. Zhang, J. H. Kennedy, *Solid State Ionics*, **38**, 217, (1990).

[22] R. Sakamoto, M. Tatsumisago, T. Minami, *J. Phys. Chem. B*, **103**, 4029, (1999).

[23] L. Long, S. Wang, M. Xiao, Y. Meng, *J. Mater. Chem. A*, **4**, 10038, (2016).

[24] F. Mizuno, A. Hayashi, K. Tadanaga, M. Tatsumisago, *Adv. Mater.*, **17**, 918, (2005).

[25] F. Mizuno, A. Hayashi, K. Tadanaga, M. Tatsumisago, *Solid State Ionics*, **177**, 2721, (2006).

[26] H. Yamane, M. Shibata, Y. Shimane, T. Junke, Y. Seino, S. Adams, K. Minami, A. Hayashi, M. Tatsumisago, *Solid State Ionics*, **178**, 1163, (2007).

[27] M. Tachez, J.-P. Malugani, R. Mercier, G. Robert, *Solid State Ionics*, **14**, 181, (1984).

[28] B. R. Shin, Y. J. Nam, D. Y. Oh, D. H. Kim, J. W. Kim, Y. S. Jung, *Electrochim. Acta*, **146**, 395, (2014).

[29] K. Homma, M. Yonemura, T. Kobayashi, M. Nagao, M. Hirayama, R. Kanno, *Solid State Ionics*, **182**, 53-58, (2011).

[30] T. Kaib, S. Haddadpour, M. Kapitein, P. Bron, C. Schroeder, H. Eckert, B. Roling, S. Dehnen, *Chem. Mater.*, **24**, 2211, (2012)

[31] R. C. Xu, X. H. Xia, X. L. Wang, Y. Xia, J. P. Tu, *J. Mater. Chem. A*, **5**, 2829, (2017).

[32] G. Sahu, E. Rangasamy, J. Li, Y. Chen, K. An, N. Dudney, C. Liang, *J. Mater. Chem. A*, **2**, 10396, (2014).

[33] M. Park, H.-G. Jung, W. D. Jung, S. Y. Cho, B.-N. Yun, Y. S. Lee,S. Choi, J. Ahn, J. Lim, J. Y. Sung, Y.-J. Jang, J.-P. Ahn, J.-H. Lee,H. Kim, *ACS Energy Lett.*, **2**, 1740, (2017).

[34] E. Rangasamy, Z. Liu, M. Gobet, K. Pilar, G. Sahu, W. Zhou, H. Wu, S. Greenbaum, C. Liang, *J. Am. Chem. Soc.*, **137**, 1384, (2015).

[35] S. J. Sedlmaier, S. Indris, C. Dietrich, M. Yavuz, C. Draeger, F. von Seggern, H. Sommer, J. Janek, *Chem. Mater.*, **29**, 1830, (2017).

[36] S. Ujiie, A. Hayashi, M. Tatsumisago, *Solid State Ionics*, **211**, 42, (2012).

[37] W. Zhijun, X. Zhengkun, Y. Akihiro, A. Xiaowei, W. Zhongde, H. Xiaogang, A. Abuliti, G. Guoqing, *Chem Eng J.*, **380**, 122419, (2020).

[38] K. H. Park, D. Y. Oh, Y. E. Choi, Y. J. Nam, L. Han, J.-Y. Kim, H. Xin, F. Lin, S. M. Oh, Y. S. Jung, *Adv. Mater.*, **28**, 1874, (2016).

[39] R. Kanno, M. Murayama, *J. Electrochem. Soc.*, **148**, A742, (2001).

[40] M. Murayama, R. Kanno, Y. Kawamoto, T. Kamiyama, *Solid State Ionics*, **789**, 154-155, (2002).

[41] M. Murayama, R. Kanno, M. Irie, S. Ito, T. Hata, N. Sonoyama, Y. Kawamoto, *J. Solid State Chem.*, **168**, 140, (2002).

[42] M. Murayama, N. Sonoyama, A. Yamada, R. Kanno, *Solid State Ionics*, **170**, 173,

(2004).

[43] T. Inada, T. Kobayashi, N. Sonoyama, A. Yamada, S. Kondo, M. Nagao, R. Kanno, *J. Power Sources*, **194**, 1085, (2009).

[44] T. Kobayashi, A. Yamada, R. Kanno, *Electrochim. Acta*, **53**, 5045, (2008).

[45] N. Kamaya, K. Homma, Y. Yamakawa, M. Hirayama, R. Kanno, M. Yonemura, T. Kamiyama, Y. Kato, S. Hama, K. Kawamoto, A. Mitsui, *Nat. Mater.*, **10**, 682, (2011).

[46] P. Bron, S. Johansson, K. Zick, J. Schmedt auf der Gunne, S. Dehnen, B. Roling, *J. Am. Chem. Soc.*, **135**, 15694, (2013).

[47] A. Kuhn, V. Duppel, B. V. Lotsch, *Energ. Environ. Sci.*, **6**, 3548, (2013).

[48] A. Kuhn, O. Gerbig, C. Zhu, F. Falkenberg, J. Maier, B. V. Lotsch, *Phys. Chem. Chem. Phys.*, **16**, 14669, (2014).

[49] S. Hori, K. Suzuki, M. Hirayama, Y. Kato, T. Saito, M. Yonemura, R. Kanno, *Faraday Discuss.*, **176**, 83, (2014).

[50] D. A. Weber, A. Senyshyn, K. S. Weldert, S. Wenzel, W. Zhang, R. Kaiser, S. Berendts, J. Janek, W. G. Zeier, *Chem. Mater.*, **28**, 5905, (2016).

[51] P. Bron, S. Dehnen, B. Roling, *J. Power Sources*, **329**, 530, (2016).

[52] T. Krauskopf, S. P. Culver, W. G. Zeier, *Chem. Mater.*, **30**, 1791, (2018).

[53] Y. Sun, K. Suzuki, S. Hori, M. Hirayama, R. Kanno, *Chem. Mater.*, **29**, 5858, (2017).

[54] J. Liang, N. Chen, X. Li, X. Li, K. R. Adair, J. Li, C. Wang, C. Yu, M. Norouzi Banis, L. Zhang, S. Zhao, S. Lu, H. Huang, R. Li, Y. Huang, X. Sun, *Chem. Mater.*, **32**, 2664, (2020).

[55] S. Hori, K. Suzuki, M. Hirayama, Y. Kato, R. Kanno, *Front. Energy Res.*, **4**, 38, (2016).

[56] Y. Sun, K. Suzuki, K. Hara, S. Hori, T.-A. Yano, M. Hara, M. Hirayama, R. Kanno,

J. Power Sources, **324**, 798, (2016).

[57] K.-H. Kim, S. W. Martin, *Chem. Mater.*, **31**, 3984, (2019).

[58] K. Takada, M. Osada, N. Ohta, T. Inada, A. Kajiyama, H. Sasaki, S. Kondo, M. Watanabe, T. Sasaki, *Solid State Ionics*, **176**, 2355, (2005).

[59] W. D. Richards, T. Tsujimura, L. J. Miara, Y. Wang, J. C. Kim, S. P. Ong, I. Uechi, N. Suzuki, G. Ceder, *Nat. Commun.*, **7**, 11009, (2016).

[60] Z. Zhang, E. Ramos, F. Lalere, A. Assoud, K. Kaup, P. Hartman, L. F. Nazar, *Energ. Environ. Sci.*, **11**, 87, (2018).

[61] M. Duchardt, U. Ruschewitz, S. Adams, S. Dehnen, B. Roling, *Angew. Chem., Int. Ed.*, **57**, 1351, (2018).

[62] A. Kuhn, J. Kohler, B. V. Lotsch, *Phys. Chem. Chem. Phys.*, 15, 11620, (2013).

[63] R. Iwasaki, S. Hori, R. Kanno, T. Yajima, D. Hirai, Y. Kato, Z. Hiroi, *Chem. Mater.*, **31**, 3694, (2019).

[64] Y. Wang, Z. Liu, X. Zhu, Y. Tang, F. Huang, *J. Power Sources*, **224**, 225, (2013).

[65] H. Wada, M. Ishii, M. Onoda, M. Tansho, A. Sato, *Solid State Ionics*, **86-88**, 159-163, (1996).

[66] M. Onoda, H. Wada, A. Sato, M, Ishii, *J. Alloys Compd*., **383**, 113-117, (2004).

[67] I. J. Alverdiyev, Z. S. Aliev, S. M. Bagheri, L. F. Mashadiyeva, Y. A. Yusibov, M. B. Babanly, *J. Alloys Compd*., **691**, 255-262, (2017).

[68] E. Gaudin, H. J. Deiseroth, T. Zaiß, *Z. Kristallogr. Cryst. Mater.*, 216, 39-44, (2001).

[69] H. J. Deiseroth, S. T. Kong, H. Eckert, J. Vannahme, C. Reiner, T. Zaiß, M. Schlosser, *Angew. Chem*., **120**, 767-770, (2008).

[70] S. T. Kong, Ö. Gün, B. Koch, H. J. Deiseroth, H. Eckert, C. Reiner, *Chem. Eur. J.* **16**, 5138, (2010).

[71] C.Yu, S. Ganapathy, J. Hargeman. L. V. Eijck, E. R. H. V. Eck, L. Zhang, T. Schwietert, S. Basak, E. M. kelder, M. Wagemaker, *ACS Appl. Mater. Interfaces.* **10**, 33296, (2018).

[72] K. Sato, A. Tamai, K. Ohara, H. Kikuchi, E. Matsubara, *J. Power Sources.* **535**, 231399, (2022).

[73] T. Yajima, F. Takeiri, K. Aidzu, H. Akamatsu, K. Fujita, W. Yoshimune, M. Ohkura, S. Lei, V. Gopalan, K. Tanaka, C. M. Brown, M. A. Green, T. Yamamoto, Y. Kobayashi, H. Kageyama, *Nat. Chem*. **7**, 1017, (2015).

[74] N. Masuda, Y. Kobayashi, O. Hernandez, T. Bataille, S. Paofai, H. Suzuki, C. Ritter, N. Ichijo, Y. Noda, K. Takegoshi, C. Tassel, T. Yamamoto, H. Kageyama, *J. Am. Chem. Soc.* **137**, 15315, (2015).

[75] Z. Zhang, Y. Sun, X. Duan, L. Peng, H. Jia, Y. Zhang, B. Shan, J. Xie, *J. Mater. Chem. A*, **7**, 2717, (2019).

[76] H. Schneider , S. J. Sedlmaier , H. Du , T. Kelley , K. Leitner , J. ter Maat , C. Scordilis-Kelley , A. Mudalige , J. Kulisch and L. Schneider , *ChemistrySelect*, **4** , 3351 -3354, (2019).

[77] S. Boulineau, M. Courty, J. M. Tarascon, V. Viallet, *Solid State Ionics*, **221**, 1-5, (2012).

[78] Z. Zhang, J. Zhang, H. Jia, L. Peng, T. An, J. Xie, *J. Power Sources*, **450**, 227601, (2020).

[79] A. R. Stamminger, B. Ziebarth, M. Mrovec, T. Hammerschmidt, R. Drautz, *Chem. Mater*., **31**, 8673-8678, (2019).

[80] R. Schlem, M. Ghidiu, S. P. Culver, A. Hansen, W. G. Zeier, *ACS Appl. Energy Mater.*, **3**, 9-18, (2020).

[81] V. Epp, Ö. Gün, H. J. Deiseroth, M. Wilkening, *Phys. Chem. Chem. Phys.*, **15**, 7123-7132, (2013).

[82] M.A. Kraft, S. Ohno, T. Zinkevich, R. Koerver, S.P. Culver, T. Fuchs, A. Senyshyn, S. Indris, B.J. Morgan, W.G. Zeier, *J. Am. Chem. Soc.*, **140**, 16330-16339, (2018).

[83] L. Zhou, A. Assoud, Q. Zhang, X. Wu, L.F. Nazar, *J. Am. Chem. Soc.*, **141**, 19002-19013, (2019).

[84] Y. Lee, J. Jeong, H. J. Lee, M. Kim, D. Han, H. Kim, J. M. Yuk, K. W. Nam, K. Y. Chung, H. G. Jung , *ACS Energy Lett,* **7**, 171–179, (2021).

[85] A. Gautam, M. Sadowski, N. Prinz, H. Eickhoff, N. Minafra, M. Ghidiu, S. P. Culver, K. Able, T. F. Fässler, M. Zobel, W. G. Zeier, *Chem. Mater*., 24, 10178-10185, (2019).

[86] A. Gautam, M. Sadowski, M. Ghidiu, N. Minafra, A. Senyshyn, K. Albe, W. G. Zeier, *Adv. Energy Mater.*, **11**, 2003369, (2021).

[87] S. V. Patel, S. Banerjee, H. Liu, P. Wang, P. H. Chien, X. Feng, J. Liu, S. P. Ong, Y. Y. Hu, *Chem. Mater.,* **33**, 1435-1443, (2021).

[88] N. J. J. De Klerk, I. Rosłoń, M. Wagemaker, *Chem. Mater.,* **28**, 7955-7963, (2016).

[89] M. A. Kraft, S. P. Culver, M. Calderon, F. Böcher, T. Krauskopf, A. Senyshyn, C. Dietrich, A. Zevalkink, J. Janek, W. G. Zeier, *J. Am. Chem. Soc.* **139**, 10909-10918, (2017).

[90] C. Yu, Y. Li, W. Li, K. R. Adair, F. Zhao, M. Willans, J. Liang, Y. Zhao, C. Wang, S. Deng, R. Li, H. Huang, S. Lu, T. K. Sham, Y. Huang, X. Sun, *Energy Stor. Mater.,* **30**, 238-249, (2020).

[91] W. D. Jung, J. S. Kim, S. Choi, S. Kim, M. Jeon, H. G. Jung, K. Y. Chung, J. H. Lee, B. K. Kim, J. H. Lee, H. Kim, *Nano Lett.,* **20**, 2303-2309, (2020).

[92] Y. Subramanian, R. Rajagopal, K. S. Ryu, *J. Power Sources.,* **520**, 230849, (2022).

[93] S. Kitajima, S. Ryu, J. Ku, S. Kim, Y. Park, D. Im, *Mater. Today Commun.* **28**, 102727, (2021).

[94] M. Cronau, M. Szabo, B. Roling, *Mater. Adv.,* **2**, 7842-7845, (2021).

[95] A. Gautam, M. Ghidiu, E. Suard, M. A. Kraft, W. G. Zeier, *ACS Appl. Energy Mater.,* **4**, 7309-7315, (2021).

[96] H. Wang, C. Yu, S. Ganapathy, E. R. H. Van Eck, L. Van Eijck, M. A. Wagemaker, *J. Power Sources.,* **412**, 29-36, (2019).

[97] L. Peng, C. Yu, Z. Zhang, H. Ren, J. Zhang, Z. He, M. Yu, L. Zhang, S. Cheng, J. Xie, *Chem. Eng. J.,* **430**, 132896, (2022).

[98] P. Lu, Y. Xia, G. Sun, D. Wu, S. Wu, W. Yan, X. Zhu, J. Lu, Q. Niu, S. Shi, Z. Sha, L. Chen, H. Li, *Nat. Commun.*, **14**, 4077, (2023).

[99] C. Yu, S. Ganapathy, J. Hageman, L. Van Eijck, E. R. H. Van Eck, L. Zhang, T. Schwietert, S. Basak, E. M. kelder, M. Wagemaker, *ACS Appl. Mater Interfaces.*, **10**, 33296-33306, (2018).

[100] K. Hogrefe, N. minafra, I. Hanghofer, A. Banik, W. G. Zeier, H. M. R. Wilkening, *J. Am. Chem. Soc.,* **144**, 1795-1812, (2022).

[101] A. Morscher, B. B. Duff, G. Han, L. M. Daniels, Y. Dang, M. Zanella, M. Sonni, A. Malik, M. S. Dyer, P. Chen, F. Blanc, J. B. Claridge, M. J. Rosseinsky, *J. Am. Chem. Soc.,* **144**, 22178-22192, (2022).

[102] B. T. Leube, C. M. Colins, L. M. Daniels, B. B. Duff, Y. Dang, R. Chen, M. W. Gaultois, T. D. Manning, F. Blanc, M. S. Dyer, J. B. Claridge, M. J. Rosseinsky, *Chem. Mater.,* **34**, 4073-4087, (2022).

[103] L. Zhou, Q. Zhang, L. F. Nazar, *Chem. Mater.,* **34**, 9634-9643, (2022).

[104] S. Wang, W. Zhang, X. Chen, D. Das, R. Ruess, A. Gautam, F. Walter, S. Ohno, R.

Koerver, Q. Zhang, W. G. Zeier, F. H. Richter, C. W. Nan, J. Janek, *Adv. Energy Mater.*, **11**, 2100654, (2021).

[105] S. Yubuchi, M. Uematsu, C. Hotehama, A. Sakuda, A. Hayashi, M. Tatsumisago, *J Mater Chem A*, **7**, 558–566, (2019).

[106] S. W. Park, G. Oh, J. W. Park, Y. C. Ha, S. M. Lee, S. Y. Toon, B. G. Kim, *Small*, **15**, 1900235, (2019)

[107] C. W. Wang, F. C. Ren, Y. Zhou, P. F. Yan, X. D. Zhou, S. J. Zhang, W. Liu, W. D. Zhang, M. H. Zou, L. Y. Zeng, X. Y. Yao, L. Huang, J. T. Li, S. G. Sun, *Energy Environ Sci*, **14**, 437–450, (2021).

[108] F. Walther, S. Randau, Y. Schneider, J. Sann, M. Rohnke, F. H. Richter, W. G. Zeier, J. Janek, *Chem. Mater*., **32**, 6123–6136, (2020).

[109] S. Randau, F. Walther, A. Neumann, Y. Schneider, R. S. Negi, B. Mogwitz, J. Sann, K. Becker-Steinberger, T. Danner, S. Hein, A. Latz, F. H. Richter, J. Janek, *Chem. Mater*., **33**, 1380–1393, (2021).

[110] F. Walther, F. Strauss, X. Wu, B. Mogwitz, J. Hertle, J. Sann, M. Rohnke, T. Brezesinski, J. Janek, *Chem. Mater*., **33**, 2110–2125, (2021).

[111] D. Kitsche, Y. Tang, Y. Ma, D. Goonetilleke, J. Sann, F. Walther, M. Bianchini, J. Janek, T. Brezesinski, *ACS Appl. Energy Mater*., **4**, 7338–7345, (2021).

[112] J. H. Choi, S. Choi, T. J. Embleton, K. Ko, K. S. Saqib, J. Ali, M. Jo, J. Hwang, S. Park, M. Kim, M. Hwang, H. Lim, P. Oh, *Nanomaterials*, **13**, 3065, (2023).

[113] K. J. Lee, Y. W. Byeon, H. J. Lee, Y. Lee, S. Park, H. R. Kim, H. K. Kim, S. J. Oh, J. P. Ahn, *Energy Storage Mater*., **57**, 326–333, (2023).

[114] S. Cangaz, F. Hippauf, F. S. Reuter, S. Doerfler, T. Abendroth, H. Althues, S. Kaskel, *Adv. Energy Mater*., **10**, 2001320, (2020).

[115] Y. Li, Y. Wu, T. Ma, Z. Wang, Q. Gao, J. Xu, L. Chen, H. Li, F. Wu, *Adv. Energy Mater*., **12**, 2001732, (2022).

[116] P. Minnmann, L. Quillman, S. Burkhardt, F. H. Richter, J. Janek, *J. Electrochem. Soc*., **168**, 040537, (2021).

[117] J. Ann, S. Choi, J. Do, S. Lim, D. Shin, *J. Ceram. Process. Res*., **19**, 413, (2018).

[118] S. Poetke, F. Hippauf, A. Baasner, S. Dörfler, H. Althues, S. Kaskel, *Batter. Supercaps*, **4**, 1323–1334, (2021).

[119] S. Jun, Y. J. Nam, H. Kwak, K. T. Kim, D. Y. Oh, Y. S. Jung, *Adv. Funct. Mater*., **30**, 2002535, (2020).

[120] R. Fang, Y. Liu, Y. Li, A. Manthiram, J. B. Goodenough, *Mater. Today*, **64**, 52–60, (2023).

[121] K. T. Kim, J. Woo, Y. S. Kim, S. Sung, C. Park, C. Lee, Y. J. Park, H. W. Lee, K. Park, Y. S. Jung, *Adv. Energy Mater*., **13**, 2301600, (2023).

[122] D. H. S. Tan, E. A. Wu, H. Nguyen, Z. Chen, M. A. T. Marple, J. M. Doux, X. Wang, H. Yang, A. Banerjee, Y. S. Meng, *ACS Energy Lett*., **4**, 2418–2427, (2019).

[123] W. Zhang, T. Leichtweiß, S. P. Culver, R. Koerver, D. Das, D. A. Weber, W. G. Zeier, J. Janek, *ACS Appl. Mater. Interfaces*, **9**, 35888–35896, (2017).

[124] J. H. Teo, F. Strauss, D. Tripkovi, S. Schweidler, Y. Ma, M. Bianchini, J. Janek, T. Brezesinski, *Cell Rep.,* **2**, 100465, (2021).

[125] M. Yamamoto, Y. Terauchi, A. Sakuda, M. Takahashi, *J. Power Sources*, **402**, 506–512, (2018).

[126] A. Y. Kim, F. Strauss, T. Bartsch, J. H. Teo, J. Janek, T. Brezesinski, *Sci. Rep*., **11**, 5367, (2021).

[127] T. J. Embleton, J. Yun, J. H. Choi, J. Kim, K. Ko, J. Kim, Y. Son, P. Oh, *Appl. Surf.*

Sci., **610**, 155490, (2023).

[128] R. Koerver, I. Aygün, T. Leichtweiß, C. Dietrich, W. Zhang, J. O. Binder, P. Hartmann, W. G. Zeier, J. Janek, *Chem. Mater.*, **29**, 5574, (2017).

[129] K. Märker, P. J. Reeves, C. Xu, K. J. Griffith, C. P. Grey, *Chem. Mater.*, **31**, 2545, (2019).

[130] Z. Ruff, C. S. Coates, K. Märker, A. Mahadevegowda, C. Xu, M. E. Penrod, C. Ducati, C. P. Grey, *Chem. Mater.*, **35**, 4979-4987, (2023).

[131] T. Swamy, X. Chen, Y. M. Chiang, *Chem. Mater.*, **31**, 707–713, (2019).

[132] T. Hakari, M. Deguchi, K. Mitsuhara, T. Ohta, K. Saito, Y. Orikasa, Y. Uchimoto, Y. Kowada, A. Hayashi, M. Tatsumisago, *Chem, Mater*., **29**, 4768–4774, (2017).

2. Structural Analysis of Novel $Li_{7-x-y}(PS_4)(S_{2-x-y}Cl_xBr_y)$ Argyrodite and Mechanism of Lithium Conduction Path

2.1 introduction

Over the years, various high-performing lithium-ion rechargeable batteries have been developed to address global warming[1] and realize a sustainable carbon-neutral society.[2] All-solid-state lithium-ion batteries are considered a promising next-generation solution[3] to deliver more energy than that of their conventional counterparts comprising liquid electrolytes.[4] All-solid-state batteries contain a cathode, anode, and electrolyte. Their properties depend mostly on the characteristics of the electrolyte.[5] Unfortunately, these batteries have low rate capabilities and energy densities, partly because of the lack of suitable electrolytes that exhibit higher ionic conductivities than those of liquid electrolytes.[6] Recent studies have shown that batteries containing electrolytes comprising phosphorus sulfide and lithium are promising[7] because of their higher ionic conductivities,[8] mechanical softness,[9] and facile processing.[10]

Among the phosphorus sulfides, various argyrodites Li_6PS_5X (X = Cl, Br, I)[11] that exhibit high ionic conductivities have been explored.[12] An ideal crystal structure of argyrodite can be illustrated by a frame structure (PS_5X, Figure 1(a)) and lithium-cages (Li_6(X, S), Figure 1(b)).[13] The chemical formula of the argyrodite is usually described as $Li_{7-\alpha}PS_{6-\alpha}X_\alpha$ (X = halogen).[14] Hereafter, the argyrodite is denoted as $Li_{7-x-y}(PS_4)(S_{2-x-y}Cl_xBr_y)$ to distinguish the sulfide anions that form the PS_4 tetrahedra from those present at the 4a and 4d sites.

Reprinted with permission from American Chemical Society

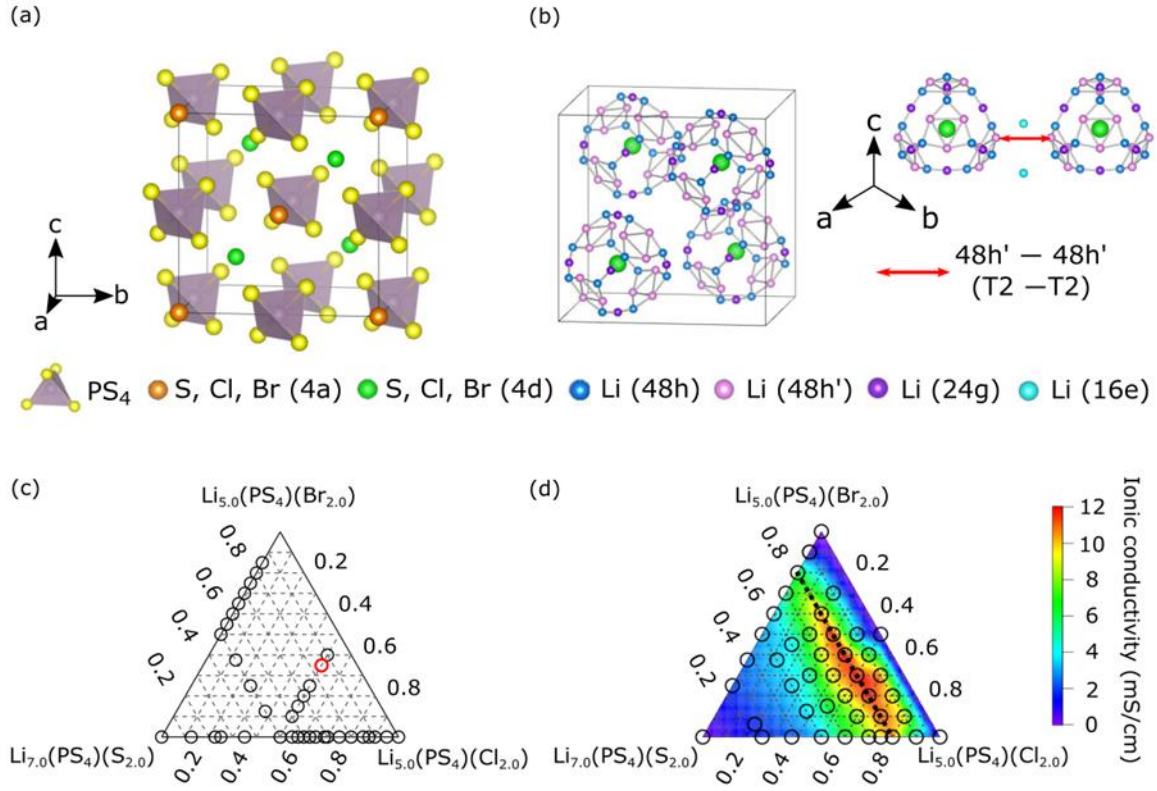

Figure 1. Crystal structure of an ideal argyrodite. (a) Frame structure of argyrodite [$(PS_4)(S_{2-x-y}Cl_xBr_y)$]. (b) Cage structure with lithium and 4d anions. (c) Open circles are investigated compositions in references. Ionic conductivities of these compositions are also reported. Red circle denotes composition with highest conductivity (24 mS/cm), $Li_{5.3}(PS_4)(S_{0.3}Cl_{1.0}Br_{0.7})$.[13] (d) Open circles show compositions investigated in this study and contour plot of ionic conductivity of $Li_{7-x-y}(PS_4)(S_{2-x-y}Cl_xBr_y)$. Black dashed line indicates ($x + y = 1.6$) composition.

A quasi-ternary system, $Li_7(PS_4)(S_2)$–$Li_5(PS_4)(Cl_2)$–$Li_5(PS_4)(Br_2)$, can be devised using argyrodite $Li_{7-x-y}(PS_4)(S_{2-x-y}Cl_xBr_y)$ (4 1(c) and (d)).[15] Various compositions of such a ternary system have been explored (Figure 1(c)).[16] However, the investigated compositions have highly limited ternary plots.[17] Although $Li_{5.3}(PS_4)(S_{0.3}Cl_{1.0}Br_{0.7})$ exhibits enhanced ionic conductivity (up to 24 mS/cm) (Figure 1(c)),[13] the composition required for the highest conductivity has not been investigated thus far. Therefore, investigating the composition of a ternary system to obtain a high lithium-ion

Reprinted with permission from American Chemical Society

conductivity remains an important research topic.

In addition, the lithium-ion conduction mechanism in argyrodite is yet to be revealed; however, several researchers have proposed different conduction paths. It is essential that the relationship between the lithium-ion conduction mechanism in argyrodite and the ionic conductivity is elucidated to enhance the performance of all-solid-state batteries. Powder neutron diffraction studies of $Li_{6.0}(PS_4)(S_{1.0}Br_{1.0})$ have shown the anion disorder at the 4a and 4d sites, i.e., anions (bromide ions and sulfide ions, respectively) are distributed equally, and this distribution is an important prerequisite for achieving the superionic conductivity.[12] It has also been reported that lithium first migrates locally around the 4d site, like a "cage" (Figure 1(b)), and thereafter migrates through the entire lattice between one "cage" and the neighboring "cage". This phenomenon can be defined as inter-cage conduction.[18]

The ionic conductivity was enhanced when the distance between the 4d site and lithium in the cage was increased from 2.4 to 2.5 Å.[12] Therefore, the inter-cage conduction path 48h′–48h′ (T2–T2) (Figure 1(b) and Table S2) decreases from 2.1 to 1.5 Å, and clearly affects the controlled anion disorder leading to a four-fold increase in the ionic conductivity.[12] The conduction mechanism in the argyodite structure has been investigated in previous studies[16] in which the ionic conductivity was gradually increased.[19] However, the conduction path for a halogen-rich composition,[20] such as $Li_{7-x-y}(PS_4)(S_{2-x-y}Cl_xBr_y)$, ($x + y > 1.0$), has not been elucidated,[21] even after combining multiple calculation methods. This is due to the difficulty in calculating the conduction path in the argyrodite structure that contains three anions[22] and lithium-deficient sites.[23] In this study, we investigated the conductivity distribution in $Li_{7-x-y}(PS_4)(S_{2-x-y}Cl_xBr_y)$ using a quasi-ternary $Li_7(PS_4)(S_2)$–$Li_5(PS_4)(Cl_2)$–$Li_5(PS_4)(Br_2)$ system.[24] We attempted

Reprinted with permission from American Chemical Society

to substitute chloride and bromide ions, respectively, at the 4a and 4d sites with sulfide ions by introducing a lithium-deficient site[25] to obtain a $Li_{7-x-y}(PS_4)(S_{2-x-y}Cl_xBr_y)$ composition that affords a high ionic conductivity. In addition, we examined the effect of site disorder on the ionic conductivity of different compositions.

We also explored the conduction path by combining the maximum entropy method (MEM) and Rietveld refinement of the neutron diffraction data. By introducing the MEM result of the lithium position in the initial structure of the Rietveld refinement, the interstitial position of lithium can be predicted more precisely compared with when only the Rietveld refinement of neutron diffraction was used; precision is increased because MEM results provide direct evidence of the presence of interstitial atoms,[26] and their positions in the unit cell.[27] The length from the 4d site to the lithium in the cage and the inter-cage conduction path length were calculated for $Li_{5.4}(PS_4)(S_{0.4}Cl_{1.6})$, $Li_{5.4}(PS_4)(S_{0.4}Cl_{1.0}Br_{0.6})$, and $Li_{5.4}(PS_4)(S_{0.4}Cl_{0.6}Br_{1.0})$. We attempted to compare our proposed conduction path with the conventional direct 48h′–48h′ (T2–T2) conduction path (Figure 1(b)),[12] and noted a clear difference in the ionic conductivity when we calculated the inter-cage conduction path length.

2.2 Experimental

2.2.1 Material synthesis

The starting materials Li_2S (>99.9% purity, Idemitsu Kosan, Japan), P_2S_5 (>99% purity, Sigma Ardrich Japan, Japan), LiCl (>99.9% purity, FUJIFILM Wako Pure Chemical Corporation, Japan), and LiBr (>99.99% purity, FUJIFILM Wako Pure Chemical Corporation, Japan) were mixed in an appropriate molar ratio (total weight 10.0 g) in an argon-filled glovebox under 1 ppm of moisture and oxygen. The mixture was placed in a

Reprinted with permission from American Chemical Society

ZrO_2 pot containing a ZrO_2 ball (10 mmφ, 600 g). Thereafter, the mixture was mechanically milled using the planetary ball milling apparatus (Fritsch Pulverisette 5) at 220 rpm for 40 h. After ball milling, the mixture was placed in an Al_2O_3 case enclosed with a stainless steel tube and heated in an argon atmosphere under 1 ppm of moisture and oxygen. The sample temperature was first ramped from room temperature (290 K to 300 K) to 623 K in 1 h and then to 703 K in 30 min; the sample was maintained at 703 K for 8 h. Subsequently, the sample was cooled to room temperature without any temperature control. The total number of compositions obtained was 44, as shown in Figure 1(d).

2.2.2 Laboratory X-Ray Powder Diffraction

Laboratory X-ray diffraction (Lab-XRD) was performed on Bragg–Brentano geometry at Bruker D2 PHASER. The applied settings of the divergence slit, solar slit, and air scatter screen were 1 mm, 0.04°, and 3 mm, respectively. The data were collected in the diffraction angle (2θ) range of 10–60° (step size = 0.05°) at room temperature (290 K to 300 K), and the scanning rate was 1 s per step. Each sample was packed in a flat glass folder and enclosed using Kapton film tape to avoid exposure to air.

2.2.3 Synchrotron Powder Diffraction

Synchrotron X-ray powder diffraction (Synchrotron-XRD) experiments were performed on a Debye-Scherrer camera at beamline BL19B2, SPring-8. The data were obtained using a semiconductor detector over a 2θ range of 2–70° (step size = 0.01°) at 80 K. The wavelength was 0.496190 Å, and the exposure time was 10 min. The samples were packed in quartz capillaries (outer diameter = 0.3 mm), encapsulated by epoxy resin in

Reprinted with permission from American Chemical Society

the argon-filled glovebox under 1 ppm of moisture and oxygen, and rotated during the measurement.

2.2.4 Neutron Powder Diffraction

The neutron diffraction data were obtained using the iMATERIA time-of-flight diffractometer at the Material and Life Science Experimental Facility of the Japan Proton Accelerator Research Complex. The samples were sealed in a 6-mm-diameter cell made from vanadium under argon using an indium ring to prevent exposure to air. The data were collected at room temperature (290 K to 300 K).

2.2.5 Rietveld Refinement and MEM Analysis

The structural parameters were refined using Rietan-FP,[28] while the profile parameters were refined using a split-pseudo-Voigt profile function for Lab-XRD and synchrotron-XRD patterns. The structural parameters were also refined using Z-Rietveld for neutron powder diffraction. Nuclear density distributions were calculated using the MEM, and the crystal structure factors and standard deviations were obtained from the Rietveld refinement. All MEM calculations were performed using the Z-MEM algorithm in the Z-Code software package,[29] which uses the conventional Sakata–Sato algorithm with zeroth-order single-pixel approximation.[30] Nuclear scattering densities were generated on a 98 × 98 × 98 grid by sampling the cell volume. The nuclear density was illustrated using VESTA.[31]

2.2.6 Electrochemical Impedance Spectroscopy

The temperature dependence of the ionic conductivity was measured by electrochemical impedance spectroscopy. The average particle size of the as-synthesized powder is 43 μm

Reprinted with permission from American Chemical Society

(Figure 2(a)), and the as-synthesized powder (0.3 g) was pressed into 9.5-mm-diameter pellets under 410 MPa (Figure 2(b)). Both sides of the pellets were covered with carbon-coated stainless steel foil (total thickness: 0.1 μm). The measurements were performed while the pellets were compressed under a pressure of 10 Nm using a screw and torque wrench under 1 ppm of moisture and oxygen. The powder was pressed without any sintering, and no binder was used. Impedance spectra were collected using a series of LN-Z2-HF cryostats (TOYO Corporation, Japan) with an impedance analyzer (E4990A, Keysight, USA). The amplitude voltage was 10 mV, and the frequency range was between 100 MHz and 20 Hz. The temperature was controlled from 200 to 350 K, and the collected impedance spectra were fitted using the Zmeam Program.[32]

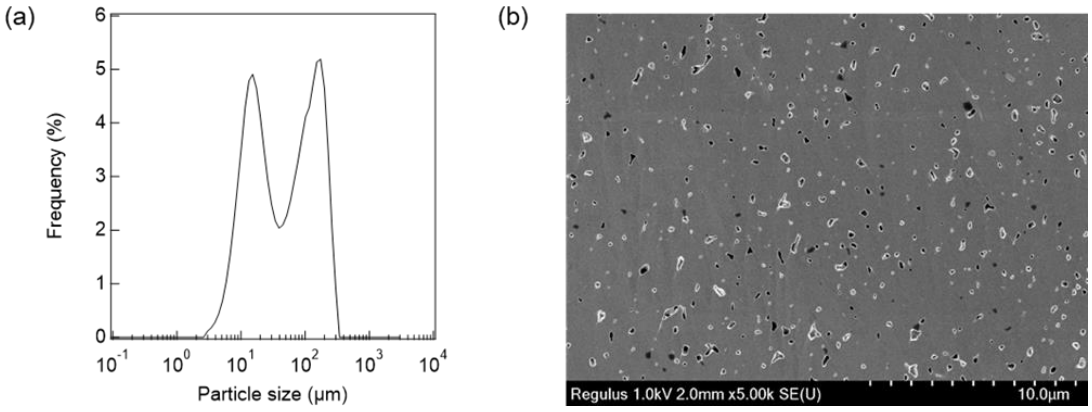

Figure 2. (a) Particle size distribution of as-synthesized $Li_{5.4}(PS_4)(S_{0.4}Cl_{1.0}Br_{0.6})$. Measurement was performed in toluene using laser diffraction particle size analyzer (Partica LA-960, HORIBA, Japan). (b) Cross-section SEM image of pelletized $Li_{5.4}(PS_4)(S_{0.4}Cl_{1.0}Br_{0.6})$.

2.2.7 Electrochemical Measurements

The battery was made using $Li_{5.4}(PS_4)(S_{0.4}Cl_{1.0}Br_{0.6})$ as the solid electrolyte material. The cathode-active material ($Li(Ni_{0.8}Co_{0.15}Al_{0.05})O_2$, (Shima Trading Company, Japan)) was

Reprinted with permission from American Chemical Society

coated with $Li_4Ti_5O_{12}$ in the same manner as that reported previously.[33] The anode-active material was artificial graphite (SFG75, Timcal). The cathode electrode was a mixture of coated $Li(Ni_{0.8}Co_{0.15}Al_{0.05})O_2$) and $Li_{5.4}(PS_4)(S_{0.4}Cl_{1.0}Br_{0.6})$ in a weight ratio of 7:3; the total weight of the cathode composite was 15 mg. The anode electrode was a 6:4 (by weight) mixture of artificial graphite and $Li_{5.4}(PS_4)(S_{0.4}Cl_{1.0}Br_{0.6})$; the total weight of the cathode composite was 12 mg. The cathode electrode mixture, solid electrolyte (100 mg), and anode electrode mixture were pressed into 10-mm-diameter pellets under 600 MPa. The measurements were performed while the battery pellets were compressed under a pressure of 10 Nm using a screw and torque wrench under 1 ppm of moisture and oxygen. The battery was charged and discharged between 2.7 V and 4.2 V at 298 K under 1 ppm of moisture and oxygen using a potentio-galvanostat (VMP-3, Biologic, France). A current density of 0.24 mA/cm^2 corresponds to 0.1 C in this all-solid-state battery.

A Li symmetry cell was made using $Li_{5.4}(PS_4)(S_{0.4}Cl_{1.0}Br_{0.6})$ as the solid electrolyte. The solid electrolyte (100 mg) was pressed into 10-mm-diameter pellets under 410 MPa. Thereafter, both sides of the pellet were covered with Li foil (10 mm φ, thickness: 2 mm; Honjo Metal, Japan), and pressed under 110 MPa. Current was applied to the Li symmetry cell under a pressure of 10 Nm at 298 K under 1 ppm of moisture and oxygen using a potentio-galvanostat (VMP-3, Biologic, France).

2.3 RESULTS AND DISCUSSION

2.3.1 Composition Map of $Li_{7-x-y}(PS_4)(S_{2-x-y}Cl_xBr_y)$ for Ionic Conductivity

Figure 1(d) presents the composition points of $Li_{7-x-y}(PS_4)(S_{2-x-y}Cl_xBr_y)$ in the quasi-$Li_7(PS_4)(S_2)$–$Li_5(PS_4)(Cl_2)$–$Li_5(PS_4)(Br_2)$ plot. An increase in the total quantity of the halide ions (chloride and bromide ions) induces a lithium-site vacancy in $Li_{7-x-y}(PS_4)(S_{2-}$

Reprinted with permission from American Chemical Society

$_{x\text{-}y}Cl_xBr_y$), which arises when charge neutrality is maintained. For $x + y < 1.6$, the lithium-site vacancy enhances the ionic conductivity. Excess halide ion ($x + y \geqq 1.7$) reduces the ionic conductivity (Figure 1(d)). A typical example can be found in the Lab-XRD data of $Li_{7\text{-}y}(PS_4)(S_{2\text{-}y}Br_y)$ (Figure 3). The ionic conductivity is enhanced when the y content in $Li_{7\text{-}y}(PS_4)(S_{2\text{-}y}Br_y)$ is less than 1.6. By contrast, when $y > 1.6$, the ionic conductivity decreases because of the segregation of impurities such as LiBr. This segregation can be confirmed by the Lab-XRD patterns (Figure 3). These results indicate that the induced lithium-site vacancy increases the ionic conductivity; however, excess substitution promotes the formation of byproducts that reduce the ionic conductivity.

When ($x + y = 1.6$) for $Li_{7\text{-}x\text{-}y}(PS_4)(S_{2\text{-}x\text{-}y}Cl_xBr_y)$, a high lithium-ion conductivity is obtained (Figure 1(d)). The lattice parameter of $Li_{7\text{-}x\text{-}y}(PS_4)(S_{2\text{-}x\text{-}y}Cl_xBr_y)$ with ($x + y = 1.6$) changes linearly with y (Figure 3 (c)); however, there is a slight impurity phase such as minor quantities of LiCl[8] and LiBr.[6] The maximum lithium-ion conductivity of 11.6 mS/cm is obtained when y = 0.6–1.0 at 298 K. The ionic conductivity decreases when $y > 1.0$ (Figure 3 and Figure 4).

The possibility that this decrease in conductivity is due to the temperature-treatment conditions has been proposed in previous papers.[34] However, the results of our study ruled out this hypothesis because we prepared all our samples under the same temperature conditions.

Our systematic conductivity measurements helped us determine the optimum composition of $Li_{7\text{-}x\text{-}y}(PS_4)(S_{2\text{-}x\text{-}y}Cl_xBr_y)$ to obtain a high lithium-ion conductivity when ($x + y = 1.6$). The highest conductivity was obtained when x = 0.6–1.0 (y = 0.6–1.0) in $Li_{7\text{-}x\text{-}y}(PS_4)(S_{2\text{-}x\text{-}y}Cl_xBr_y)$. We also prepared various composition maps for the lithium-ion conductivity in $Li_{7\text{-}x\text{-}y}(PS_4)(S_{2\text{-}x\text{-}y}Cl_xBr_y)$ recorded under the same annealing conditions.

Reprinted with permission from American Chemical Society

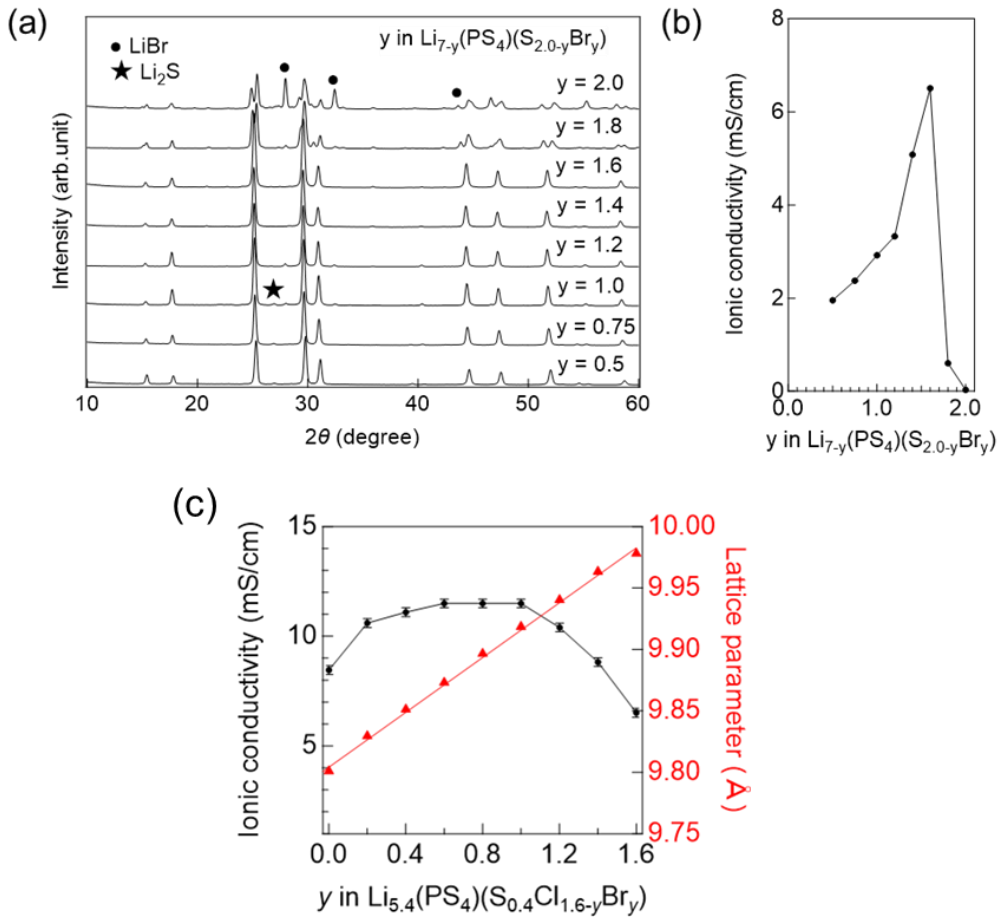

Figure 3. (a) Laboratory X-ray diffraction (Lab-XRD) patterns of $Li_{7-y}(PS_4)(S_{2-y}Br_y)$ (x = 0) and (b) ionic conductivity. An excess substitution promotes the formation of byproducts like LiBr and Li_2S. (c) Lattice parameter and ionic conductivity when $x + y$ = 1.6 in $Li_{7-x-y}(PS_4)(S_{2-x-y}Cl_xBr_y)$. Lattice parameter is calculated from laboratory X-ray diffraction data; error bar (almost negligible) for the red triangle marker falls inside the marker. Ionic conductivity is measured at 298 K.

Reprinted with permission from American Chemical Society

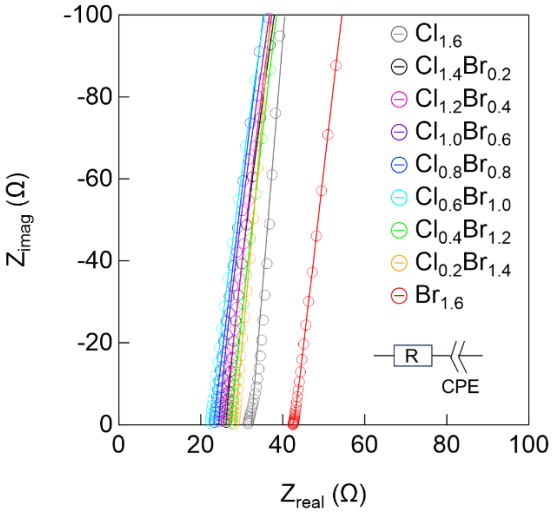

Figure 4. Impedance spectra of $Li_{5.4}(PS_4)(S_{0.4}Cl_{1.6-y}Br_y)$ at 300 K. The spectra are fitted by equivalent circuit.

2.3.2 Structural Characterization and MEM Analysis

Neutron diffraction can be used to quantify the quantity of lithium present inside a lattice by determining the neutron scattering length of each plane. Notably, the neutron scattering length is not proportional to the atomic number, i.e., it is different for each atom. The neutron scattering length of lithium is -1.9 fm, while that of the other cations and anions in $Li_{7-x-y}(PS_4)(S_{2-x-y}Cl_xBr_y)$ have positive values.[35] As a result, the quantity of lithium can be easily measured through the neutron diffraction method.

Figure 5 shows the neutron scattering density of $Li_{5.4}(PS_4)(S_{0.4}Cl_{1.6})$ ($x = 1.6$, $y = 0.0$) as determined by MEM analysis. The investigation of the relationship between the conduction mechanism and the structure of the halogen-rich $Li_{7-x-y}(PS_4)(S_{2-x-y}Cl_xBr_y)$ (when $x + y > 1$) was based on the MEM analysis. Lithium is present in four sites (48h, 24g, 48h′, and 16e); therefore, it is difficult to exhibit nuclear density three-dimensionally (Figure 6). Hence, the nuclear scattering density is only shown on the (111) plane for clarity. Figure 5(a) shows the vertical view of an interstitial site against the (111) plane.

Reprinted with permission from American Chemical Society

The bond valence sum (BVS) mapping of the lithium-ion on the (111) plane is shown in Figure 5(b). The BVS mapping of the lithium-ion presents the lithium conduction path as calculated from its bond valence and length.[36]

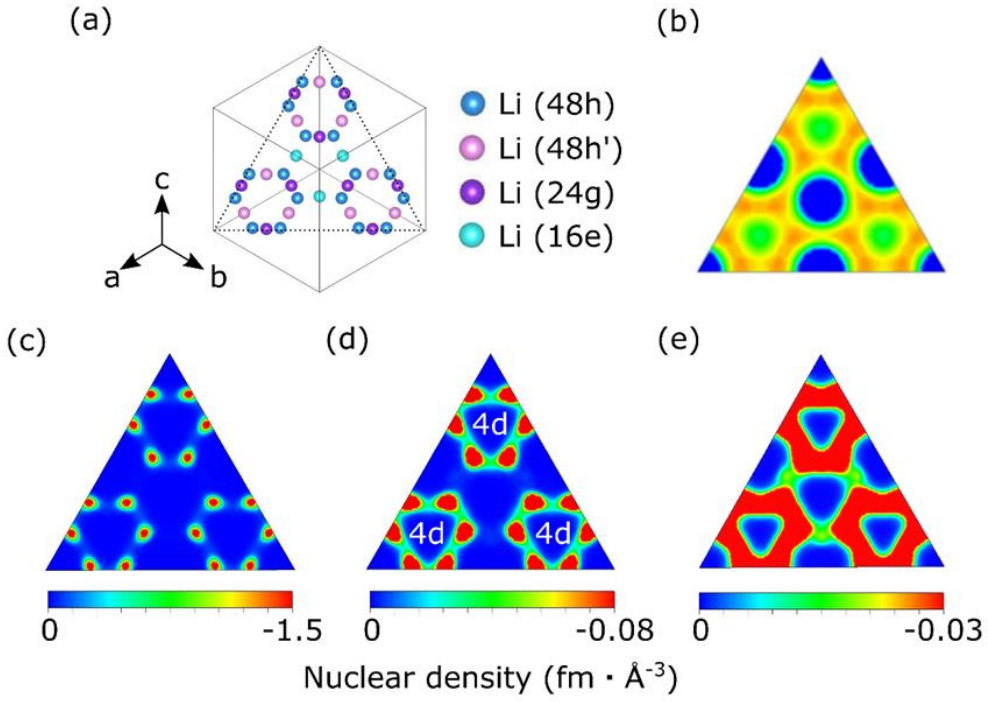

Figure 5. (a) Interstitial sites of the argyrodite structure from vertical view against the (111) plane. 16e and 4d sites are not exactly on (111) plane; instead, they are located at (x, x, x) and (0.75, 0.75, 0.75), respectively. (b) BVS mapping of lithium-ion on (111) plane. Density changes from red at a higher isosurface level to blue at a lower isosurface level. MEM nuclear density map of (111) plane in $Li_{5.4}(PS_4)(S_{0.4}Cl_{1.6})$($x$ = 1.6, y = 0). Maximum nuclear scattering density levels changed at (c) -1.5 fm/Å^3, (d) -0.08 fm/Å^3, and (e) -0.03 fm/Å^3.

Reprinted with permission from American Chemical Society

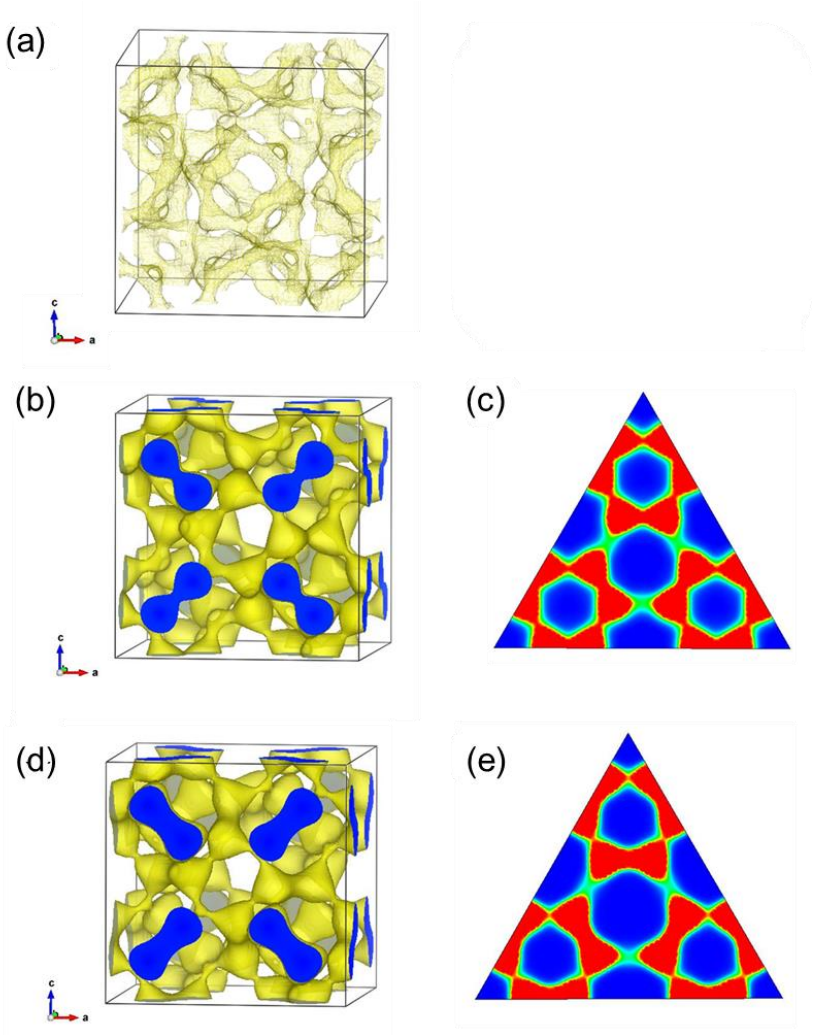

Figure 6. (a) Three-dimensional BVS mapping result. (b) (111) Plane of BVS mapping result. (c) Nuclear density mapping of $Li_{5.4}(PS_4)(S_{0.4}Cl_{1.0}Br_{0.6})$ (x = 1.0, y = 0.6). Minimum isosurface level is −0.03 fm/Å^3, and maximum isosurface level is 0 fm/Å^3. (d) (111) Plane of neutron density mapping of $Li_{5.4}(PS_4)(S_{0.4}Cl_{1.0}Br_{0.6})$ (x = 1.0, y = 0.6). (e) Nuclear density mapping of $Li_{5.4}(PS_4)(S_{0.4}Cl_{0.6}Br_{1.0})$ (x = 0.6, y = 1.0). (f) (111) Plane of nuclear density mapping of $Li_{5.4}(PS_4)(S_{0.4}Cl_{0.6}Br_{1.0})$ (x = 0.6, y = 1.0). Minimum isosurface level is −0.03 fm/Å^3, and maximum isosurface level is 0 fm/Å^3.

The MEM calculations showed that the lithium ions are mainly distributed at the 48h site (Table 2). MEM analysis is a useful method for the direct observation of nuclear and electron densities at an interstitial site[37] and for visualizing the ion-conduction path.[38]

Reprinted with permission from American Chemical Society

Our results reveal that (1) lithium ions are localized at the 48h site because of the high nuclear scattering density (Figure 5(c)), and (2) lithium ions are delocalized over three sites (48h, 24g, and 48h′) near the 4d site. Hence, the lithium ions are present around the 4d site (Figure 5(d)) because the nuclear scattering density at the delocalized sites is relatively low (Figure 5(c)).

At lower nuclear densities, lithium migrates through the entire lattice via the interstitial 16e site (Figure 5(e)).[39] The BVS mapping[34] and MEM results[40] have been used separately to illustrate the lithium conduction path. However, they have never been utilized together; our study is the first to do so. We also revealed that the BVS mapping coincides with the MEM results (Figures 5 (b) and (e)). Conventionally, the molecular dynamics simulation and MEM analysis report that lithium conducts locally around the 4d site in a manner akin to a “cage” structure.[13] The lithium inter-cage conduction path, calculated by both BVS mapping and MEM, has never been used to discuss the halogen-rich composition such as $Li_{7-x-y}(PS_4)(S_{2-x-y}Cl_xBr_y)$ with ($x + y > 1.0$). Our study showed that lithium conducts from one “cage” to the neighboring “cage” through the interstitial 16e site [41] in halogen-rich $Li_{7-x-y}(PS_4)(S_{2-x-y}Cl_xBr_y)$ with ($x + y > 1.0$).

The Rietveld refinement was employed again by distributing lithium ions at the 48h site, and at the 24g, 16e, and 48h′ sites (Table 2, Figures 7, 8 and 9) because the MEM analysis and BVS mapping indicated the presence of nuclear scattering density.[42] The elemental analysis revealed that the total bromide, chloride, and sulfide ion contents are almost similar to that of the nominal one (Table 1), indicating the absence of any volatile component in the sample. Moreover, it is difficult to confirm the amorphous and major impurity phases in this compound using synchrotron-XRD and ^{31}P NMR (Tables 3 and 4; Figures 10 and 11). Therefore, the refinement was performed under constraint. The total

Reprinted with permission from American Chemical Society

quantity of anions was found to be the same as that prepared (Tables 1, 2, 3, 5, 7, and 9), and there was no deficiency of occupation noted at the 4a and 4d sites. This method is similar to that reported in previous studies (Tables 2, 3, 5, 7, and 9).[12]

Chloride and sulfide ions at the same crystal site are indistinguishable by XRD; therefore, we attempted to calculate apparent anion occupancy of (chloride/sulfide) as a pseudo-single atom, which is usually adopted in mixed anion systems [26]. It is also difficult to determine lithium by XRD; therefore, lithium is distributed only at the 48h site, and its position was determined using neutron data. The site occupancy of bromide ion at the 4a site is in good agreement with that of neutron data (Figure 7-9 and 11-13, Table 3-9).

Table 1. Results of elemental analysis of $Li_{7-x-y}(PS_4)(S_{2-x-y}Cl_xBr_y)$ performed using inductively coupled plasma (ICP) atomic absorption spectroscopy. Samples (0.1 g) were dissolved in KOH solution under Ar atmosphere. All samples were measured 4 times.

			mol%				
x	*y*		Li	P	S	Cl	Br
1.6	0	Prepared	5.40	1.00	4.40	1.60	—
		sample	5.41(1)	1.00(1)	4.38(2)	1.68(2)	—
1.0	0.6	Prepared	5.40	1.00	4.40	1.00	0.60
		sample	5.37(1)	1.00(1)	4.32(2)	1.08(2)	0.62(2)
0.6	1.0	Prepared	5.40	1.00	4.40	0.60	1.00
		sample	5.43(1)	1.00(2)	4.36(2)	0.63(3)	1.04(3)
0.0	1.6	Prepared	5.40	1.00	4.40	—	1.60
		sample	5.22(1)	1.00(1)	4.38(1)	—	1.52(3)

Reprinted with permission from American Chemical Society

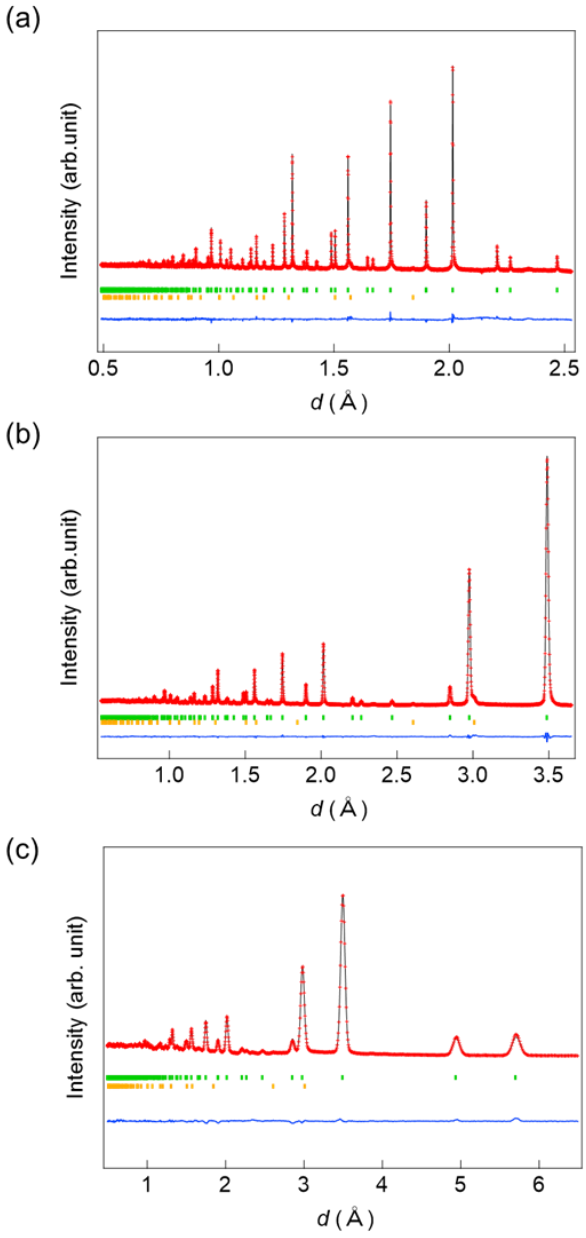

Figure 7. Neutron diffraction patterns and refined result for $Li_{5.4}(PS_4)(S_{0.4}Cl_{1.0}Br_{0.6})$ (x = 1.0, y = 0.6). Refinements were performed by Rietveld method. (a) BS blank data. (b) SE blank data. (c) LA35 blank data. Refinement was performed using data of BS, SE, and LA35 blanks simultaneously. Red ticks and black line are observed diffraction data and calculated data, respectively; difference profile is shown in blue. Calculated Bragg reflections of $Li_{5.4}(PS_4)(S_{0.4}Cl_{1.0}Br_{0.6})$ and $LiCl_{0.81}Br_{0.19}$ are shown as green and orange ticks, respectively.

Reprinted with permission from American Chemical Society

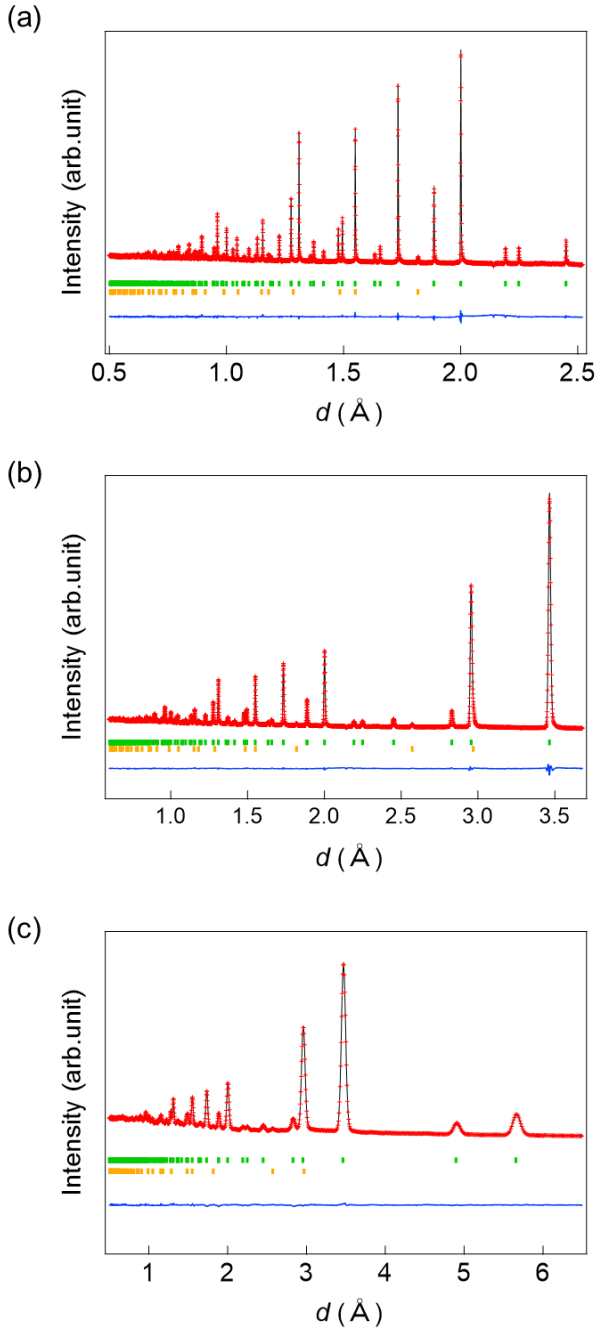

Figure 8. Neutron diffraction patterns and corresponding Rietveld refinement of $Li_{5.4}(PS_4)(S_{0.4}Cl_{1.6})$ (x = 1.6, y = 0.0). (a) BS blank data. (b) SE blank data. (c) LA35 blank data. Refinement was performed using data of BS, SE, and LA35 blanks simultaneously. Red ticks and black line represent observed diffraction data and calculated data, respectively, while difference profile is shown in blue. Calculated Bragg reflections of $Li_{5.4}(PS_4)(S_{0.4}Cl_{1.0}Br_{0.6})$ and LiCl are shown as green and orange ticks, respectively.

Reprinted with permission from American Chemical Society

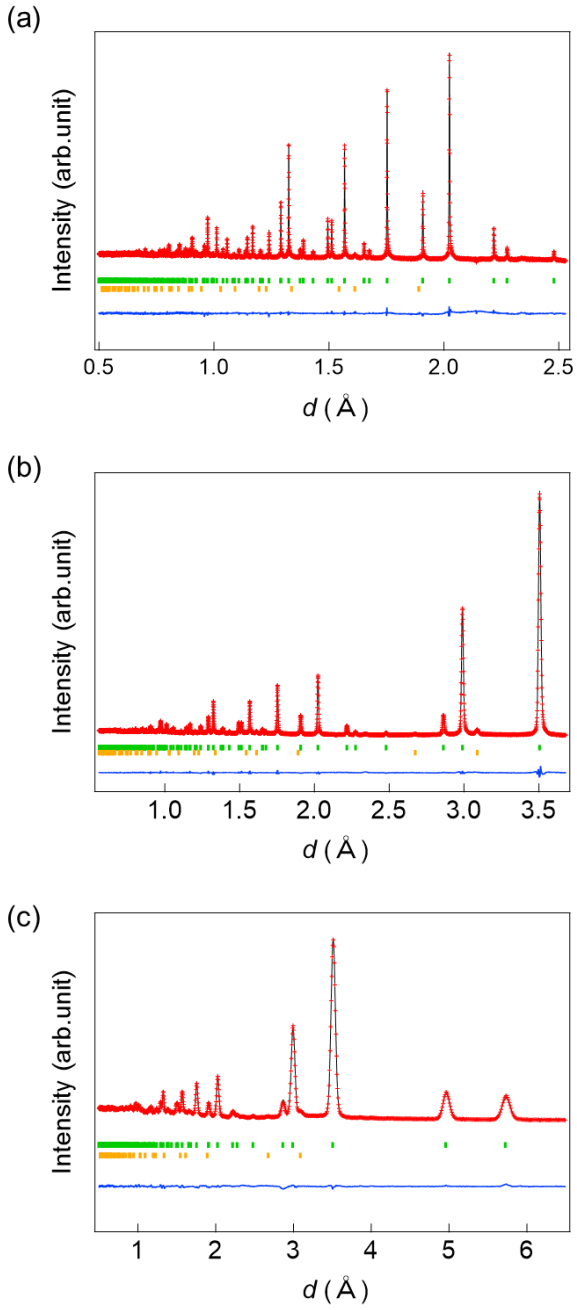

Figure 9. Neutron diffraction patterns and corresponding Rietveld refinement of $Li_{5.4}(PS_4)(S_{0.4}Cl_{0.6}Br_{1.0})$ (x = 0.6, y = 1.0). (a) BS blank data. (b) SE blank data. (c) LA35 blank data. Refinement was performed using data of BS, SE, and LA35 blanks simultaneously. Red ticks and black line represent observed diffraction data and calculated data, respectively; difference profile is shown in blue. Calculated Bragg reflections of $Li_{5.4}(PS_4)(S_{0.4}Cl_{1.0}Br_{0.6})$ and $LiCl_{0.41}Br_{0.59}$ are shown as green and orange ticks, respectively.

Reprinted with permission from American Chemical Society

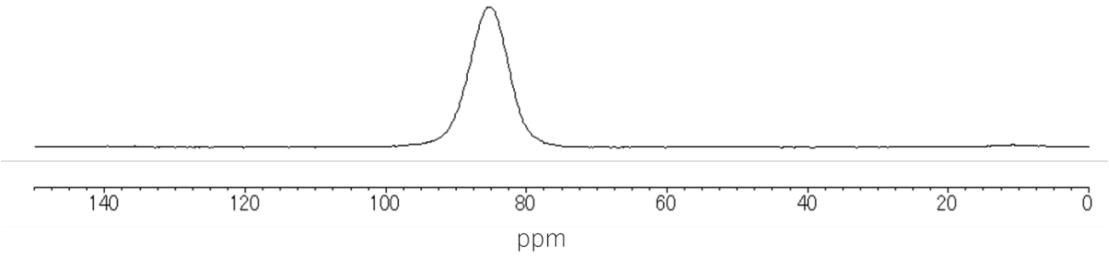

Figure 10. ^{31}P NMR spectrum of $Li_{5.4}(PS_4)(S_{0.4}Cl_{1.0}Br_{0.6})$($x$ = 1.0, y = 0.6). NMR measurement was performed on an ECA-500NMR (JEOL RESONANCE) spectrometer spun at 200.43 MHz. No evidence for bonding of P-Br, P-Cl, and Li_3PO_4 was observed, which would correspond to a peak at approximately 10 ppm.

Table 2. Constraints used for refinement of neutron diffraction patterns collected using $Li_{5.4}(PS_4)(S_{0.4}Cl_{1.0}Br_{0.6})$.

Atom	Site	Notation	x/a	y/b	z/c	Occ.	U_{iso} (Å^2)
Li	48h	48h	Li1(x)	1- Li1(x)	Li1(z)	0.45-1/3*Li2(Occ)- 1/2*Li3(Occ)-Li4(Occ)	Li1(U_{iso})
Li	16e	16e	Li2(x)	Li2(x)	Li2(x)	Li2(Occ)	Li1(U_{iso})
Li	24g	24g	Li3(x)	0.25	0.75	Li3(Occ)	Li1(U_{iso})
Li	48h	48h’	0.5+ Li4(x)	Li4(x)	Li4(z)	Li4(Occ)	Li1(U_{iso})
Br	4a	4a	0	0	1	Br1(Occ)	Br1(U_{iso})
Cl	4a	4a	0	0	1	Cl1((Occ)	Br1(U_{iso})
S	4a	4a	0	0	1	1- Br1(Occ)- Cl1((Occ)	Br1(U_{iso})
P	4b	4b	0	0	0.5	1	P1(U_{iso})
Br	4d	4d	0.25	0.25	0.75	0.6- Br1(Occ)	Br2(U_{iso})
Cl	4d	4d	0.25	0.25	0.75	1- Cl1((Occ)	Br2(U_{iso})
S	4d	4d	0.25	0.25	0.75	Br1(Occ)+ Cl1((Occ)-0.6	Br2(U_{iso})
S	16e	16e’	S3(x)	- S3(x)	0.5+ S3(x)	1	S3(U_{iso})

Reprinted with permission from American Chemical Society

Table 3. Structural parameters of $Li_{5.4}(PS_4)(S_{0.4}Cl_{1.0}Br_{0.6})$ refined by Rietveld method (neutron data).

Neutron diffraction							
Atom	Site	Notation	*x/a*	*y/b*	*z/c*	Occ.	U_{iso} (Å^2)
Li	48h	48h	0.31701(18)	0.68299(18)	0.0153(3)	0.3759(16)	0.0603(5)
Li	16e	16e	0.136(2)	0.136(2)	0.136(2)	0.0679(19)	0.0603(5)
Li	24g	24g	0.016(5)	0.25	0.75	0.027(2)	0.0603(5)
Li	48h	48h'	0.5748(14)	0.0748(14)	0.273(2)	0.038(2)	0.0603(5)
Br	4a	4a	0	0	1	0.3959(4)	0.0420(3)
Cl	4a	4a	0	0	1	0.4140(12)	0.0420(3)
S	4a	4a	0	0	1	0.1901(9)	0.0420(3)
P	4b	4b	0	0	0.5	1	0.0346(3)
Br	4d	4d	0.25	0.25	0.75	0.2041(4)	0.0435(2)
Cl	4d	4d	0.25	0.25	0.75	0.5860(12)	0.0435(2)
S	4d	4d	0.25	0.25	0.75	0.2099(9)	0.0435(2)
S	16e	16e'	0.11789(6)	-0.11789(6)	0.61789(6)	1	0.0544(2)
$F\bar{4}3m$, a = 9.870036(8) Å, R_{wp} = 4.34 %, R_e = 2.65 %, χ^2 = 2.72, impurity: 0.6 wt%($LiCl_{0.81}Br_{0.19}$)							

Reprinted with permission from American Chemical Society

Table 4. Structural parameters obtained from Rietveld refinements of $Li_{5.4}(PS_4)(S_{0.4}Cl_{1.0}Br_{0.6})$ at 80 K (synchrotron data).

Atom	Site	Notation	x/a	y/b	z/c	Occ.	U_{iso} (Å^2)
Li	48h	48h	0.31701 (fix)	0.68299 (fix)	0.0153 (fix)	0.45	0.085(4)
Br	4a	4a	0	0	1	0.395(1)	0.0261(7)
Cl/S	4a	4a	0	0	1	0.605(1)	0.0261(7)
P	4b	4b	0	0	0.5	1	0.0240(7)
Cl/S	4d	4d	0.25	0.25	0.75	0.795(1)	0.0199(6)
Br	4d	4d	0.25	0.25	0.75	0.205(1)	0.0199(6)
S	16e	16e’	0.12087(9)	-0.12087(9)	0.62087(9)	1	0.0440(4)
$F\bar{4}3m$, a = 9.8205(1) Å, R_{wp} = 3.12 %, R_p = 1.74 %, χ^2 = 1.16, impurity: 0.6 wt%($LiCl_{0.81}Br_{0.19}$)							

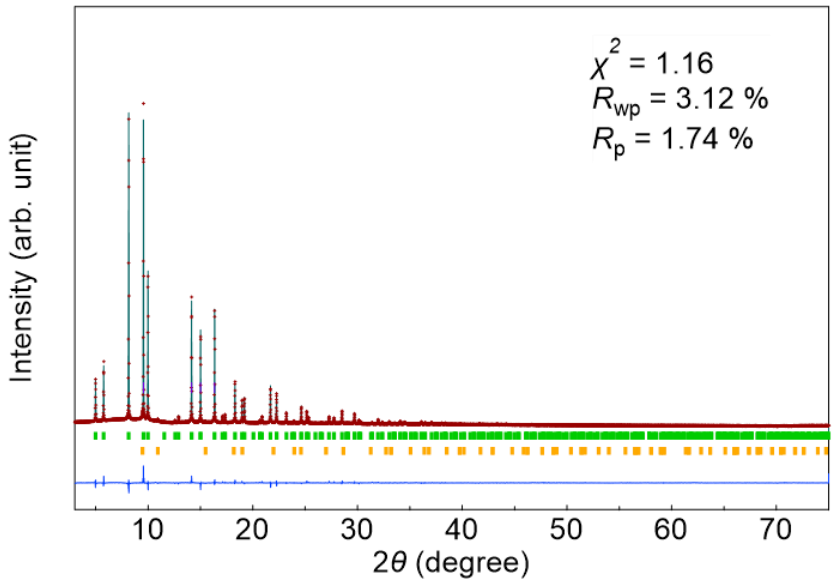

Figure 11. Synchrotron XRD pattern at 80 K and corresponding Rietveld refinement of $Li_{5.4}(PS_4)(S_{0.4}Cl_{1.0}Br_{0.6})$ (x = 1.0, y = 0.6). Red ticks and black line represent observed diffraction data and calculated data, respectively; difference profile is shown in blue. Calculated Bragg reflections of $Li_{5.4}(PS_4)(S_{0.4}Cl_{1.0}Br_{0.6})$ and $LiCl_{0.81}Br_{0.19}$ are shown as green and orange ticks, respectively.

Reprinted with permission from American Chemical Society

Table 5. Structural parameters obtained from Rietveld refinement of neutron data of $Li_{5.4}(PS_4)(S_{0.4}Cl_{1.6})$ (x = 1.6, y = 0.0). Constraints of lithium site occupancy were applied similarly to that for $Li_{5.4}(PS_4)(S_{0.4}Cl_{1.0}Br_{0.6})$.

Neutron diffraction							
Atom	Site	Notation	x/a	y/b	z/c	Occ.	U_{iso} (Å^2)
Li	48h	48h	0.32207(16)	0.67793(16)	0.0203(2)	0.3813(11)	0.0650(5)
Li	16e	16e	0.1513(11)	0.1513(11)	0.1513(11)	0.0569(17)	0.0650(5)
Li	24g	24g	0.016(6)	0.25	0.75	0.0191(15)	0.0650(5)
Li	48h	48h’	0.5705(9)	0.0705(9)	0.2725(13)	0.0402(8)	0.0650(5)
Cl	4a	4a	0	0	1	0.7059(3)	0.0359(3)
S	4a	4a	0	0	1	0.2941(3)	0.0359(3)
P	4b	4b	0	0	0.5	1	0.0409(2)
Cl	4d	4d	0.25	0.25	0.75	0.8941(3)	0.04730(16)
S	4d	4d	0.25	0.25	0.75	0.1059(3)	0.04730(16)
S	16e	16e’	0.11866(6)	-0.11866(6)	0.61866(6)	1	0.06146(19)
$F\bar{4}3m$, a = 9.803613(8) Å, R_{wp} = 4.63 %, R_e = 2.65 %, χ^2 = 3.06, impurity: 0.6 wt%(LiCl)							

Reprinted with permission from American Chemical Society

Table 6. Structural parameters obtained from Rietveld refinements of $Li_{5.4}(PS_4)(S_{0.4}Cl_{1.6})$ at 80 K (synchrotron data).

Atom	Site	Notation	x/a	y/b	z/c	Occ.	U_{iso} (Å^2)
Li	48h	48h	0.32207 (fix)	0.67793 (fix)	0.02030 (fix)	0.45	0.064(2)
Cl/S	4a	4a	0	0	1	1	0.0240(3)
P	4b	4b	0	0	0.5	1	0.0176(3)
Cl/S	4d	4d	0.25	0.25	0.75	1	0.0228(3)
S	16e	16e’	0.12020(8)	-0.12020(8)	0.62020(8)	1	0.0422(2)
$F\bar{4}3m$, a = 9.7627(2) Å, R_{wp} = 6.67 %, R_e = 4.41 %, χ^2 = 2.28, impurity: 0.8 wt%(LiCl)							

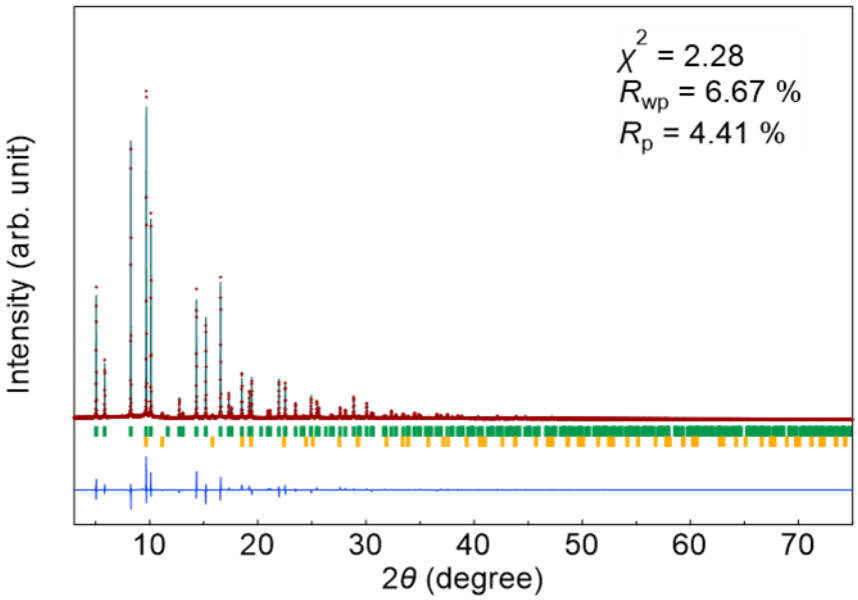

Figure 12. Synchrotron X-ray diffraction pattern at 80 K and corresponding Rietveld refinement of $Li_{5.4}(PS_4)(S_{0.4}Cl_{1.6})$ (x = 1.6). Constraints are applied similarly to that for $Li_{5.4}(PS_4)(S_{0.4}Cl_{1.0}Br_{0.6})$. Red ticks and black line represent observed diffraction data and calculated data, respectively; difference profile is shown in blue. Calculated Bragg reflections of $Li_{5.4}(PS_4)(S_{0.4}Cl_{1.6})$ and LiCl are shown as green and orange ticks, respectively.

Reprinted with permission from American Chemical Society

Table 7. Structural parameters of $Li_{5.4}(PS_4)(S_{0.4}Cl_{0.6}Br_{1.0})$ ($x = 0.6$, $y = 1.0$) obtained from neutron diffraction pattern refined by Rietveld method. Constraints of lithium site occupancy were applied in a similar manner to that for $Li_{5.4}(PS_4)(S_{0.4}Cl_{1.0}Br_{0.6})$.

Neutron diffraction							
Atom	Site	Notation	*x/a*	*y/b*	*z/c*	Occ.	U_{iso} (Å^2)
Li	48h	48h	0.3149(2)	0.6851(2)	0.0148(2)	0.3743(17)	0.0657(6)
Li	16e	16e	0.137(2)	0.137(2)	0.137(2)	0.054(2)	0.0657(6)
Li	24g	24g	0.025(2)	0.25	0.75	0.056(2)	0.0657(6)
Li	48h	48h’	0.5732(19)	0.0732(19)	0.278(3)	0.0296(13)	0.0657(6)
Br	4a	4a	0	0	1	0.6677(4)	0.0427(3)
Cl	4a	4a	0	0	1	0.2105(13)	0.0427(3)
S	4a	4a	0	0	1	0.1218(9)	0.0427(3)
P	4b	4b	0	0	0.5	1	0.0318(3)
Br	4d	4d	0.25	0.25	0.75	0.3323(4)	0.0401(2)
Cl	4d	4d	0.25	0.25	0.75	0.3895(13)	0.0401(2)
S	4d	4d	0.25	0.25	0.75	0.2782(9)	0.0401(2)
S	16e	16e’	0.11796(5)	-0.11796(5)	0.61796(5)	1	0.0509(2)
$F\bar{4}3m$, a = 9.915382(9) Å, R_{wp} = 4.64 %, R_e = 2.83 %, χ^2 = 2.69, impurity: 0.5 wt% ($LiCl_{0.41}Br_{0.59}$)							

Reprinted with permission from American Chemical Society

Table 8. Structural parameters obtained from Rietveld refinements of $Li_{5.4}(PS_4)(S_{0.4}Cl_{0.6}Br_{1.0})$ laboratory XRD data at room temperature (290 K to 300 K).

Atom	Site	Notation	x/a	y/b	z/c	Occ.	U_{iso} (Å^2)
Li	48h	48h	0.3149 (fix)	0.6851 (fix)	0.0148 (fix)	0.45	0.104(8)
Br	4a	4a	0	0	1	0.698(2)	0.027(1)
Cl/S	4a	4a	0	0	1	0.302(2)	0.027(1)
P	4b	4b	0	0	0.5	1	0.015(1)
Cl/S	4d	4d	0.25	0.25	0.75	0.698(2)	0.024(1)
Br	4d	4d	0.25	0.25	0.75	0.302(2)	0.024(1)
S	16e	16e’	0.12087(9)	-0.12087(9)	0.62087(9)	1	0.0341(7)

$F\bar{4}3m$, a = 9.9420(3) Å, R_{wp} = 6.17 %, R_e = 4.82 %, χ^2 = 1.57, impurity: 2.4 wt% ($LiCl_{0.41}Br_{0.59}$)

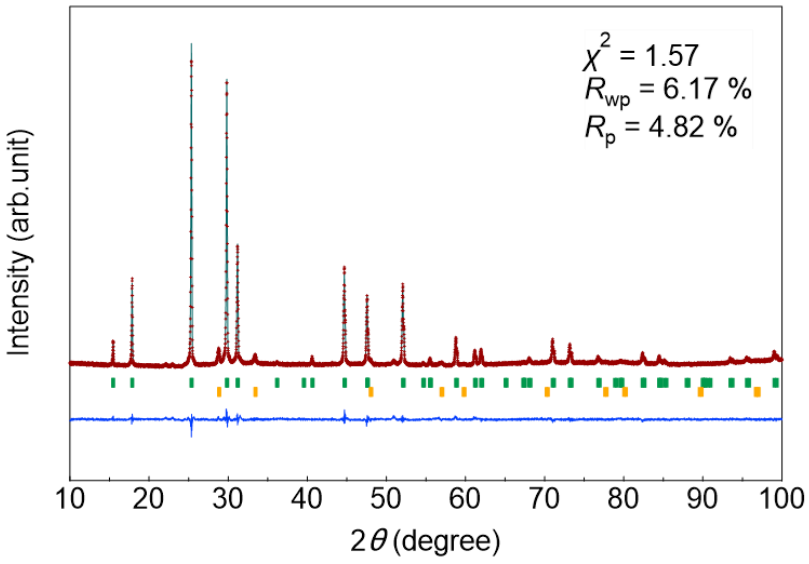

Figure 13. Laboratory XRD pattern at room temperature (290 to 300 K) and corresponding Rietveld refinement of $Li_{5.4}(PS_4)(S_{0.4}Cl_{0.6}Br_{1.0})$ (x = 0.6, y = 1.0). Red ticks and black line represent observed diffraction data and calculated data, respectively; difference profile is shown in blue. Calculated Bragg reflections of $Li_{5.4}(PS_4)(S_{0.4}Cl_{0.6}Br_{1.0})$ and $LiCl_{0.41}Br_{0.59}$ are shown as green and orange ticks, respectively.

Reprinted with permission from American Chemical Society

Table 9. Structural parameters obtained from Rietveld refinements of $Li_{5.4}(PS_4)(S_{0.4}Br_{1.6})$ (x = 0.0, y = 1.6) at 80 K (synchrotron data). Lithium is distributed at sites 48h and 24g only.

Atom	Site	Notation	x/a	y/b	z/c	Occ.	U_{iso} (Å^2)
Li	48h	48h	0.315(1)	0.685(1)	0.007(1)	0.36(1)	0.028(3)
Li	24g	24g	0.014(6)	0.25	0.75	0.18(1)	0.028(3)
Br	4a	4a	0	0	1	0.944(3)	0.0202(6)
S	4a	4a	0	0	1	0.056(3)	0.0202(6)
P	4b	4b	0	0	0.5	1	0.0170(7)
Br	4d	4d	0.25	0.25	0.75	0.656(3)	0.0148(5)
S	4d	4d	0.25	0.25	0.75	0.344(3)	0.0148(5)
S	16e	16e’	0.1193(1)	-0.1193(1)	0.6193(1)	1	0.0273(4)
$F\bar{4}3m$, a = 9.93098(6) Å, R_{wp} = 2.37%, R_p = 1.21%, χ^2 = 1.23, impurity: 0.1 wt% (LiBr)							

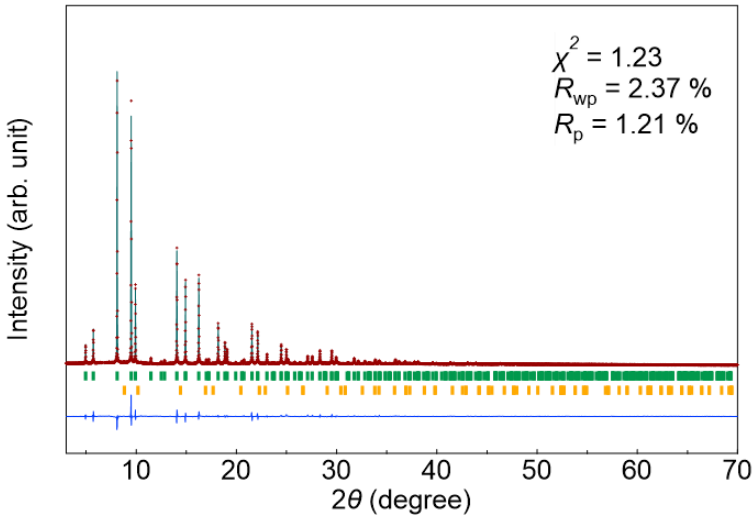

Figure 14. Synchrotron XRD pattern at 80 K and corresponding Rietveld refinement of $Li_{5.4}(PS_4)(S_{0.4}Br_{1.6})$ (x = 0.0, y = 1.6). Red ticks and black line represent observed diffraction data and calculated data, respectively; difference profile is shown in blue. Calculated Bragg reflections of $Li_{5.4}(PS_4)(S_{0.4}Br_{1.6})$ and LiBr are shown as green and orange ticks, respectively.

Reprinted with permission from American Chemical Society

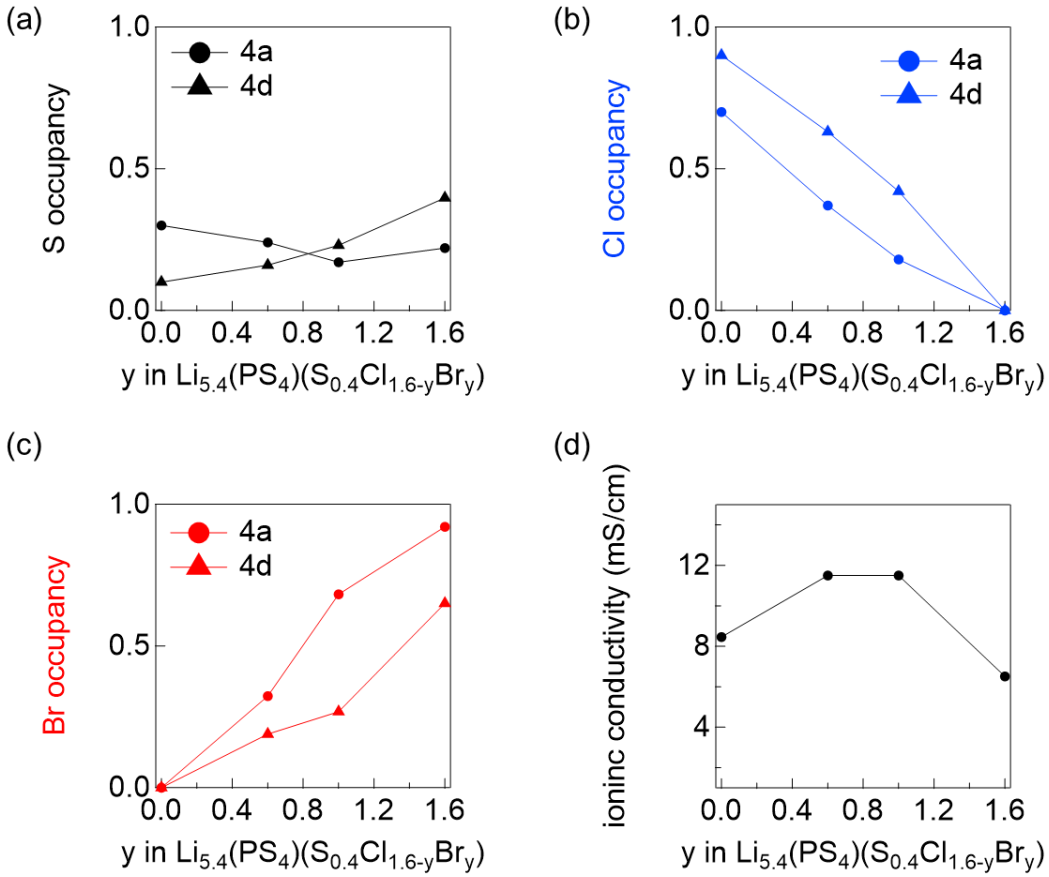

Figure 15. Site occupancy of sulfide, chloride, and bromide ions at 4a and 4d sites of $Li_{5.4}(PS_4)(S_{0.4}Cl_{1.6-y}Br_y)$ and composition dependence of lithium-ion conductivity. (a) Site occupancy of sulfide ion, (b) site occupancy of chloride ion, (c) site occupancy of bromide ion, and (d) ionic conductivity.

Figure 15 illustrates a series of anion-site occupancy compositions in $Li_{7-x-y}(PS_4)(S_{2-x-y}Cl_xBr_y)$ with ($x + y = 1.6$), calculated from the Rietveld refinement. As the bromide-ion substitution increases, the bromide ions preferentially occupy the 4a site instead of the 4d site. By contrast, chloride ions exhibited a trend opposite to that of the bromide-site distribution. As the chloride-ion substitution increased, chloride ions occupy the 4d site instead of the 4a site.[43] Hence, only the ternary compositions, $Li_{5.4}(PS_4)(S_{0.4}Cl_{1.0}Br_{0.6})$ and $Li_{5.4}(PS_4)(S_{0.4}Cl_{0.6}Br_{1.0})$, can exhibit the site disorder of chloride, sulfide, and bromide ions at both the 4d and 4a sites, with an ionic conductivity of up to 11.6 mS/cm. By

Reprinted with permission from American Chemical Society

contrast, the binary compositions $Li_{5.4}(PS_4)(S_{0.4}Cl_{1.6})$ and $Li_{5.4}(PS_4)(S_{0.4}Br_{1.6})$ do not exhibit such disorder and exhibit an ionic conductivity of only up to 8.5 mS/cm (Figure 15). This result is consistent with the relationship between the superionic conductivity and anion disorder at the 4a and 4d sites.[12]

2.3.3 Effect of Inter-cage Conduction Path and Its Length on Ionic Conductivity

No difference was noted between the conduction paths of binary $Li_{5.4}(PS_4)(S_{0.4}Cl_{1.6})$ (x = 1.6, y = 0) and ternary $Li_{5.4}(PS_4)(S_{0.4}Cl_{1.0}Br_{0.6})$ (x = 1.0, y = 0.6) or $Li_{5.4}(PS_4)(S_{0.4}Cl_{0.6}Br_{1,0})$ (x = 0.6, y = 1.0) compositions (Figures 5 (e) and 6). This similarity occurs because the total halogen content associated with the conduction path is greater than that associated with the disordered state at the 4a and 4d sites.[12] The MEM analysis results reveal that the 48h–16e–48h site conduction path is the inter-cage conduction path (Figure 5(e)). These results are incomparable with those obtained in previous studies, according to which the inter-cage conduction path involves the 48h′–48h′ (T2–T2) jump.[12] In our study, the occupancy of the 48h′ site is less than 0.05, whereas that of $Li_{6.0}(PS_4)(S_{1.0}Br_{1.0})$ is approximately 0.3.[12] Hence, the 48h′–48h′ (T2–T2) conduction results from the most occupied site, i.e., 48h; we also observed conduction paths including, 48h–48h′–48h′–48h (Figure 16(a)). Subsequently, we compared the length of 48h–48h′–48h′–48h to that of 48h–16e–48h (Figure 16(a)), both calculated using Rietveld refinements of neutron powder diffraction. The 48h–16e–48h conduction path is approximately 1.5 times shorter than 48h–48h′–48h′–48h (Figures 16(b) and (c)). This difference explains why the lithium conduction path of $Li_{5.4}(PS_4)(S_{0.4}Cl_{1.6})$ is different from that of $Li_{6.0}(PS_4)(S_{1.0}Br_{1.0})$, and may enhance the ionic conductivity of $Li_{6.0}(PS_4)(S_{1.0}Br_{1.0})$ from 2 to 8.5 mS/cm of $Li_{5.4}(PS_4)(S_{0.4}Cl_{1.6})$.

Reprinted with permission from American Chemical Society

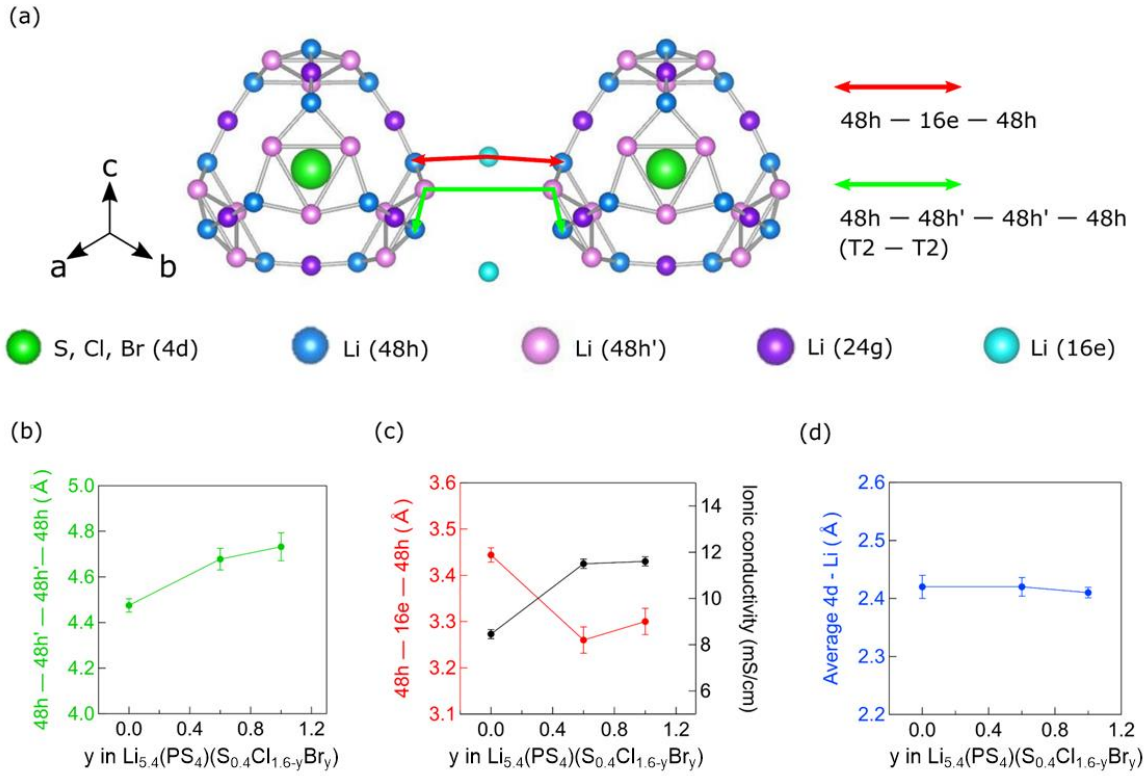

Figure 16. (a) Difference in inter-cage conduction paths of 48h–48h′–48h′–48h and 48h–16e–48h. Length of (b) 48h–48h′–48h′–48h site and (c) 48h–16e–48h site. (d) Average length of 4d site and Li (48h, 24g, and 48h′) around 4d site.

The site disorder in $Li_{6.0}(PS_4)(S_{1.0}Br_{1.0})$ increases the average length of the 4d site and lithium in the cage from 2.4 to 2.5 Å. Thus, the total path length for the inter-cage conduction decreases from 2.1 to 1.5 Å, leading to a four-fold increase in the ionic conductivity.[12] Our results suggest that the average lengths of the 4d site and lithium in the cage are similar (Figure 16(d)). On the contrary, the 48h–16e–48h path length, which corresponds to inter-cage conduction, clearly changes. The 48h–16e–48h path length in $Li_{5.4}(PS_4)(S_{0.4}Cl_{1.0}Br_{0.6})$ at 3.26(3) Å or in $Li_{5.4}(PS_4)(S_{0.4}Cl_{0.6}Br_{1,0})$ (3.30(3) Å) is shorter than that of $Li_{5.4}(PS_4)(S_{0.4}Cl_{1.6})$ (3.44(2) Å) (Figure 16(c)). The shorter 48h–16e–48h distance appears to enhance the ionic conductivity from 8.5 mS/cm in $Li_{5.4}(PS_4)(S_{0.4}Cl_{1.6})$

Reprinted with permission from American Chemical Society

to 11.6 mS/cm in $Li_{5.4}(PS_4)(S_{0.4}Cl_{1.0}Br_{0.6})$ or $Li_{5.4}(PS_4)(S_{0.4}Cl_{0.6}Br_{1,0})$ (Figure 16(c)); this observation is consistent with that of the proposed site disorder effect on ionic conductivity that is influenced by the shorter inter-cage conduction length.[12]

The activation energy for the lithium-ion conductivity of our samples (0.37–0.39 eV) was slightly higher than the reported value (approximately 0.30 eV).[8] This is because the contributions from the bulk and the grain boundary cannot be deconvoluted by the impedance spectra (Figure 17).[15] Thus, the ionic conductivity represents the ionic conductivity of both the bulk and the grain boundary. It has been proposed that the annealed pellet could reduce the grain boundary contribution.[8] In our experiments, the annealed powder was cold-pressed into a pellet. It is impossible to separate the grain boundary contribution using the impedance spectra of the cold-pressed samples. Hence, the apparent activation energy and Arrhenius pre-exponential factor appear to be higher than those of the previously reported values (Figure 17).[9] The activation energy and pre-exponential factor appear to follow the Meyer–Neldel rule,[44] according to which the activation energy is proportional to the Arrhenius pre-exponential factor.[45]

It has been speculated that the lattice softening reduces the Debye frequency, which consequently lowers the jump frequency and entropy of migration,[15] but this has not yet been confirmed. Some reports have stated that the ionic conductivity is affected by the activation energy, and by the Arrhenius pre-exponential factor.[46] This information can be used to design an optimum composition for enhanced ionic conductivity.[47] This phenomenon coincides with our scenario (Figure 17); however, in our scenario, the ionic conductivity depends on both the bulk and the grain boundaries.

Reprinted with permission from American Chemical Society

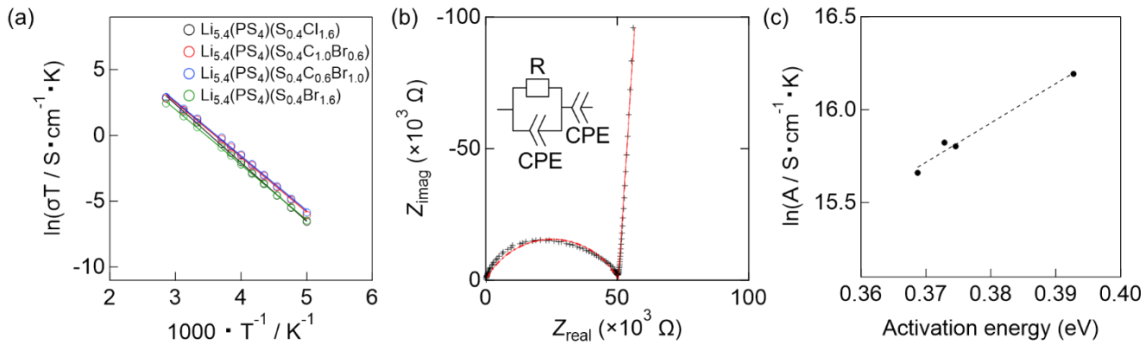

Figure 17. Conductivity results of $Li_{5.4}(PS_4)(S_{0.4}Cl_{1.6})$. (a) Arrhenius plot, (b) impedance spectrum at 200 K and equivalent circuit model, and (c) variations in ionic conductivity and Arrhenius pre-exponential factor (A) with increasing activation energy.

Recently, new superionic compounds comprising the argyrodite structure were devised by substitution.[48] To the best of our knowledge, this is the first study to propose the involvement of the 16e site in inter-cage conduction in $Li_{7-x-y}(PS_4)(S_{2-x-y}Cl_xBr_y)$ compositions with ($x + y > 1$), although compositions such as $Li_6(P_{1-\alpha},Ge_\alpha)S_5X$[49] and $Li_{6.15}Al_{0.15}Si_{1.35}S_{5.4}O_{0.6}$[41] with a lower halogen content may exhibit the involvement of the 16e site in inter-cage conduction.[50]

The effect of different ion conduction paths on the coulombic efficiency of the all-solid-state battery and the stability against Li metal was confirmed (Figures 18 and 19). The coulombic efficiency was 99.90(4) % at 99 cycles. The discharge capacity at 5 C was 64(6) % compared with the discharge capacity of the first cycle at 0.1 C (Figure 18), and the capacity retention rate of 100 cycles was 95(4) % at 0.1 C. This rate is 1.1 times higher than that of other all-solid-state batteries using $Li_{6.0}(PS_4)(S_{1.0}Cl_{1.0})$ at 35 cycles, although the alloy InLi was adopted as an anode.[51] The stability against Li metal is confirmed by the Li symmetry cell. It is reported that an increasing interfacial resistance has been observed upon prolonged stripping/plating in symmetric cells, when the electrolyte exhibits poor stability against Li metal.[8] In our scenario, the resistance of the Li

Reprinted with permission from American Chemical Society

symmetry cell does not increase for 48 h at different current densities (Figure 19). For $Li_{5.5}(PS_4)(S_{0.5}Cl_{1.5})$, the applied current was 0.25 mA/cm^2.[8] For $Li_{5.4}(PS_4)(S_{0.4}Cl_{1.0}Br_{0.6})$, the maximum current density was 3.0 mA/cm^2, indicating that $Li_{5.4}(PS_4)(S_{0.4}Cl_{1.0}Br_{0.6})$ is stable against Li metal.

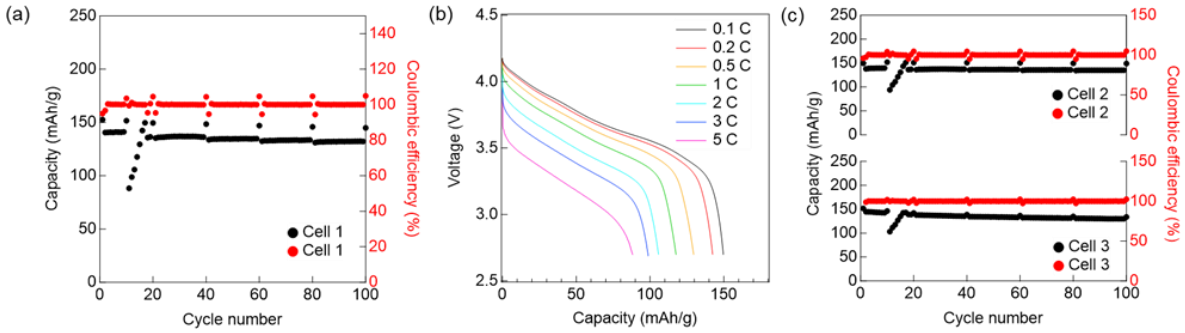

Figure 18. Cycling characteristics for charge–discharge capacity and efficiency for all-solid-state cell. Discharge rates at 1st, 9th, 16th, 19th, 39th, 59th, 79th, and 100th cycles are 0.1 C. Charge and discharge rate at cycles 10–14 are 5 C, 3 C, 2 C, 1 C, 0.5 C, respectively. Other charge and discharge cycles described above adopted 0.2 C. (b) Discharge capacity at different C rate. (c) Three cells were measured under same conditions. Coulombic efficiency of Cell 2 and Cell 3 at 99 cycles are 99.92 %, 99.94 %, respectively. Capacity retention rate of Cell 2 and Cell 3 at 100 cycles are 98 %, 88 %, respectively.

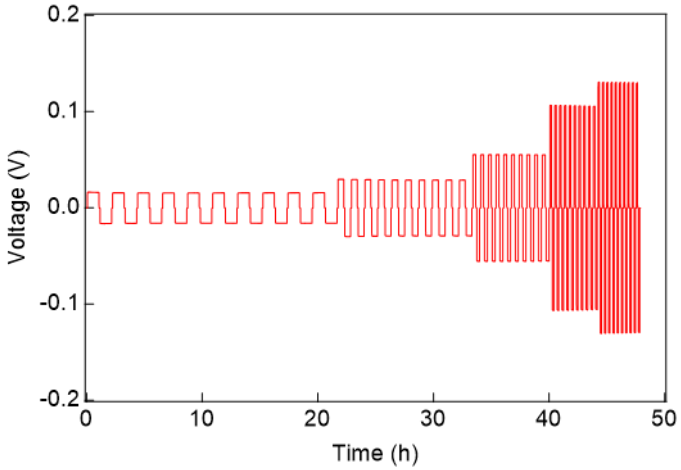

Figure 19. Stability against Li metal anode is measured using Li symmetry cell. Current densities used were 0.3, 0.6, 1.2, 2.4, and 3.0 mA/cm^2. Cut off current is set at 0.3 mAh/cm^2, and 20 total cycles were applied for each current density.

Reprinted with permission from American Chemical Society

2.4 Conclusion

A wide range of composition maps of $Li_{7-x-y}(PS_4)(S_{2-x-y}Cl_xBr_y)$ for ionic conductivity were discussed herein. $Li_{7-x-y}(PS_4)(S_{2-x-y}Cl_xBr_y)$ with x = 0.6–1.0 (y = 0.6–1.0) exhibited one of the highest ionic conductivities reported so far. The study also revealed that the 48h′–48h′ (T2–T2) is not the path for the inter-cage conduction in the halogen-rich $Li_{7-x-y}(PS_4)(S_{2-x-y}Cl_xBr_y)$ with ($x + y > 1$); instead, it is the 48h–16e–48h conduction path that is used because the 48h site shows the greatest occupancy. This result was supported by the combined BVS and MEM calculations. This is the first study to propose such a difference in the inter-cage conduction path of halogen-rich argyrodite. This difference in the conduction path also enhances the ionic conductivity from 2 mS/cm in $Li_{6.0}(PS_4)(S_{1.0}Br_{1.0})$ to 8.5 mS/cm in $Li_{5.4}(PS_4)(S_{0.4}Cl_{1.6})$. Additionally, the site disorder at the 4a and 4d sites enhances the ionic conductivity to 11.6 mS/cm in $Li_{5.4}(PS_4)(S_{0.4}Cl_{1.0}Br_{0.6})$ or $Li_{5.4}(PS_4)(S_{0.4}Cl_{0.6}Br_{1,0})$, owing to the shorter inter-cage conduction path. This insight may help further research on higher ionic conductivity in halogen-rich compositions with the argyrodite structure; the results obtained from further research may in turn accelerate the practical application of all-solid-state batteries. We plan on assembling an all-solid-state battery using a Li-metal anode in a future study.

2.5 References

1. Jacobson, M. Z. Review of Solutions to Global Warming, Air Pollution, and Energy Security. *Energy Environ. Sci.* **2009***, 2*, 148-173. DOI: 10.1039/B809990C

2. Hannan, M. A.; Lipu, M. S. H.; Hussain, A.; Mohamed, A. A Review of Lithium-Ion Battery State of Charge Estimation and Management System in Electric Vehicle Applications: Challenges and Recommendations. *Renew. Sustain. Energy Rev.* **2017**, *78*,

Reprinted with permission from American Chemical Society

834-854. DOI: 10.1016/j.rser.2017.05.001

3. Janek, J.; Zeier, W. G. A Solid Future for Battery Development. *Nat. Energy.* **2016**, *1*, 16141. DOI: 10.1038/nenergy.2016.141

4. Kato, Y.; Hori, S.; Saito, T.; Suzuki, K.; Hirayama, M.; Mitsui, A.; Yonemura, M.; Iba, H.; Kanno, R. High-Power All-Solid-State Batteries Using Sulfide Superionic Conductors. *Nat. Energy.* **2016,** *1*, 16030. DOI: 10.1038/nenergy.2016.30

5. Boulineau, S.; Tarascon, J. M.; Leriche, J. B.; Viallet, V. Electrochemical Properties of All-Solid-State Lithium Secondary Batteries Using Li-Argyrodite Li_6PS_5Cl as Solid Electrolyte. *Solid State Ionics.* **2013***, 242*, 45-48. DOI: 10.1016/j.ssi.2013.04.012

6. Wang, P.; Liu, H.; Patel, S.; Feng, X.; Chien, P.-H.; Wang, Y.; Hu, Y. Y. Fast Ion Conduction and Its Origin in $Li_{6-x}PS_{5-x}Br_{1+x}$. *Chem. Mater.* **2020**, *32*, 3833-3840. DOI: 10.1021/acs.chemmater.9b05331.

7. Feng, X.; Chien, P.-H.; Wang, Y.; Petel, S.; Wang, P.; Liu, H.; Immediato-Scuotto, M.; Hu, Y. Y. Enhanced Ion Conduction by Enforcing Structural Disorder in Li-Deficient Argyrodites $Li_{6-x}PS_{5-x}Cl_{1+x}$. *Energy. Stor. Mater.* **2020**, *30*, 67-73. DOI: 10.1016/j.ensm.2020.04.042

8. Adeli, P.; Bazak, J. D.; Park, K. H.; Kochetkov, I.; Huq, A.; Goward, G. R.; Nazar, L. F. Boosting Solid-State Diffusivity and Conductivity in Lithium Superionic Argyrodites by Halide Substitution. *Angew. Chem. Int Ed.* **2019**, *58*, 8681-8686. DOI: 10.1002/anie.201814222

9. Adeli, P.; Bazak, J. D.; Huq, A.; Goward, G. R.; Nazar, L. F. Influence of Aliovalent Cation Substitution and Mechanical Compression on Li-Ion Conductivity and Diffusivity in Argyrodite Solid Electrolytes. *Chem. Mater.* **2021**, *33*, 146-157. DOI: 10.1021/acs.chemmater.0c03090

Reprinted with permission from American Chemical Society

10. Suyama, M.; Kato, A.; Sakuda, A.; Hayashi, A.; Tatsumisago, M. Lithium Dissolution/Deposition Behavior with Li_3PS_4-LiI Electrolyte for All-Solid-State Batteries Operating at High Temperatures. *Electrochim*. *Acta*. **2018**, *286*, 158-162. DOI: 10.1016/j.electacta.2018.07.227

11. Epp, V.; Gün, Ö.; Deiseroth, H. J.; Wilkening, M. Highly Mobile Ions: Low-Temperature NMR Directly Probes Extremely Fast Li^+ Hopping in Argyrodite-Type Li_6PS_5Br. *J. Phys. Chem. Lett.* **2013**, *4*, 2118-2123. DOI: 10.1021/jz401003a

12. Gautam, A.; Sadowski, M.; Ghidiu, M.; Minafra, N.; Senyshyn, A.; Albe, K.; Zeier, W. G. Engineering the Site-Disorder and Lithium Distribution in the Lithium Superionic Argyrodite Li_6PS_5Br. *Adv. Energy Mater.* **2020**, *11*, 2003369. DOI: 10.1002/aenm.202003369

13. Patel, S. V.; Banerjee, S.; Liu, H.; Wang, P.; Chien, P. H.; Feng, X.; Liu, J.; Ong, S. P.; Hu, Y. Y. Tunable Lithium-Ion Transport in Mixed-Halide Argyrodites $Li_{6-x}PS_{5-x}ClBr_x$: An Unusual Compositional Space. *Chem. Mater.* **2021**, *33*, 1435-1443. DOI: 10.1021/acs.chemmater.0c04650

14. De Klerk, N. J. J.; Rosłoń, I.; Wagemaker, M. Diffusion Mechanism of Li Argyrodite Solid Electrolytes for Li-Ion Batteries and Prediction of Optimized Halogen Doping: The Effect of Li Vacancies, Halogens, and Halogen Disorder. *Chem. Mater.* **2016,** *28*, 7955-7963. DOI: 10.1021/acs.chemmater.6b03630

15. Kraft, M. A.; Culver, S. P.; Calderon, M.; Böcher, F.; Krauskopf, T.; Senyshyn, A.; Dietrich, C.; Zevalkink, A.; Janek, J.; Zeier, W. G. Influence of Lattice Polarizability on the Ionic Conductivity in the Lithium Superionic Argyrodites Li_6PS_5X (X = Cl, Br, I). *J. Am. Chem. Soc.* **2017**, *139*, 10909-10918. DOI: 10.1021/jacs.7b06327

16. Yu, C.; Li, Y.; Li, W.; Adair, K. R.; Zhao, F.; Willans, M.; Liang, J.; Zhao, Y.; Wang,

Reprinted with permission from American Chemical Society

C.; Deng, S.; Li, R.; Huang, H.; Lu, S.; Sham, T. K.; Huang, Y.; Sun, X. Enabling Ultrafast Ionic Conductivity in Br-Based Lithium Argyrodite Electrolytes for Solid-State Batteries with Different Anodes. *Energy Stor. Mater.* ***2020****, 30,* 238-249. DOI: 10.1016/j.ensm.2020.04.014

17. Subramanian, Y.; Rajagopal, R.; Ryu, K. S. Synthesis, Air Stability and Electrochemical Investigation of Lithium Superionic Bromine Substituted Argyrodite ($Li_{6-x}PS_{5-x}Cl_{1.0}Br_x$) for All-Solid-State Lithium Batteries. *J. Power Sources.* **2022**, *520*, 230849. DOI: 10.1016/j.jpowsour.2021.230849

18. Zhao, E.; He, L.; Zhang, Z.; Doux, J.-M.; Tan, D. H. S.; Wu, E. A.; Deysher, G.; Chen, Y.-T.; Zhao, J.; Wang, F.; Meng, Y. S. New Insights into Li Distribution in the Superionic Argyrodite Li_6PS_5Cl. *Chem. Commun.* **2021**, *57*, 10787-10790. DOI: 10.1039/d1cc03083c

19. Yu, C.; Li, Y.; Willans, M.; Zhao, Y.; Adair, K. R.; Zhao, F.; Li, W.; Deng, S.; Liang, J.; Banis, M. N.; Li, R.; Huang, H.; Zhang, L.; Yang, R.; Lu, S.; Huang, Y.; Sun, X. Superionic Conductivity in Lithium Argyrodite Solid-State Electrolyte by Controlled Cl-Doping. *Nano Energy.* **2020**, *69*, 104396. DOI: 10.1016/j.nanoen.2019.104396

20. Jung, W. D.; Kim, J. S.; Choi, S.; Kim, S.; Jeon, M.; Jung, H. G.; Chung, K. Y.; Lee, J. H.; Kim, B. K.; Lee, J. H.; Kim, H. Superionic Halogen-Rich Li-Argyrodites Using In Situ Nanocrystal Nucleation and Rapid Crystal Growth. *Nano Lett.* **2020**, *20*, 2303-2309. DOI: 10.1021/acs.nanolett.9b04597

21. Kitajima, S.; Ryu, S.; Ku, J.; Kim, S.; Park, Y.; Im, D. Methodology for Enhancing the Ionic Conductivity of Superionic Halogen-Rich Argyrodites for All-Solid-State Lithium Batteries. *Mater. Today Commun.* **2021**, *28*, 102727. DOI: 10.1016/j.mtcomm.2021.102727

Reprinted with permission from American Chemical Society

22. Cronau, M.; Szabo, M.; Roling, B. Single-Step Ball Milling Synthesis of Highly Li^+ Conductive $Li_{5.3}PS_{4.3}ClBr_{0.7}$ Glass Ceramic Electrolyte Enables Low-Impedance All-Solid-State Batteries. *Mater. Adv.* **2021**, *2*, 7842-7845. DOI: 10.1039/d1ma00784j

23. Gautam, A.; Ghidiu, M.; Suard, E.; Kraft, M. A.; Zeier, W. G. On the Lithium Distribution in Halide Superionic Argyrodites by Halide Incorporation in $Li_{7-x}PS_{6-x}Cl_x$. *ACS Appl. Energy Mater.* **2021**, *4,* 7309-7315. DOI: 10.1021/acsaem.1c01417

24. Wang, H.; Yu, C.; Ganapathy, S.; Van Eck, E. R. H.; Van Eijck, L.; Wagemaker, M. A Lithium Argyrodite $Li_6PS_5Cl_{0.5}Br_{0.5}$ Electrolyte with Improved Bulk and Interfacial Conductivity. *J. Power Sources.* **2019**, *412*, 29-36. DOI: 10.1016/j.jpowsour.2018.11.029

25. Peng, L.; Yu, C.; Zhang, Z.; Ren, H.; Zhang, J.; He, Z.; Yu, M.; Zhang, L.; Cheng, S.; Xie, J. Chlorine-Rich Lithium Argyrodite Enabling Solid-State Batteries with Capabilities of High Voltage, High Rate, Low-Temperature and Ultralong Cyclability. *Chem. Eng. J.* **2022**, *430*, 132896. DOI: 10.1016/j.cej.2021.132896

26. Masuda, N.; Kobayashi, Y.; Hernandez, O.; Bataille, T.; Paofai, S.; Suzuki, H.; Ritter, C.; Ichijo, N.; Noda, Y.; Takegoshi, K.; Tassel, C.; Yamamoto, T.; Kageyama, H. Hydride in $BaTiO_{2.5}H_{0.5}$: A Labile Ligand in Solid State Chemistry. *J. Am. Chem. Soc.* **2015**, *137*, 15315-25321. DOI: 10.1021/jacs.5b10255

27. Nagasaki, T.; Shiotani, S.; Igawa, N.; Yoshino, M.; Iwasaki, K.; Fukazawa, H.; Utsumi, W. Neutron Powder Diffraction and Difference Maximum Entropy Method Analysis of Protium- and Deuterium-Dissolved $BaSn_{0.5}In_{0.5}O_{2.75+\alpha}$. *J. Solid State Chem.* **2009**, *182*, 2632-2639. DOI: 10.1016/j.jssc.2009.06.024

28. Izumi, F.; Momma, K. Three-Dimensional Visualization in Powder Diffraction. *Solid State Phenom.* **2007**, *130*, 15-20. DOI: 10.4028/www.scientific.net/SSP.130.15

29. Ishikawa, Y.; Zhang, J. R.; Kiyanagi, R.; Yonemura, M.; Hoshikawa, A.; Ishigaki, T.;

Reprinted with permission from American Chemical Society

Torii, S.; Tomiyasu, R.; Kamiyama, T. Z-MEM and Z-3D, Maximum Entropy Method and Visualization Software for Electron/Nuclear Density Distribution in Z-Code, ICANS XXI: International Collaboration on Advanced Neutron Sources, DAA-P08, JPARC, Tokai, Japan, **2014**.

30. Sakata, M.; Sato, M. Accurate Structure Analysis by the Maximum-Entropy Method. *Acta Crystallogr. A.* **1990**, *46*, 263-270. DOI: 10.1107/S0108767389012377

31. Momma, K.; Izumi, F. VESTA 3 for Three-Dimensional Visualization of Crystal, Volumetric and Morphology Data. *J. Appl. Crystallogr.* **2011**, *44*, 1272-1276. DOI: 10.1107/S0021889811038970

32. Kobayashi, K.; Sakka, Y.; Suzuki, T. S. Development of an Electrochemical Impedance Analysis Program Based on the Expanded Measurement Model. *J. Ceram. Soc. Jpn.* **2016**, *124*, 943-949. DOI: 10.2109/jcersj2.16120

33. Ohta, N.; Takada, K.; Zhang, L.; Ma, R.; Osada, M.; Sasaki, T. Enhancement of the High-Rate Capability of Solid-State Lithium Batteries by Nanoscale Interfacial Modification. *Adv. Mater.* **2006**, *18*, 2226-2229. DOI: 10.1002/adma.200502604

34. Gautam, A.; Sadowski, M.; Prinz, N.; Eickhoff, H.; Minafra, N.; Ghidiu, M.; Culver, S. P.; Albe, K.; Fässler, T. F.; Zobel, M.; Zeier, W. G. Rapid Crystallization and Kinetic Freezing of Site-Disorder in the Lithium Superionic Argyrodite Li_6PS_5Br. *Chem. Mater.* **2019**, *31*, 10178-10185. DOI: 10.1021/acs.chemmater.9b03852

35. Price, D. L.; Fernandez-Alonso, F. An Introduction to Neutron Scattering. *Exp. Methods Phys. Sci.* **2013**, *44*, 1-136. DOI: 10.1016/B978-0-12-398374-9.00001-2

36. Yubuchi, S.; Tsukasaki, H.; Sakuda, A.; Mori, S.; Hayashi, A.; Tatsumisago, M. Quantitative Analysis of Crystallinity in an Argyrodite Sulfide-Based Solid Electrolyte Synthesized via Solution Processing. *RSC Adv.* **2019**, *9*, 14465-14471. DOI:

Reprinted with permission from American Chemical Society

10.1039/c9ra00949c

37. Norberg, S. T.; Rahman, S. M. H.; Hull, S.; Knee, C. S.; Eriksson, S. G. The Proton Conducting Electrolyte $BaTi_{0.5}In_{0.5}O_{2.75}$: Determination of the Deuteron Site and Its Local Environment. *J. Phys. Condens. Matter.* **2013**, *25*, 454214.

38. Yashima, M.; Itoh, M.; Inaguma, Y.; Morii, Y. Crystal Structure and Diffusion Path in the Fast Lithium-Ion Conductor $La_{0.62}Li_{0.16}TiO_3$. *J. Am. Chem. Soc.* **2005**, *127*, 3491-3495. DOI: 10.1021/ja0449224

39. Morgan, B. J. Mechanistic Origin of Superionic Lithium Diffusion in Anion-Disordered Li_6PS_5X Argyrodites. *Chem. Mater.* **2021**, *33*, 2004-2018. DOI: 10.1021/acs.chemmater.0c03738

40. Huang, W.; Cheng, L.; Hori, S.; Suzuki, K.; Yonemura, M.; Hirayama, M.; Kanno, R. Ionic Conduction Mechanism of a Lithium Superionic Argyrodite in the Li–Al–Si–S–O System. *Mater. Adv.* **2020**, *1*, 334-340. DOI: 10.1039/d0ma00115e

41. Lee, Y.; Jeong, J.; Lim, H. D.; Kim, S. O.; Jung, H. G.; Chung, K. Y.; Yu, S. Superionic Si-Substituted Lithium Argyrodite Sulfide Electrolyte $Li_{6+x}Sb_{1-x}Si_xS_5I$ for All-Solid-State Batteries. *ACS Sustainable Chem. Eng* **2021**, *9*, 120-128. DOI: 10.1021/acssuschemeng.0c05549

42. Ahmed, I.; Knee, C. S.; Karlsson, M.; Eriksson, S. -G.; Henry, P. F.; Matic, A.; Engberg, D.; Börjesson, L. Location of Deuteron Sites in the Proton Conducting Perovskite $BaZr_{0.5}0In_{0.50}O_{3-y}$. *J. Alloys Compd.* **2008**, *450*, 103-110. DOI: 10.1016/j.jallcom.2006.11.154

43. Inagaki, M.; Suzuki, K.; Hori, S.; Yoshino, K.; Matsui, N.; Yonemura, M.; Hirayama, M.; Kanno, R. Conduction Mechanism of $Li_{10}GeP_2S_{12}$-Type Lithium Superionic Conductors in a Li-Sn-Si-P-S System. *Chem. Mater.* **2019**, *31*, 3485-3490.

Reprinted with permission from American Chemical Society

44. Meyer, W.; Neldel, H. Relation between the Energy Constant and the Quantity Constant in the Conductivity-Temperature Formula of Oxide Semiconductors. *Z. Technol. Phys.* **1937**, *12*, 588.

45. Krauskopf, T.; Muy, S.; Culver, S. P.; Ohno, S.; Delaire, O.; Shao-Horn, Y.; Zeier, W. G. Comparing the Descriptors for Investigating the Influence of Lattice Dynamics on Ionic Transport Using the Superionic Conductor $Na_3PS_{4-x}Se_x$. *J. Am. Chem. Soc.* **2018**, *140*, 14464-14473. DOI: 10.1021/jacs.8b09340

46. Ngai, K. L. Meyer−Neldel Rule and Anti Meyer−Neldel Rule of Ionic Conductivity: Conclusions from the Coupling Model. *Solid State Ionics.* **1998**, *105*, 231-235. DOI: 10.1016/S0167-2738(97)00469-4

47. Muy, S.; Bachman, J. C.; Chang, H.-H.; Giordano, L.; Maglia, F.; Lupart, S.; Lamp, P.; Zeier, W. G.; Shao-Horn, Y. Lithium Conductivity and Meyer-Neldel Rule in Li_3PO_4–Li_3VO_4–Li_4GeO_4 Lithium Superionic Conductors. *Chem. Mater.* **2018**, *30*, 5573-5582. DOI: 10.1021/acs.chemmater.8b01504

48. Kraft, M. A.; Ohno, S.; Zinkevich, T.; Koerver, R.; Culver, S. P.; Fuchs, T.; Senyshyn, A.; Indris, S.; Morgan, B. J.; Zeier, W. G. Inducing High Ionic Conductivity in the Lithium Superionic Argyrodites $Li_{6+x}P_{1-x}Ge_xS_5I$ for All-Solid-State Batteries. *J. Am. Chem. Soc.* **2018**, *140*, 16330-16339. DOI: 10.1021/jacs.8b10282

49. Hogrefe, K.; Minafra, N.; Hanghofer, I.; Banik, A.; Zeier, W. G.; Wilkening, H. M. R. Opening Diffusion Pathways through Site Disorder: The Interplay of Local Structure and Ion Dynamics in the Solid Electrolyte $Li_{6+x}P_{1-x}Ge_xS_5I$ as Probed by Neutron Diffraction and NMR. *J. Am. Chem. Soc.* **2022**, *144*, 1795-1812. DOI: 10.1021/jacs.1c11571

50. Schlenker, R.; Hansen, A. L.; Senyshyn, A.; Zinkevich, T.; Knapp, M.; Hupfer, T.; Ehrenberg, H.; Indris, S. Structure and Diffusion Pathways in Li_6PS_5Cl Argyrodite from

Reprinted with permission from American Chemical Society

Neutron Diffraction, Pair-Distribution Function Analysis, and NMR. *Chem. Mater.* **2020**, *32*, 8420-8430. DOI: 10.1021/acs.chemmater.0c02418

51. Doux, J. M.; Yang, Y.; Tan, D. H. S.; Nguyen, H.; Wu, E. A.; Wang, X.; Banerjee, A.; Meng, Y. S. Pressure Effects on Sulfide Electrolytes for All Solid-State Batteries. *J. Mater. Chem. A.* **2020**, *8*, 5049-5055. DOI: 10.1039/c9ta12889a

Reprinted with permission from American Chemical Society

3. Electrochemical Stability of $Li_{5.4}(PS_4)(S_{0.4}Cl_{1.0}Br_{0.6})$ in All-Solid-State Battery Comprising $LiNbO_3$-Coated $Li(Ni_{0.8}Co_{0.1}Mn_{0.1})O_2$ Cathode and Lithium Metal Anode

3.1 introduction

Over the years, various high-performance lithium-ion rechargeable batteries have been developed to address global warming[1] and realize a sustainable, carbon-neutral society.[2] All-solid-state lithium-ion batteries offer a potential solution to reach this goal.[3,4] The performance of such batteries primarily depends on the electrochemical properties of the electrolyte.[5] However, all-solid-state lithium-ion batteries have disadvantages such as low rate capabilities and energy densities. Thus, the application of such batteries is limited because of a lack of suitable electrolytes that exhibit high ionic conductivities.[6] Recent studies have shown that lithium–phosphorus–sulfide solid electrolytes are promising materials [7] because of their high ionic conductivities,[8] mechanical softness,[9] and facile processing.[10]

Among the phosphorus sulfides, various $Li_{7-\alpha}PS_{6-\alpha}X_\alpha$ (X = Cl, Br, I) argyrodites that exhibit high ionic conductivities have been discovered.[11-17] These argyrodites are denoted as $Li_{7-\alpha}(PS_4)(S_{2-\alpha}X_\alpha)$.[18] Recently, high lithium-ion conductivity was measured in $Li_{7-x-y}(PS_4)(S_{2-x-y}Cl_xBr_y)$.[11-18] Particularly, $Li_{5.4}(PS_4)(S_{0.4}Cl_{1.0}Br_{0.6})$ demonstrate the highest ionic conductivity among the $Li_{7-x-y}(PS_4)(S_{2-x-y}Cl_xBr_y)$ systems.[18] The high stability of $Li_{5.4}(PS_4)(S_{0.4}Cl_{1.0}Br_{0.6})$ against reaction with lithium metal has been reported.[18] High Coulombic efficiency, discharge capacity, and capacity retention rate values of an all-solid-state battery using $Li_{5.4}(PS_4)(S_{0.4}Cl_{1.0}Br_{0.6})$ have also been reported.[18] Another study used $Li(Ni_{0.8}Co_{0.15}Al_{0.05})O_2$ and artificial graphite (AG) as the

Reprinted with permission from Journal of the Electrochemical Society

cathode and anode, respectively, in all-solid-state batteries, as these materials are known to exhibit high Coulombic efficiencies.[19] The same cathode and anode materials were used in our previous study.[18]

To develop new batteries with higher energy densities, the use of a cathode that can operate at relatively high voltages (up to 0.1 V) is preferable. For example, $Li(Ni_{0.8}Co_{0.1}Mn_{0.1})O_2$ is a candidate material for high-voltage operation.[20,21] However, its use as a cathode material requires that the $Li_{5.4}(PS_4)(S_{0.4}Cl_{0.1}Br_{0.6})$ electrolyte possess sufficiently high chemical stability to withstand high-voltage operation. Consequently, the applicability of this cathode material has not yet been verified.

In this study, the chemical stability of $Li_{5.4}(PS_4)(S_{0.4}Cl_{1.0}Br_{0.6})$ and the reactivities of $Li_{5.4}(PS_4)(S_{0.4}Cl_{1.0}Br_{0.6})$ and $Li(Ni_{0.8}Co_{0.1}Mn_{0.1})O_2$ in Li | $Li_{5.4}(PS_4)(S_{0.4}Cl_{1.0}Br_{0.6})$ | $Li(Ni_{0.8}Co_{0.1}Mn_{0.1})O_2$–$Li_{5.4}(PS_4)(S_{0.4}Cl_{1.0}Br_{0.6})$ batteries were investigated using battery cycling tests over 50 cycles, followed by X-ray diffraction (XRD) analysis to evaluate the phase stability.

3.2 Experimental

3.2.1 Synthesis of the solid electrolyte

The $Li_{5.4}(PS_4)(S_{0.4}Cl_{0.1}Br_{0.6})$ powder used as the electrolyte layer was synthesized using the same protocol as in our previous study.[18] A composite composed of a solid electrolyte and an active material, $Li(Ni_{0.8}Co_{0.1}Mn_{0.1})O_2$, was employed as the cathode. Pulverized solid-electrolyte powder was used as the cathode because small-particle solid-electrolyte powders provide an effective interface with intimate contact between the active materials in the cathode layer.[22]

The electrolyte powder was placed in a ZrO_2 pot (1.0 g per pot) containing a ZrO_2 ball

Reprinted with permission from Journal of the Electrochemical Society

(0.5 mm diameter; 34 g), and 10.4 mL toluene (<5 ppm of moisture) was pipetted into the pot in an argon-filled glovebox. The moisture and oxygen levels in the glovebox were below

1 ppm. The mixture was then mechanically milled using a planetary ball mill (Fritsch Pulverisette 7) at 150 rpm for 2 h to obtain a fine slurry. After ball-milling, the samples were sieved and classified into beads and slurries in an argon-filled glovebox. To obtain the $Li_{5.4}(PS_4)(S_{0.4}Cl_{1.0}Br_{0.6})$ powder for the cathode layer, the slurry was heated to 373 K and dried using a Schlenk bottle under vacuum.

3.2.2 Particle-size distribution

The particle-size distribution of the $Li_{5.4}(PS_4)(S_{0.4}Cl_{1.0}Br_{0.6})$ cathode powder was measured using a laser diffraction particle-size analyzer (Partica LA-960, Horiba, Japan). The measurements were performed in toluene (>99.5% purity, with a moisture content of less than 10 ppm; Fujifilm Wako Pure Chemical Corporation, Japan), as previously reported.[18] Furthermore, the measurements were performed in a dry room maintained at a moisture content below 1 ppm.

3.2.3 Microscopy and elemental analysis

Scanning electron microscopy (SEM) measurements were performed using a Hitachi SU8220 instrument at an accelerating voltage of 2 kV and an emission current of

10 μA. Energy dispersive X-ray spectroscopy (EDS; Bruker X Flash5060FQ) was performed in the same field-of-view used to obtain the SEM images using an accelerating voltage of 10 kV and emission current of 5 μA.

Polished cross-sections of the pellet samples were prepared before SEM and EDS

Reprinted with permission from Journal of the Electrochemical Society

measurements using Ar-ion milling (IM-4000, Hitachi High-Tech). During the 5-h milling process, the accelerating voltage was 3.5 kV, and the sample was cooled to below 100 K using liquid nitrogen.

3.2.4 Synthesis of cathode mixtures

To improve battery performance, $LiNbO_3$ was coated onto the $Li(Ni_{0.8}Co_{0.1}Mn_{0.1})O_2$ powder particles (Shima Trading Company, Japan) using a solution containing lithium, niobium alkoxides, and ethanol, as described previously.[23] The thickness of the coated layer (4.2 nm) was calculated from the combination of the volume of the solution used for the coating, the Brunauer–Emmett–Teller (BET) surface area of $Li(Ni_{0.8}Co_{0.1}Mn_{0.1})O_2$, and the density of $LiNbO_3$.

Mixed cathode powders were prepared using $LiNbO_3$-coated $Li(Ni_{0.8}Co_{0.1}Mn_{0.1})O_2$ and $Li_{5.4}(PS_4)(S_{0.4}Cl_{1.0}Br_{0.6})$ in weight ratios of 7:3 (70NCM-30SE), 8:2 (80NCM-20SE), and 9:1 (90NCM-10SE). The cathode mixtures were placed in a ZrO_2 pot (1.0 g per pot) containing a ZrO_2 ball (2.0 mm diameter; 34 g) in an argon-filled glovebox for dry ball-milling. The mixture was mechanically milled using a planetary ball-milling apparatus (AV-1, Asahi Rika Factory. Ltd., Tokyo, Japan) at 600 rpm for 1 h. After ball-milling, the samples were sieved and classified into beads and powders in an argon-filled glovebox.

3.2.5 X-ray powder diffraction analysis

Two different laboratory XRD instruments were used to analyze the powder and pellet samples. The Bragg–Brentano geometry (Bruker D2 PHASER) was used to analyze the powder samples before conducting charge/discharge cycling tests. The divergence and Soller slit were set to 0.1 mm and 0.04°, respectively. The data were collected over a

Reprinted with permission from Journal of the Electrochemical Society

diffraction angle (2θ) range of 10–100° (step size = 0.01°) at a scanning rate of 1 s per step. The samples were packed in a flat folder and sealed using Kapton tape to prevent exposure to air. All measurements were performed at room temperature (290–300 K).

The second XRD instrument was a Bruker D8 ADVANCE, which was used to analyze the pellet samples after the charge/discharge cycling tests. The pellets were exposed to a horizontal X-ray beam (parallel to the pellet surface) by changing their vertical positions. The top of the pellets was identified by measuring the scattering intensity decay. The X-ray beam irradiated the detected top position of each pellet, and measurements were performed using a Bragg–Brentano geometry, with the divergence and Soller slit set to 0.1 mm and 0.025°, respectively. The data were collected over a 2θ range of 10–60° (step size = 0.02°) at a scanning rate of 4 s per step. During the measurements, the temperature was maintained at room temperature (290–300 K). The all-solid-state battery pellets were placed in a dome-like cell to avoid exposure to air. The thickness of the cathode mixture layer was 61 μm for 90NCM-10SE and 97 μm for 70NCM-30SE, as calculated based on the reported densities of $Li(Ni_{0.8}Co_{0.1}Mn_{0.1})O_2$ (4.8 g/cm^3) and $Li_{5.4}(PS_4)(S_{0.4}Cl_{1.0}Br_{0.6})$ (2.0 g/cm^3), respectively.[18,24] Even for the thickest cathode electrode layer of 97 μm, more than 99% of the incident X-ray intensity was diffracted. In this calculation, the mass absorption coefficient and mass fraction of each element and the densities of $Li(Ni_{0.8}Co_{0.1}Mn_{0.1})O_2$ and $Li_{5.4}(PS_4)(S_{0.4}Cl_{1.0}Br_{0.6})$ were used.[25] Therefore, the entire cathode mixture layer was analyzed using XRD.

3.2.6 Crystallite size

The crystallite sizes were calculated from the full-width at half-maximum (FWHM) of the peaks in the XRD pattern using the whole-pattern powder fitting method.[26] The

Reprinted with permission from Journal of the Electrochemical Society

diffraction peak profiles were modeled using a split-pseudo-Voigt function and an 11th-order Legendre orthogonal polynomial background model using the Rietan-FP software.[26] For $Li_{5.4}(PS_4)(S_{0.4}Cl_{1.0}Br_{0.6})$, the crystallite size was calculated using Scherrer's equation along the (200) direction from the diffraction peak of $2\theta = 25°$, with a shape factor of 0.9.[27]

3.2.7 All-solid-state battery cell fabrication and electrochemical measurements

A battery with a Li | $Li_{5.4}(PS_4)(S_{0.4}Cl_{1.0}Br_{0.6})$ | $Li(Ni_{0.8}Co_{0.1}Mn_{0.1})O_2$–$Li_{5.4}(PS_4)(S_{0.4}Cl_{1.0}Br_{0.6})$ structure was fabricated. The total amount of cathode active material was 18 mg. Lithium foil (10 mm diameter, 0.2 mm thickness; Honjo Metal, Japan) was used as the anode. The solid electrolyte (100 mg) was pressed into 10-mm-diameter pellets at 300 MPa. Thereafter, the cathode mixtures were pressed into 10-mm-diameter pellets at 600 MPa to form a cathode electrode layer. Finally, lithium metal was attached to the opposite side of the cathode and pressed at 100 MPa.

Electrochemical measurements were performed while the battery pellets were loaded at a pressure of 20 MPa using a screw and torque wrench. The battery was charged and discharged between 2.5 and 4.3 V at 298 K using a potentiogalvanostat (VMP-3, Biologic, France). The atmosphere contained less than 1 ppm of moisture and oxygen. The current density was fixed at 0.24 or 1.2 mA/cm^2, corresponding to 0.1C and 0.5C, respectively. Impedance spectra were collected using the potentiogalvanostat. The charge and discharge capacity values at the 1st, 2nd, 10th, 20th, 30th, 40th, and 50th cycles were measured at 0.1C. The values at all other cycles were measured at 0.5C to accelerate the capacity degradation. Impedance spectra were collected at the 1st, 10th, 20th, 30th, 40th, and 50th cycles under a state of charge (SOC) of 0%, 50%, and 100%. Before conducting the

Reprinted with permission from Journal of the Electrochemical Society

impedance measurements, the charge and discharge operations were stopped for 5 min. Impedance spectra were measured for the open-cell state with a voltage amplitude of 10 mV over a frequency range of 10^6 to 0.01 Hz at 298 K. All measurements were conducted under 1 ppm of moisture and oxygen. In the case of an all-solid-state battery comprising a sulfide solid electrolyte, it has previously been reported that 300 to 600 MPa was applied to manufacture the pellet and 10 to 70 MPa during cycling.[18,23,28,29]

3.2.8 Partial ionic and electronic conductivity measurements of cathode mixtures

The ionic conductivities of the cathode mixtures were measured using an electron-blocking cell with a Li | $Li_{5.4}(PS_4)(S_{0.4}Cl_{1.0}Br_{0.6})$ | $Li(Ni_{0.8}Co_{0.1}Mn_{0.1})O_2$–$Li_{5.4}(PS_4)(S_{0.4}Cl_{1.0}Br_{0.6})$ | $Li_{5.4}(PS_4)(S_{0.4}Cl_{1.0}Br_{0.6})$ | Li structure. Cathode mixtures (total weight: 200 mg) sandwiched with 50 mg of $Li_{5.4}(PS_4)(S_{0.4}Cl_{1.0}Br_{0.6})$ from both sides were pressed into 10-mm-diameter pellets under a pressure of 600 MPa. Subsequently, Li foil (10 mm φ, thickness: 0.2 mm; Honjo Metal, Japan) was applied on both ends and pressed at 100 MPa. Constant voltages (E_{app_i}) of 10, 20, 30, 40, and 50 mV were applied for 2 h. The resistance of the electron-blocking cell was calculated from the slope between E_{app_i} and current using the current and voltage values obtained after 2 h. The electron-blocking cell resistance includes the solid electrolyte and mixture resistances. The resistance of the solid electrolyte and cell length of $Li_{5.4}(PS_4)(S_{0.4}Cl_{1.0}Br_{0.6})$ (equivalent to 16.2 Ω and 7.4 × 10^{-2} cm at 100 mg, respectively) were calculated based on the literature[18] and subtracted from the electron-blocking cell resistance. The ionic conductivity was calculated using the surface area (0.785 cm^2), subtracted resistance, and cell length. The measurements were performed while the electron-blocking cell was compressed under a pressure of 20 MPa using a screw and torque wrench in an atmosphere with 1 ppm of

Reprinted with permission from Journal of the Electrochemical Society

moisture and oxygen.

The electronic conductivity of the cathode composites was measured using an ion-blocking electrode of stainless steel (SUS) | $Li(Ni_{0.8}Co_{0.1}Mn_{0.1})O_2$–$Li_{5.4}(PS_4)(S_{0.4}Cl_{1.0}Br_{0.6})$ | SUS. The ion-blocking electrode (total weight: 200 mg) was pressed into 10-mm-diameter pellets under 600 MPa. Thereafter, constant voltages (E_{app_e}) of 10, 20, 30, 40, and 50 mV were applied to the electrode pellets for 2 h, and the resistance of the composite was calculated from the slope between E_{app_e} and current. In this calculation, correction of the resistance of the solid electrolyte is not needed. The measurements were performed while the electrode pellets were compressed under a pressure of 20 MPa using a screw and torque wrench in an atmosphere with 1 ppm of moisture and oxygen.

3.3 Results and Discussion

3.3.1 Properties of as-prepared $Li_{5.4}(PS_4)(S_{0.4}Cl_{1.0}Br_{0.6})$ and mixed cathode powders

Pulverized solid-electrolyte powder was used as the cathode material to ensure good interfacial contact with the active materials in the cathode layer.[22] During pulverization, no byproduct phases were generated (Figure 1(a) (I) and (II)), as evidenced by the observation of XRD peaks that are only related to $Li_{5.4}(PS_4)(S_{0.4}Cl_{1.0}Br_{0.6})$. The milling of the $Li_{5.4}(PS_4)(S_{0.4}Cl_{1.0}Br_{0.6})$ used in the cathode changes the crystallite size in relation to that of the solid electrolyte, as identified by the changes in the FWHM of the (200) peak. This peak had the highest peak intensity, which simplified distinguishing between the background and the peak using the 11th-order Legendre orthogonal polynomial background model. Mechanical milling increases the FWHM value owing to a decrease in the crystallite size from 75.6 to 53.0 nm (Figure 1(b)). A decrease in the particle size

Reprinted with permission from Journal of the Electrochemical Society

of the powder from 43[18] to 1.5 μm was further confirmed by particle-size distribution and SEM analyses (results shown in Figure 2 (a) and (b), respectively). The differences in the crystallite and particle sizes indicate that the particles comprised aggregated crystallites and/or polycrystals composed of several crystallites.

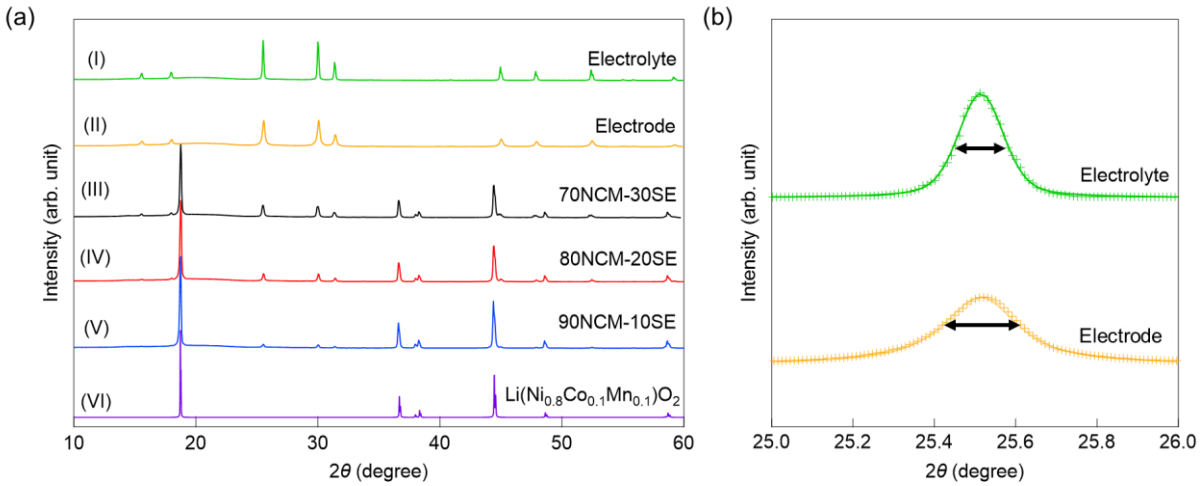

Figure 1. (a) XRD patterns of the $Li_{5.4}(PS_4)(S_{0.4}Cl_{1.0}Br_{0.6})$ powders used for the (I) electrolyte layer and (II) electrode layer and cathode mixtures of $Li(Ni_{0.8}Co_{0.1}Mn_{0.1})O_2$ and $Li_{5.4}(PS_4)(S_{0.4}Cl_{1.0}Br_{0.6})$: (III) 70NCM-30SE, (IV) 80NCM-20SE, and (IV) 90NCM-10SE. All measurements were performed at room temperature (290–300 K). (VI) The pattern of $Li(Ni_{0.8}Co_{0.1}Mn_{0.1})O_2$ (VI) was simulated using the literature lattice parameters.[30] (b) FWHM values (black arrows) were obtained from the (200) XRD peaks of $Li_{5.4}(PS_4)(S_{0.4}Cl_{1.0}Br_{0.6})$ extracted from the XRD patterns of the electrolyte and electrode powders. Crosses represent raw XRD data and the solid lines are fitted data using the split-pseudo-Voigt function.

The XRD patterns of the cathode mixtures are shown in Figure 1(a) (III)–(V). If $Li_{5.4}(PS_4)(S_{0.4}Cl_{1.0}Br_{0.6})$ reacts with $Li(Ni_{0.8}Co_{0.1}Mn_{0.1})O_2$[30] during the preparation of the mixed cathode, Li_3PO_4 should be observed as a decomposition product owing to the oxidation of the lithium–phosphorus–sulfide solid electrolyte.[29] In the present case, no peaks corresponding to byproduct phases were observed in the XRD patterns of the as-prepared cathode mixtures, and only $Li(Ni_{0.8}Co_{0.1}Mn_{0.1})O_2$ (Figure 1(a) (VI)) and

Reprinted with permission from Journal of the Electrochemical Society

$Li_{5.4}(PS_4)(S_{0.4}Cl_{1.0}Br_{0.6})$ (Figure 1(a) (I) and (II)) were identified. These results indicate that $Li_{5.4}(PS_4)(S_{0.4}Cl_{1.0}Br_{0.6})$ is stable during pulverization and mixing with $Li(Ni_{0.8}Co_{0.1}Mn_{0.1})O_2$.

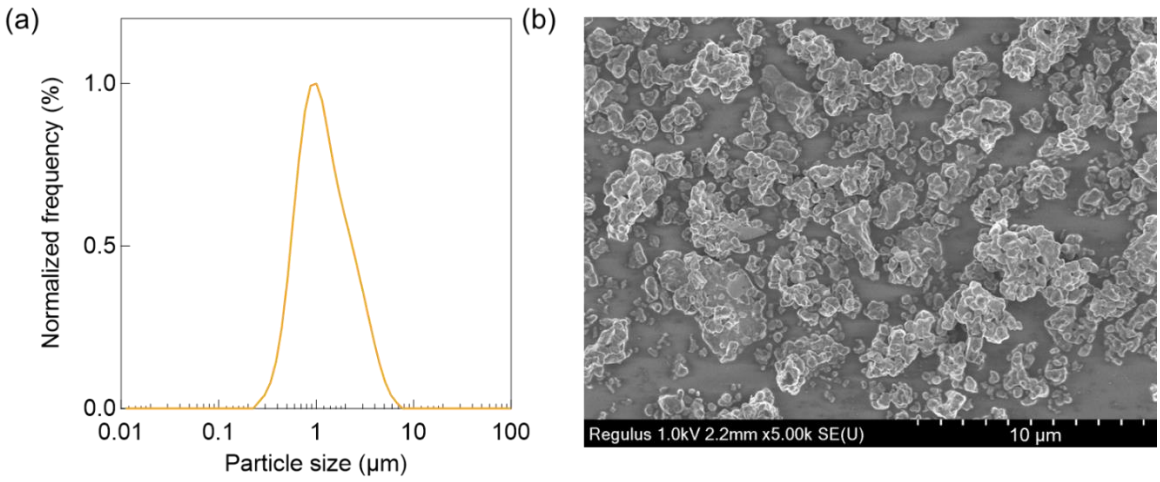

Figure 2. (a) Particle-size distribution (measured using laser diffraction in toluene) and (b) SEM image of $Li_{5.4}(PS_4)(S_{0.4}Cl_{1.0}Br_{0.6})$ used for the cathode layers. The powder has a median diameter of 1.5 μm.

3.3.2 Charge and discharge capacities of Li | $Li_{5.4}(PS_4)(S_{0.4}Cl_{1.0}Br_{0.6})$ | $Li(Ni_{0.8}Co_{0.1}Mn_{0.1})O_2$–$Li_{5.4}(PS_4)(S_{0.4}Cl_{1.0}Br_{0.6})$ batteries

Before investigating the all-solid-state battery, we first measured the stability of $Li_{5.4}(PS_4)(S_{0.4}Cl_{1.0}Br_{0.6})$ using linear sweep voltammetry. It has previously been reported that the cyclic voltammogram of the $Li_{5.5}(PS_4)(S_{1.0}Cl_{1.5})$ solid electrolyte showed negligible current during the voltage sweep.[8] This result indicates the stability of the $Li_{5.5}(PS_4)(S_{1.0}Cl_{1.5})$ solid electrolyte over the measured voltage window. The cyclic voltammogram of $Li_{5.4}(PS_4)(S_{0.4}Cl_{1.0}Br_{0.6})$ was measured to explore its stability during the voltage sweep. As shown in Figure 3, a negligible amount of current is observed

Reprinted with permission from Journal of the Electrochemical Society

during the voltage sweep, and the current decreased further after the second cycle. This result showed that $Li_{5.4}(PS_4)(S_{0.4}Cl_{1.0}Br_{0.6})$ is stable up to 10 V.

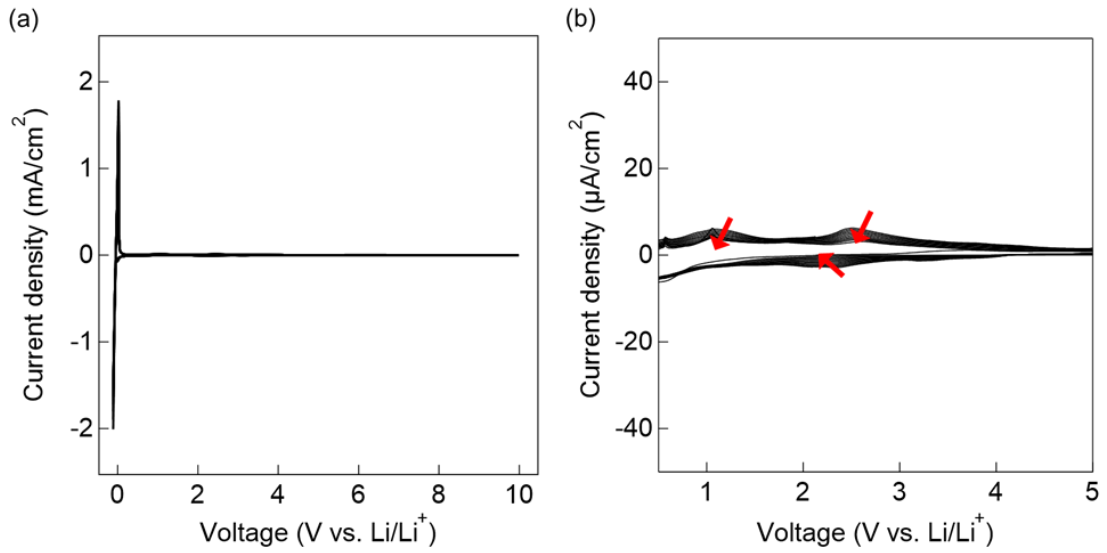

Figure 3. (a) Cyclic voltammogram using a stainless steel (SUS) | $Li_{5.4}(PS_4)(S_{0.4}Cl_{1.0}Br_{0.6})$ | Li | SUS cell. The cell structure is the same as that of the all-solid-state batteries except that the cathode is not inserted. A scan rate was 1 mV/s from −0.1 to 10.0 V and measurements were repeated 10 times. (b) Magnified view of the cyclic voltammogram from 0.5 to 5.0 V. The red arrows represent the decreasing current with the number of voltage sweeps.

The battery using the 90NCM-10SE cathode mixture exhibited a higher discharge capacity than the other batteries, although the Coulombic efficiencies of all batteries were approximately 100% (Figure 4). The impedance spectra of the batteries using 90NCM-10SE, 80NCM-20SE, and 70NCM-30SE are shown in Figure 5 (a)–(c). The resistance of the battery using 90NCM-10SE is smaller than those of the other batteries, indicating the possibility of achieving a higher capacity. The capacity retention rate is used as an indicator of cycling durability and is expressed as the discharge capacity measured during a certain cycle as a percentage of that measured during the first cycle. The capacity

Reprinted with permission from Journal of the Electrochemical Society

retention rate of the 90NCM-10SE all-solid-state battery was 91.7% at the 50th cycle. For the battery with a AG–$Li_{5.4}(PS_4)(S_{0.4}Cl_{1.0}Br_{0.6})$ | $Li_{5.4}(PS_4)(S_{0.4}Cl_{1.0}Br_{0.6})$ | $Li(Ni_{0.8}Co_{0.15}Al_{0.05})O_2$–$Li_{5.4}(PS_4)(S_{0.4}Cl_{1.0}Br_{0.6})$ structure used in our previous study,[18] the capacity retention rate and Coulombic efficiency were 96(4)% and 99.95(3)%, respectively, at the 50th cycle. The operating cut-off voltage was 4.2 V, which is lower than that of the Li | $Li_{5.4}(PS_4)(S_{0.4}Cl_{1.0}Br_{0.6})$ | $Li(Ni_{0.8}Co_{0.1}Mn_{0.1})O_2$–$Li_{5.4}(PS_4)(S_{0.4}Cl_{1.0}Br_{0.6})$ battery. The all-solid-state battery using $Li_{5.4}(PS_4)(S_{0.4}Cl_{1.0}Br_{0.6})$ as a solid electrolyte and $Li(Ni_{0.8}Co_{0.1}Mn_{0.1})O_2$ as a cathode active material showed the same capacity retention rate and Coulombic efficiency as those reported in our previous study,[18] despite the higher cut-off voltage. Because there is no significant difference in the Coulombic efficiencies and capacity retention rates among the different battery configurations, and the operating voltage of $Li(Ni_{0.8}Co_{0.1}Mn_{0.1})O_2$ is higher than that of $Li(Ni_{0.8}Co_{0.15}Al_{0.05})O_2$, it is concluded that the $Li_{5.4}(PS_4)(S_{0.4}Cl_{1.0}Br_{0.6})$ solid electrolyte has high electrochemical stability.

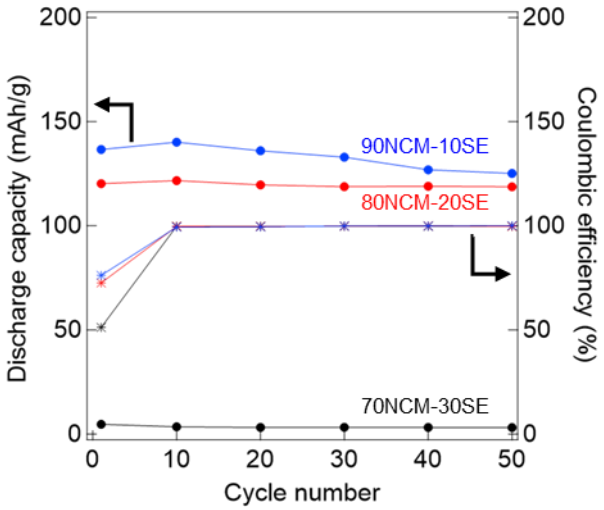

Figure 4. Cycling durability (filled circles) and Coulombic efficiency (asterisks) of the (black) 70NCM-30SE, (red) 80NCM-20SE, and (blue) 90NCM-10SE mixtures measured at 0.1C.

Reprinted with permission from Journal of the Electrochemical Society

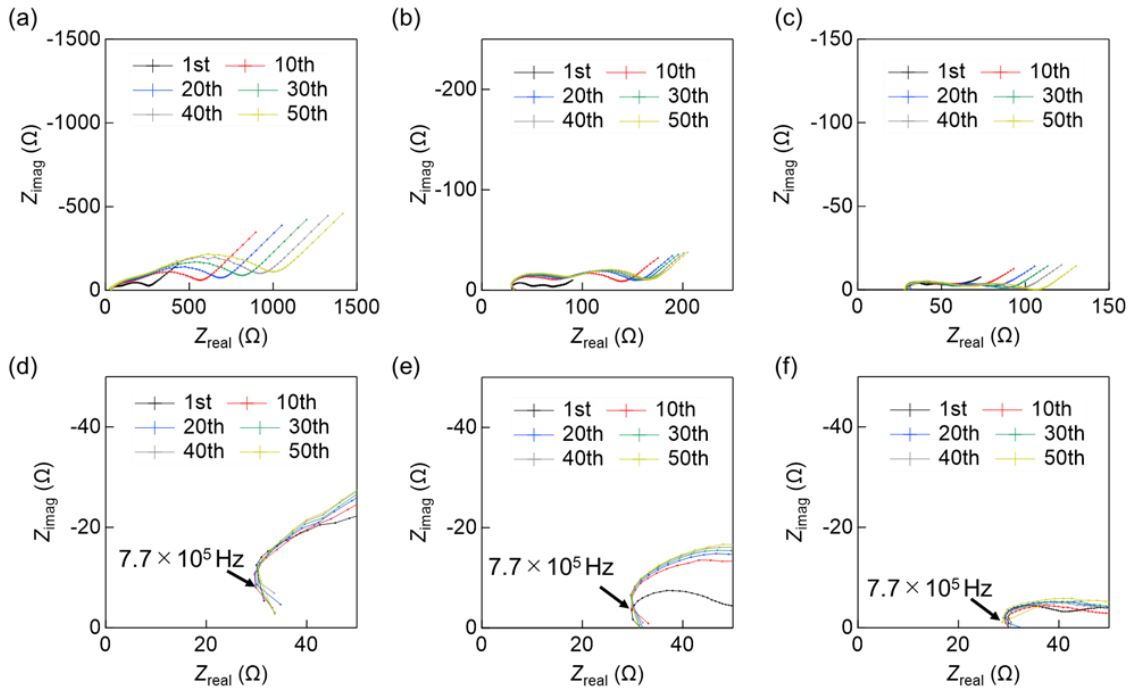

Figure 5. Impedance spectra of (a, d) 70NCM-30SE, (b, e) 80NCM-20SE, and (c, f) 90NCM-10SE mixtures measured at an equivalent of 50% SOC and a frequency range of 10^6–0.01 Hz over 50 cycles (data for the 1st, 10th, 20th, 30th, 40th, and 50th cycles are shown).

3.3.3 Properties of the $Li_{5.4}(PS_4)(S_{0.4}Cl_{1.0}Br_{0.6})$ and cathode mixtures after charge/discharge cycling of the all-solid-state batteries

For the batteries using 90NCM-10SE, 80NCM-20SE, and 70NCM-30SE, the resistances measured at approximately 10^6 Hz are similar (Figure 5 (a)–(f)) and the calculated resistances using equivalent circuit are also similar (Tables S1–S3). It is well-known that the high-frequency impedance corresponds to the resistance of the solid electrolyte including the bulk and grain boundary resistance of Li | $Li_{5.4}(PS_4)(S_{0.4}Cl_{1.0}Br_{0.6})$ | $Li(Ni_{0.8}Co_{0.1}Mn_{0.1})O_2$–$Li_{5.4}(PS_4)(S_{0.4}Cl_{1.0}Br_{0.6})$ batteries.[18,31,32] Therefore, the fact that the impedance values calculated from the equivalent circuit models of the batteries using 90NCM-10SE, 80NCM-20SE, and 70NCM-30SE tend to similar values above 10^6 Hz

Reprinted with permission from Journal of the Electrochemical Society

indicates that the electrolyte resistance is independent of the amount of $Li(Ni_{0.8}Co_{0.1}Mn_{0.1})O_2$ in the cathodes (Tables S1–S3).

It has previously been shown that the resistance of the $Li_{6.0}(PS_4)(S_{1.0}Cl_{1.0})$ solid electrolyte increased from 40 to 60 Ω after 50 cycles in InLi| $Li_{6.0}(PS_4)(S_{1.0}Cl_{1.0})$ | $LiCoO_2$–$Li_{6.0}(PS_4)(S_{1.0}Cl_{1.0})$ batteries.[32] Therein, the cut-off voltages at the high and low limits were 4.2 and 2.6 V, respectively, while for the Li | $Li_{5.4}(PS_4)(S_{0.4}Cl_{1.0}Br_{0.6})$ | $Li(Ni_{0.8}Co_{0.1}Mn_{0.1})O_2$–$Li_{5.4}(PS_4)(S_{0.4}Cl_{1.0}Br_{0.6})$ battery, the cut-off voltages were 4.3 and 2.5 V, respectively. A high operating voltage (up to 0.1 V) is desirable to increase the energy density of all-solid-state batteries.[20,21] Compared to $Li_{6.0}(PS_4)(S_{1.0}Cl_{1.0})$, $Li_{5.4}(PS_4)(S_{0.4}Cl_{1.0}Br_{0.6})$ has higher chemical stability over a wide voltage window, as indicated by the relatively constant resistance of the solid electrolyte over 50 charge/discharge cycles.

As shown in Figure 5 (a)–(c), the impedance spectra were reproduced by fitting with equivalent circuits (Figure 6 and Tables 1–3). Furthermore, as explained above, the resistance of the solid-electrolyte is relatively stable during cycling and independent of the amount of $Li(Ni_{0.8}Co_{0.1}Mn_{0.1})O_2$ in the electrode. The difference in the impedance spectra is attributed to the different ratios of the cathode components. This indicates that the spectral features below 10^6 Hz are related to the electrode impedance because the electrolyte resistance is independent of the amount of $Li(Ni_{0.8}Co_{0.1}Mn_{0.1})O_2$ in the cathodes.

Reprinted with permission from Journal of the Electrochemical Society

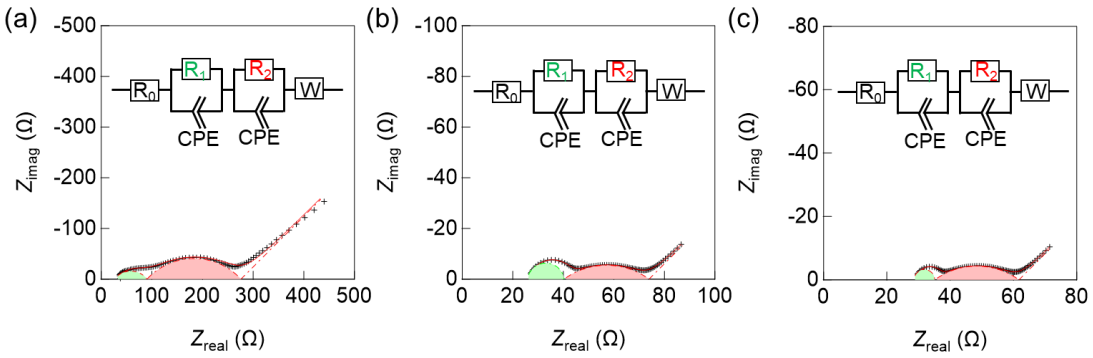

Figure 6. Impedance spectra of the batteries using (a) 70NCM-30SE, (b) 80NCM-20SE, and (c) 90NCM-10SE cathode materials measured at the 1st cycle and fitted using the inset equivalent circuit models, as previously reported.[S3] The spectra were fit using the Zmeam software.[S4]

Table 1. Equivalent circuit parameters obtained by fitting the impedance spectrum of the 70NCM-30SE battery.

70NCM-30SE	R0 (Ω)	R1 (Ω)	C1 (F $s^{(1-\alpha 1)}$)	α1	R2 (Ω)	C2 (F $s^{(1-\alpha 2)}$)	α2
1st cycle	25.12	76.55	2.13×10^{-5}	0.51	164.43	1.92×10^{-4}	0.58
10th cycle	25.21	212.30	4.29×10^{-5}	0.47	317.88	1.77×10^{-5}	0.67
20th cycle	25.16	263.31	4.39×10^{-5}	0.46	384.57	8.59×10^{-5}	0.70
30th cycle	25.15	292.23	4.10×10^{-5}	0.47	476.43	7.89×10^{-5}	0.69
40th cycle	25.16	326.91	4.10×10^{-5}	0.47	546.79	7.21×10^{-5}	0.70
50th cycle	25.17	343.92	4.03×10^{-5}	0.47	604.40	7.21×10^{-5}	0.70

Table 2. Equivalent circuit parameters obtained by fitting the impedance spectrum of the 80NCM-20SE battery.

80NCM-20SE	R0 (Ω)	R1 (Ω)	C1 (F $s^{(1-\alpha 1)}$)	α1	R2 (Ω)	C2 (F $s^{(1-\alpha 2)}$)	α2
1st cycle	25.20	16.21	1.05×10^{-5}	0.84	32.21	2.44×10^{-4}	0.40
10th cycle	25.18	56.62	1.77×10^{-5}	0.53	68.26	1.92×10^{-4}	0.54
20th cycle	25.16	56.86	1.24×10^{-5}	0.57	80.23	6.65×10^{-4}	0.52
30th cycle	25.21	62.25	1.43×10^{-5}	0.55	80.95	6.35×10^{-4}	0.52
40th cycle	25.10	73.72	2.25×10^{-5}	0.51	86.76	5.92×10^{-4}	0.56
50th cycle	25.05	77.71	2.45×10^{-5}	0.49	86.95	5.89×10^{-4}	0.57

Reprinted with permission from Journal of the Electrochemical Society

Table 3. Equivalent circuit parameters obtained by fitting the impedance spectrum of the 90NCM-10SE battery.

90NCM-10SE	R0 (Ω)	R1 (Ω)	C1 ($F\ s^{(1-\alpha 1)}$)	α1	R2 (Ω)	C2 ($F\ s^{(1-\alpha 2)}$)	α2
1st cycle	25.13	7.74	7.64×10^{-7}	0.92	25.22	2.62×10^{-4}	0.40
10th cycle	25.10	23.62	1.05×10^{-5}	0.87	25.79	3.38×10^{-4}	0.40
20th cycle	25.25	24.98	1.50×10^{-6}	0.84	39.42	1.81×10^{-4}	0.40
30th cycle	25.20	28.02	1.51×10^{-6}	0.83	45.02	1.51×10^{-4}	0.40
40th cycle	25.14	30.68	1.78×10^{-6}	0.79	50.99	1.09×10^{-4}	0.40
50th cycle	25.12	38.31	1.12×10^{-6}	0.81	59.79	1.11×10^{-4}	0.40

The electrode impedance of all samples increases during cycling (Figure 5 (a)–(c)). Our previously reported results on the stability of $Li_{5.4}(PS_4)(S_{0.4}Cl_{1.0}Br_{0.6})$ against lithium metal[18] demonstrated that this increase in impedance was mainly caused by the cathode. As shown by the XRD patterns in Figure 7 (a), no crystalline byproducts such as Li_2S, LiCl, or LiBr were formed in the cathode during 50 cycles, and all XRD peaks are attributed to $Li_{5.4}(PS_4)(S_{0.4}Cl_{1.0}Br_{0.6})$ and $Li_{1.0}(Ni_{0.8}Co_{0.1}Mn_{0.1})O_2$. Recently, it has been reported that amorphous byproducts at the interface of $Li_{6.0}(PS_4)(S_{1.0}Cl_{1.0})$ and $Li_{1.0}(Ni_{0.6}Co_{0.2}Mn_{0.2})O_2$ are generated during cycling, which can increase the impedance.[29,32] However, the reason for the increased impedance during cycling observed in our battery configuration was not clarified experimentally at this stage and will be the topic of future work. For example, amorphous byproducts may have been produced during cycling, which could not be identified by XRD. It has previously been shown that the cathode resistance of an all-solid-state InLi | $Li_{6.0}(PS_4)(S_{1.0}Cl_{1.0})$ | $LiCoO_2$–$Li_{6.0}(PS_4)(S_{1.0}Cl_{1.0})$ battery increased from 50 to 150 Ω after 50 cycles.[32] In comparison, the cathode resistance of 90NCM-10SE increased from 35 to 85 Ω after 50 cycles in a Li | $Li_{5.4}(PS_4)(S_{0.4}Cl_{1.0}Br_{0.6})$ | $Li(Ni_{0.8}Co_{0.1}Mn_{0.1})O_2$–$Li_{5.4}(PS_4)(S_{0.4}Cl_{1.0}Br_{0.6})$ battery

Reprinted with permission from Journal of the Electrochemical Society

configuration. After 50 cycles, the change in the cathode resistance of $Li_{5.4}(PS_4)(S_{0.4}Cl_{1.0}Br_{0.6})$ was smaller than that of $Li_{6.0}(PS_4)(S_{1.0}Cl_{1.0})$. In both the solid electrolyte and cathode layers, $Li_{5.4}(PS_4)(S_{0.4}Cl_{1.0}Br_{0.6})$ was more stable than $Li_{6.0}(PS_4)(S_{1.0}Cl_{1.0})$. Therefore, the high electrochemical stability of $Li_{5.4}(PS_4)(S_{0.4}Cl_{1.0}Br_{0.6})$ indicates that it has high potential for use in all-solid-state lithium-ion batteries.

A comparison of the XRD peaks of $Li(Ni_{0.8}Co_{0.1}Mn_{0.1})O_2$ before and after 50 cycles (Figure 7 (a)) revealed anisotropic volume changes, such as an expansion of the *c* axis and shrinkage of the *a* axis, in the pattern of the 90NCM-10SE cathode mixture.[30] The results of whole-pattern fitting using Rietan-FP[26] to compare the XRD patterns of $Li(Ni_{0.8}Co_{0.1}Mn_{0.1})O_2$ obtained before and after 50 cycles showed that the *c* axis expanded from 14.20(2) to 14.46(1) Å and the *a* axis shrank from 2.873(2) to 2.820(1) Å. The discharge capacity of 70NCM-30SE was lower than those of 80NCM-20SE and 90NCM-10SE (Figure 4). Even after 50 cycles, the lattice parameters of $Li(Ni_{0.8}Co_{0.1}Mn_{0.1})O_2$ in 70NCM-30SE, calculated from its main XRD peaks, did not change. After 50 cycles, the XRD pattern of 70NCM-30SE shows small peaks close to one of the $Li(Ni_{0.8}Co_{0.1}Mn_{0.1})O_2$ peaks (2θ = 18.5°) observed in 80NCM-20SE and 90NCM-10SE as the main XRD peak (Figure 7 (c)).[30] This indicates that in 70NCM-30SE, the lithiation and delithiation reactions occurred only in some of the $Li(Ni_{0.8}Co_{0.1}Mn_{0.1})O_2$, which is consistent with the low discharge capacity of this cathode mixture (Figure 4).

Reprinted with permission from Journal of the Electrochemical Society

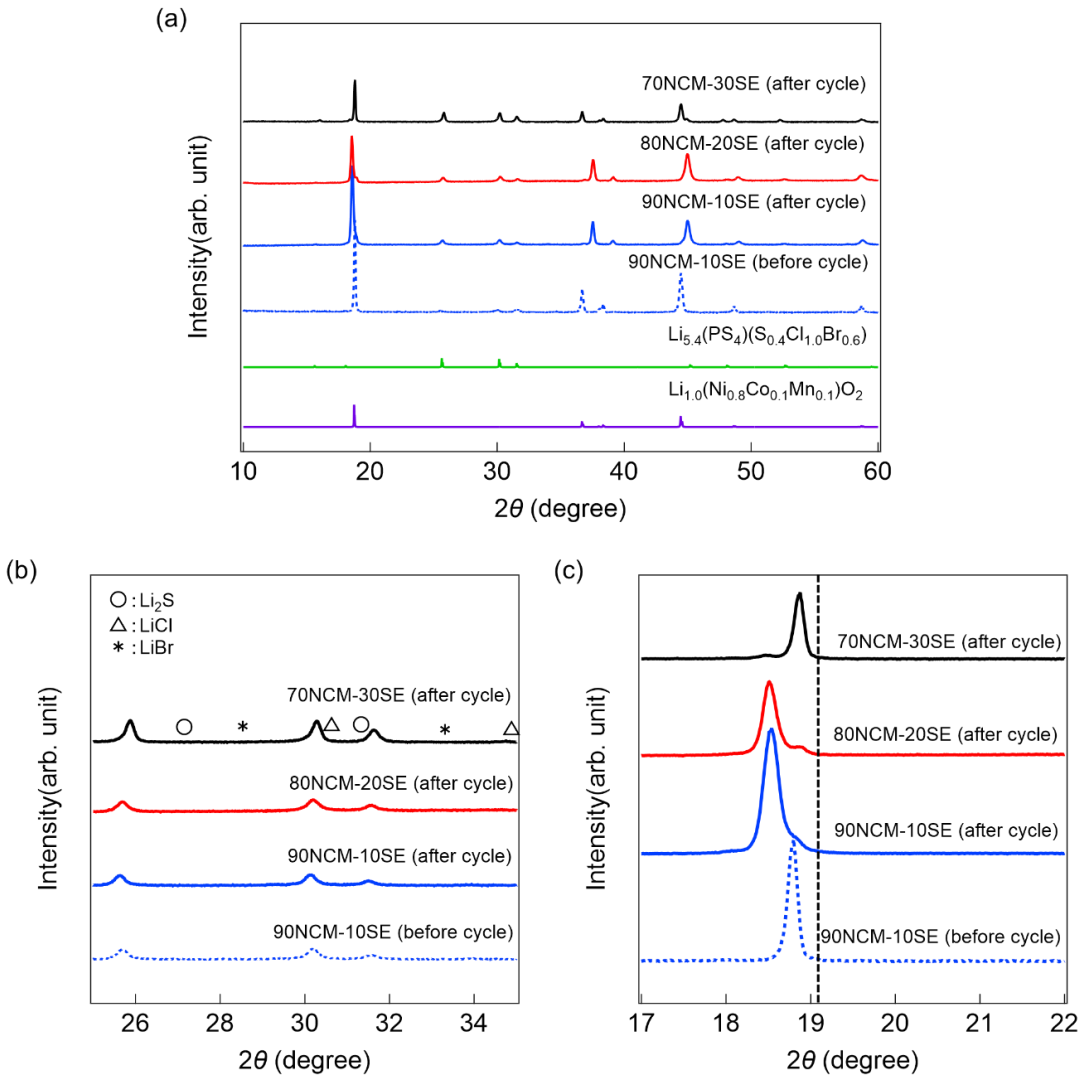

Figure 7. (a) XRD patterns of pellets of the 70NCM-30SE, 80NCM-20SE, and 90NCM-10SE cathode mixtures measured at room temperature (290–300 K) before and after cycling. The XRD pattern of $Li(Ni_{0.8}Co_{0.1}Mn_{0.1})O_2$ was simulated from reference data,[30] and that of $Li_{5.4}(PS_4)(S_{0.4}Cl_{1.0}Br_{0.6})$ before cycling is shown for reference (green line). (b) Magnified view of the evidence of no-formation of impurity crystalline phase. (c) Magnified view of the (003) XRD peak of $Li(Ni_{0.8}Co_{0.1}Mn_{0.1})O_2$ measured for the cathode mixture pellets before and after cycling. The black dashed line represents the position of the $2\theta = 18.5°$ peak.

Reprinted with permission from Journal of the Electrochemical Society

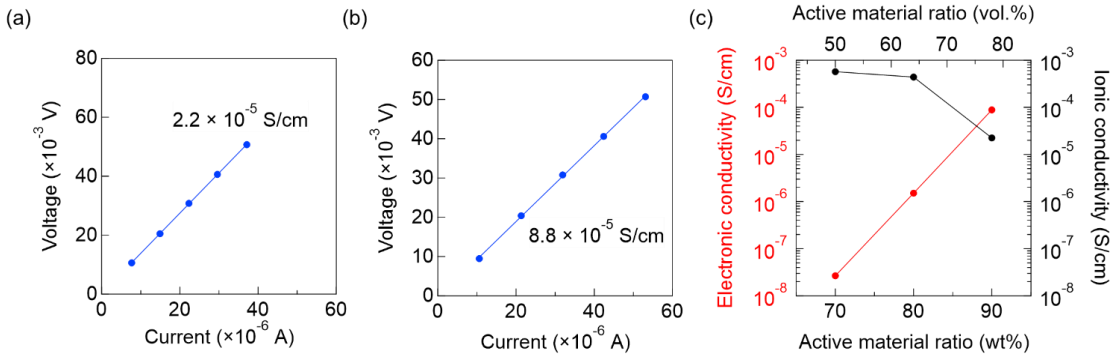

Figure 8. (a) Ionic conductivity and (b) electronic conductivity measurements for 90NCM-10SE. (c) Partial ionic and electronic conductivities of the cathode mixture.

No evidence of the formation of crystalline byproducts was found for any of the cathode mixtures after 50 cycles because of the high stability of $Li_{5.4}(PS_4)(S_{0.4}Cl_{1.0}Br_{0.6})$. Furthermore, in our experiments, amorphous PO fragments may have increased the resistivity during cycling,[29] resulting in decreased discharge capacity. We plan to investigate the existence of amorphous impurities as part of a future study. The decrease in discharge capacity with a decrease in the amount of $Li(Ni_{0.8}Co_{0.1}Mn_{0.1})O_2$ in the cathode mixtures is explained as follows. The partial ionic and electronic conductivities of 90NCM-10SE, 80NCM-20SE, and 70NCM-30SE were measured (Figure 8). The ionic conductivity increased with a decreasing amount of $Li(Ni_{0.8}Co_{0.1}Mn_{0.1})O_2$ in the cathode mixtures. In contrast, the electronic conductivity exhibited a trend opposite to that of the ionic conductivity. As the amount of $Li(Ni_{0.8}Co_{0.1}Mn_{0.1})O_2$ in the cathode mixtures increased, the electronic conductivity of the cathode mixtures increased, increasing the discharge capacity.[33] For 70NCM-30SE in particular, a low electronic conductivity reduced the discharge capacity (Figures 4 and 9). Among the 90NCM-10SE, 80NCM-20SE, and 70NCM-30SE cathode mixtures, the extent of the change in the electronic conductivity of the cathode is higher than that of the ionic conductivity. In the case of the

Reprinted with permission from Journal of the Electrochemical Society

addition of vapor grown carbon fiber (VGCF) as a carbon additive in the $Li(Ni_{0.6}Co_{0.2}Mn_{0.2})O_2$ and β-Li_3PS_4 cathode mixture, the discharge capacity of the battery with VGCF was 1.4 times higher than that of the battery without VGCF. [33] This report showed that a higher electronic conductivity of the cathode mixture results in a higher discharge capacity. This is consistent with our results (Figures 4 and 9).

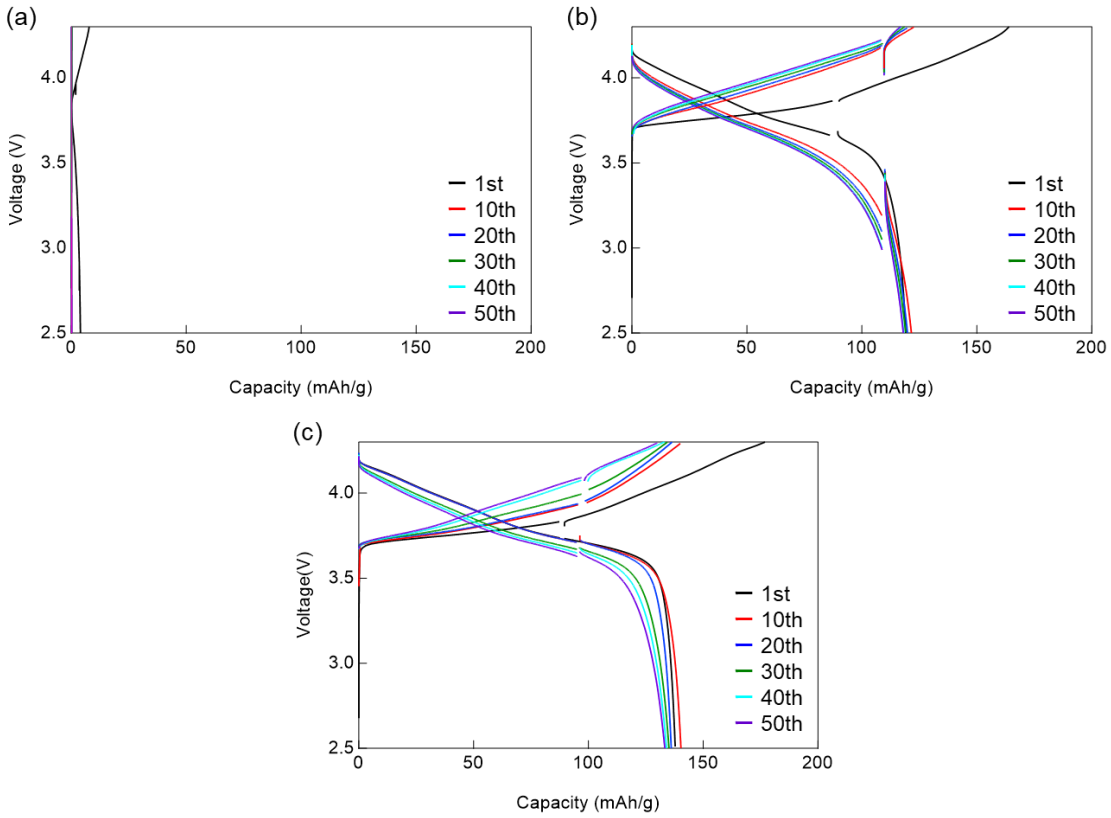

Figure 9. Charge/discharge curves of (a) 70NCM-30SE, (b) 80NCM-20SE, and (c) 90NCM-10SE. These charge/discharge curves are not continuous because impedance spectra were collected at the 1st, 10th, 20th, 30th, 40th, and 50th cycles under a state of charge (SOC) of 0%, 50%, and 100%.

Note that a significant number of voids were present in the solid electrolyte (Figure 10), reducing lithium permeability because of a reduction in the ionic conductivity with increasing porosity.[34] Furthermore, lithiation and delithiation reactions occur at the solid

Reprinted with permission from Journal of the Electrochemical Society

electrolyte/active material interfaces inside the cathode and at the solid electrolyte/cathode interface. Voids at the solid electrolyte/cathode active material interface limit the lithiation and delithiation reactions because lithium cannot diffuse through the voids. Therefore, a manufacturing process to prevent void formation inside the $Li(Ni_{0.8}Co_{0.1}Mn_{0.1})O_2$–$Li_{5.4}(PS_4)(S_{0.4}Cl_{1.0}Br_{0.6})$ cathode layer must be developed to improve the electrode performance.

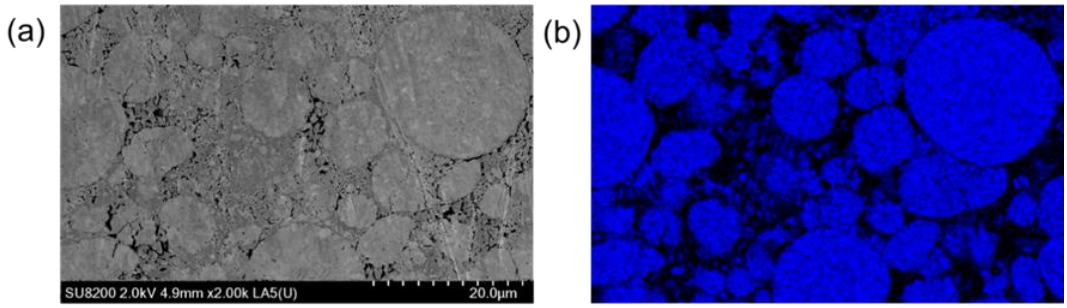

Figure 10. (a) SEM image and (b) the corresponding elemental map of Ni (blue) in the 90NCM-10SE mixture used to detect the presence of $Li(Ni_{0.8}Co_{0.1}Mn_{0.1})O_2$. In the SEM image, the bright areas correspond to the cathode active material, the dark gray areas to the solid electrolyte, and the black areas to voids.

No carbon additive was introduced in this study focusing on the stability of $Li_{5.4}(PS_4)(S_{0.4}Cl_{1.0}Br_{0.6})$ and $Li(Ni_{0.8}Co_{0.1}Mn_{0.1})O_2$ because exploration of the interface reaction between $LiNbO_3$-coated $Li(Ni_{0.8}Co_{0.1}Mn_{0.1})O_2$ and carbon or $Li_{5.4}(PS_4)(S_{0.4}Cl_{1.0}Br_{0.6})$ and carbon was beyond the scope of this study. However the addition of a carbon additive is an efficient approach to further improve cathode performance, especially for $Li(Ni_{1-x-y}Co_xMn_y)O_2$ because the electronic conductivity of $Li(Ni_{1-x-y}Co_xMn_y)O_2$ is < 0.01 mS/cm.[35]. For example, the addition of a carbon additive (3 wt%) to $Li(Ni_{0.6}Co_{0.2}Mn_{0.2})O_2$ and Li_3PS_4 (70:30 wt%) resulted in an increase in the discharge capacity from 100 to 145 mAh/g.[33] This indicates that the electronic

Reprinted with permission from Journal of the Electrochemical Society

conductivity of $Li(Ni_{0.6}Co_{0.2}Mn_{0.2})O_2$ is low. The electronic conductivity of $Li(Ni_{0.8}Co_{0.1}Mn_{0.1})O_2$ is also <0.01 mS/cm.[35] However, the ionic conductivity of $Li_{5.4}(PS_4)(S_{0.4}Cl_{1.0}Br_{0.6})$ (12 mS/cm) is 100 times higher than the electronic conductivity of $Li(Ni_{0.8}Co_{0.1}Mn_{0.1})O_2$. Insufficient electronic conductivity results in a low discharge capacity.[33] To improve cathode performance, the addition of carbon additive materials with high electronic conductivity has proven to be highly effective.

3.4 Conclusions

The electrochemical stability of a new solid electrolyte, $Li_{5.4}(PS_4)(S_{0.4}Cl_{1.0}Br_{0.6})$, mixed with the $Li(Ni_{0.8}Co_{0.1}Mn_{0.1})O_2$ cathode active material was evaluated for an all-solid-state battery with a Li | $Li_{5.4}(PS_4)(S_{0.4}Cl_{1.0}Br_{0.6})$ | $Li(Ni_{0.8}Co_{0.1}Mn_{0.1})O_2$–$Li_{5.4}(PS_4)(S_{0.4}Cl_{1.0}Br_{0.6})$ structure. At a high frequency of ~10^6 Hz, the resistance of the solid electrolyte remained unchanged during 50 charge/discharge cycles. No evidence of the formation of crystalline byproducts was observed in the XRD patterns of any cathode mixtures from the all-solid-state batteries after 50 cycles. These results demonstrate the superior stability of $Li_{5.4}(PS_4)(S_{0.4}Cl_{1.0}Br_{0.6})$ against $Li(Ni_{0.8}Co_{0.1}Mn_{0.1})O_2$ for all tested cathode compositions. The all-solid-state battery performance of Li | $Li_{5.4}(PS_4)(S_{0.4}Cl_{1.0}Br_{0.6})$ | $Li(Ni_{0.8}Co_{0.1}Mn_{0.1})O_2$–$Li_{5.4}(PS_4)(S_{0.4}Cl_{1.0}Br_{0.6})$ can be further improved by reducing the porosity of the $Li_{5.4}(PS_4)(S_{0.4}Cl_{1.0}Br_{0.6})$ material in the mixed cathode layer and by adding a carbon additive to enhance the discharge capacity.

3.5 References

1. M. Z. Jacobson, *Energy Environ. Sci.*, **2**, 148 (2009). https://doi.org/10.1039/B809990C

Reprinted with permission from Journal of the Electrochemical Society

2. M. A. Hannan, M. S. H. Lipu, A. Hussain, and A. Mohamed, *Renew. Sustain. Energy Rev.*, **78**, 834-854 (2017). https://doi.org/10.1016/j.rser.2017.05.001

3. J. Janek and W. G. Zeier, *Nat. Energy*, **1**, 16141 (2016). https://doi.org/10.1038/nenergy.2016.141

4. Y. Kato, S. Hori, T. Saito, K. Suzuki, M. Hirayama, A. Mitsui, M. Yonemura, H. Iba, and R. Kanno, *Nat. Energy*, **1**, 16030 (2016). https://doi.org/10.1038/nenergy.2016.30

5. S. Boulineau, J. M. Tarascon, J. B. Leriche, and V. Viallet, *Solid State Ionics*, **242**, 45 (2013). https://doi.org/10.1016/j.ssi.2013.04.012

6. P. Wang, H. Liu, S. Patel, X. Feng, P.-H. Chien, Y. Wang, and Y. Y. Hu, *Chem. Mater.*, **32**, 3833-3840 (2020). https://doi.org/10.1021/acs.chemmater.9b05331

7. X. Feng, P. -H. Chien, Y. Wang, S. Petel, P. Wang, H. Liu, M. Immediato-Scuotto, and Y. Y. Hu, *Energy. Stor. Mater.*, **30**, 67 (2020). https://doi.org/10.1016/j.ensm.2020.04.042

8. P. Adeli, J. D. Bazak, K. H. Park, I. Kochetkov, A. Huq, G. R. Goward, and L. F. Nazar, *Angew. Chem. Int. Ed.*, **58**, 8681 (2019). https://doi.org/10.1002/anie.201814222

9. P. Adeli, J. D. Bazak, A. Huq, G. R. Goward, and L. F. Nazar, *Chem. Mater.*, **33**, 146 (2021). https://doi.org/10.1021/acs.chemmater.0c03090

10. M. Suyama, A. Kato, A. Sakuda, A. Hayashi, and M. Tatsumisago, *Electrochim*. *Acta*, **286**, 158 (2018). https://doi.org/10.1016/j.electacta.2018.07.227

11. V. Epp, O. Gün, H. J. Deiseroth, and M. Wilkening, *J. Phys. Chem. Lett.*, **4**, 2118 (2013). https://doi.org/10.1021/jz401003a

12. A. Gautam, M. Sadowski, M. Ghidiu, N. Minafra, A. Senyshyn, K. Albe, and W. G. Zeier, *Adv. Energy Mater.*, **11**, 2003369 (2020). https://doi.org/10.1002/aenm.202003369

13. S. V. Patel, S. Banerjee, H. Liu, P. Wang, P. H. Chien, X. Feng, J. Liu, S. P. Ong, and Y. Y. Hu, *Chem. Mater.*, **33**, 1435 (2021). https://doi.org/10.1021/acs.chemmater.0c04650

Reprinted with permission from Journal of the Electrochemical Society

14. N. J. J. De Klerk, I. Rosłoń, and M. Wagemaker, *Chem. Mater.*, **28**, 7955 (2016). https://doi.org/10.1021/acs.chemmater.6b03630

15. M. A. Kraft, S. P. Culver, M. Calderon, F. Böcher, T. Krauskopf, A. Senyshyn, C. Dietrich, A. Zevalkink, J. Janek, and W. G. Zeier, *J. Am. Chem. Soc.*, **139**, 10909 (2017). https://doi.org/10.1021/jacs.7b06327

16. C. Yu, Y. Li, W. Li, K. R. Adair, F. Zhao, M. Willans, J. Liang, Y. Zhao, C. Wang, S. Deng, R. Li, H. Huang, S. Lu, T. K. Sham, Y. Huang, and X. Sun, *Energy Stor. Mater.*, **30**, 238 (2020). https://doi.org/10.1016/j.ensm.2020.04.014

17. Y. Subramanian, R. Rajagopal, and K. S. Ryu, *J. Power Sources*, **520**, 230849 (2022). https://doi.org/10.1016/j.jpowsour.2021.230849

18. N. Masuda, K. Kobayashi, F. Utsuno, T. Uchikoshi, and N. Kuwata, *J. Phys. Chem. C*, **126**, 14067-14074 (2022). https://doi.org/10.1021/acs.jpcc.2c03780

19. Y. Seino, N. Ohta, and K. Takada, *J. Power Sources*, **196**, 6488 (2011). https://doi.org/10.1016/j.jpowsour.2011.03.090

20. W. Li, E. M. Erickson, and A. Manthiram, *Nat. Energy*, **5**, 26 (2020). https://doi.org/10.1038/s41560-019-0513-0

21. T. Weigel, F. Schipper, E. M. Erickson, F. A. Susai, B. Markoovsky, and D. Aurbach, *ACS Energy Lett.*, **2**, 508 (2019). https://doi.org/10.1021/acsenergylett.8b02302

22. X. Yao, D. Liu, C. Wang, R. Long, G. Peng, Y. S. Hu, H. Li, L. Chen, and X. Xu, *Nano Lett.*, **11**, 7148 (2016). https://doi.org/10.1021/acs.nanolett.6b03448

23. N. Ohta, K. Takada, I. Sakaguchi, L. Zhang, R. Ma, K. Fukuda, M. Osada, and T. Sasaki, *Electrochem. Commun.*, **9**, 1786 (2007). https://doi.org/10.1016/j.elecom.2007.02.008

24. X. Zheng, X. Li, B. Zhang, Z. Wang, H. Guo, Z. Huang, G. Yan, D. Wang, and Y. Xu,

Reprinted with permission from Journal of the Electrochemical Society

Ceram. Int., **42**, 644 (2016). https://doi.org/10.1016/j.ceramint.2015.08.159

25. L. Alexander and H. P. Klug, *Anal. Chem.*, **20**, 886 (1948). https://doi.org/10.1021/ac60022a002

26. F. Izumi and K. Momma, *Solid State Phenom.*, **130**, 15 (2007). https://doi.org/10.4028/www.scientific.net/SSP.130.15

27. M. Ahmadipour, M. J. Abu, M. Fariz, A. Rahman, M. F. Ain, and Z. A. Ahmad, *Micro & Nano Letters*, **11**, 47 (2016). https://doi.org/10.1049/mnl.2015.0562

28. S. Gao, B. Liu, B. Hu, Z. Ning, D. S. Jolly, S. Zhang, J. Perera, J. Bu, J. Liu, C. Doerrer, E. Darnbrough, D. Armstrong, P. S. Grant, and P. G. Bruce, *Joule*, **6**, 636 (2022). https://doi.org/10.1016/j.joule.2022.02.008

29. F. Walther, R. Koerver, T. Fuchs, S. Ohno, J. Sann, M. Rohnke, W. G. Zeier, and J. Janek, *Chem. Mater.*, **31**, 3745 (2019). https://doi.org/10.1021/acs.chemmater.9b00770

30. K. Märker, P. J. Reeves, C. Xu, K. J. Griffith, and C. P. Grey, *Chem. Mater.*, **31**, 2545 (2019). https://doi.org/ 10.1021/acs.chemmater.9b00140

31. R. Koerver, I. Aygün, T. Leichtweiß, C. Dietrich, W. Zhang, J. O. Binder, P. Hartmann, W. G. Zeier, and J. Janek, *Chem. Mater.*, **29**, 5574 (2017). https://doi.org/10.1021/acs.chemmater.7b00931

32. S. Wang, W. Zhang, X. Chen, D. Das, R. Ruess, A. Gautam, F. Walter, S. Ohno, R. Koerver, Q. Zhang, W. G. Zeier, F. H. Richter, C. W. Nan, and J. Janek, *Adv. Energy Mater.*, **11**, 2100654 (2021). https://doi.org/10.1002/aenm.202100654

33. F. Walther, S. Randau, Y. Schneider, J. Sann, M. Rohnke, F. H. Richter, W. G. Zeier, and J. Janex, *Chem. Mater.*, **14**, 6123 (2020). https://doi.org/10.1021/acs.chemmater.0c01825

34. A. Sakuda, A. Hayashi, T. Ohmoto, S. Hama, and M. Tatsumisago, *J. Power Sources*,

Reprinted with permission from Journal of the Electrochemical Society

196, 6735 (2011). https://10.1016/j.jpowsour.2010.10.103

35. J. Zahnow, T. Bernges, A. Wagner, N. Bohn, J. R. Binder, W. G. Zeier, M. T. Elm, and J. Janek, *ACS Appl. Energy Mater.*, **2**, 1335 (2021). https://doi.org/10.1021/acsaem.0c02606

Reprinted with permission from Journal of the Electrochemical Society

4. Enhanced Capacity of All-Solid-State Battery Comprising $LiNbO_3$-Coated $Li(Ni_{0.8}Co_{0.1}Mn_{0.1})O_2$ Cathode, $Li_{5.4}(PS_4)(S_{0.4}Cl_{1.0}Br_{0.6})$ Solid Electrolyte and Lithium Metal Anode

4.1 Introduction

Various high-performance lithium-ion rechargeable batteries, such as all-solid-state batteries, have been developed to address the demand for technological development under the challenges of climate change [1] and realize a sustainable carbon-neutral society [2-4]. The performance of all-solid-state batteries mostly depends on the electrochemical properties and lithium-ion conductivity of the electrolyte [5]. Although conventional all-solid-state lithium-ion batteries have low rate capabilities and energy densities, recent studies have demonstrated that lithium–phosphorus–sulfide solid electrolytes (SE) show improved ionic conductivity [6-8] and may be easily integrated into battery production because of their mechanical softness [9] and facile processing [10].

Among the phosphorus sulfides, we have discovered various $Li_{7-\alpha}PS_{6-\alpha}X_\alpha$ (X = Cl, Br, I) argyrodites that exhibit high ionic conductivities [11-17], denoted as $Li_{7-\alpha}(PS_4)(S_{2-\alpha}X_\alpha)$ [18]. In a $Li_{7-x-y}(PS_4)(S_{2-x-y}Cl_xBr_y)$ system [18], $Li_{5.4}(PS_4)(S_{0.4}Cl_{1.0}Br_{0.6})$ showed excellent electrochemical stability in Li｜$Li_{5.4}(PS_4)(S_{0.4}Cl_{1.0}Br_{0.6})$｜$Li(Ni_{0.8}Co_{0.1}Mn_{0.1})O_2$–$Li_{5.4}(PS_4)(S_{0.4}Cl_{1.0}Br_{0.6})$ batteries. Nevertheless, the discharge capacity of this battery (140 mAh/g) was still lower than those of other all-solid-state batteries (> 140 mAh/g) [19].

Reprinted with permission from Journal of Solid State Electrochemistry

To explain the low discharge capacity, we measured the electronic and ionic conductivities of cathode mixtures. Changing the amount of cathode active material from 70 to 90 wt% increased the electronic conductivity of the cathode mixture, but reduced its ionic conductivity. Unfortunately, both high electronic and lithium-ion conductivities are necessary for generating an effective composite cathode. In addition, much predomination of electronic conductivity contributes to the discharge capacity [19].

Several studies have attempted to enhance the capacity of various sulfide solid electrolytes using a carbon additive (CA) to increase the electronic conductivity of the cathode [20-42]. The discharge capacity of the Li｜β-Li_3PS_4 | $Li(Ni_{0.6}Co_{0.2}Mn_{0.2})O_2$–β-$Li_3PS_4$ battery increased with a CA-modified cathode. However, the capacity retention rate was ~85% after 50 cycles [23]. Similarly, the retention rate of the In-Li｜$Li_{6.0}(PS_4)(S_{1.0}Cl_{1.0})$ | $Li(Ni_{0.6}Co_{0.2}Mn_{0.2})O_2$–$Li_{6.0}(PS_4)(S_{1.0}Cl_{1.0})$ battery was 79% after 50 cycles [42]. With a CA, the capacity decreased with repeated cycles, although the initial capacity was high [23]. The decreased capacity after cycling was likely related to a decomposition reaction of SE, although the mechanism remains unclear [43, 44]. However, it is unclear whether an all-solid-state battery with a CA-modified cathode can maintain a consistent capacity after cycling.

We hypothesized that a CA-modified cathode would enhance the capacity of an all-solid-state battery using a high ion-conductive $Li_{5.4}(PS_4)(S_{0.4}Cl_{1.0}Br_{0.6})$ solid electrolyte. We previously showed that batteries with a cathode mixture consisting of 70 wt% active material and 30 wt% $Li_{5.4}(PS_4)(S_{0.4}Cl_{1.0}Br_{0.6})$ had the lowest capacity [19]; however, the capacity of the battery may be rescued by adding CA to increase the electronic

Reprinted with permission from Journal of Solid State Electrochemistry

conductivity of the cathode mixture [19]. Unfortunately, the effects of CA cathode modifications in all-solid-state $Li_{5.4}(PS_4)(S_{0.4}Cl_{1.0}Br_{0.6})$ batteries are unclear. To increase the battery capacity, the cathode mixture should preferably have a high active material ratio. However, we selected 70 wt% active material and 30 wt% $Li_{5.4}(PS_4)(S_{0.4}Cl_{1.0}Br_{0.6})$ to investigate the effect of electronic conductivity on capacity during cycling. We measured the changes in the discharge capacity and capacity retention rates of the Li｜$Li_{5.4}(PS_4)(S_{0.4}Cl_{1.0}Br_{0.6})$ | $Li(Ni_{0.8}Co_{0.1}Mn_{0.1})O_2$–$Li_{5.4}(PS_4)(S_{0.4}Cl_{1.0}Br_{0.6})$–CA battery using cycling tests, followed by impedance analysis to evaluate the battery resistance during cycling.

4.2 Experimental

4.2.1 Synthesis of solid electrolyte and cathode mixture

$Li_{5.4}(PS_4)(S_{0.4}Cl_{0.1}Br_{0.6})$ powder and $LiNbO_3$-coated $Li(Ni_{0.8}Co_{0.1}Mn_{0.1})O_2$ were synthesized as we previously described [18, 19]. Mixed cathode powders were prepared using $LiNbO_3$-coated $Li(Ni_{0.8}Co_{0.1}Mn_{0.1})O_2$, $Li_{5.4}(PS_4)(S_{0.4}Cl_{1.0}Br_{0.6})$, and CA (Li100, Denka) in weight ratios of 70:30:0 (0 vol%), 70:30:3.4 (5 vol%), 70:30:7.2 (10 vol%), and 70:30:21.5 (25 vol%), respectively. CA made from acetylene black was selected in this study because it has previously been reported to maintain a high-capacity retention rate even after cycling [20]. The densities for $Li(Ni_{0.8}Co_{0.1}Mn_{0.1})O_2$ and $Li_{5.4}(PS_4)(S_{0.4}Cl_{1.0}Br_{0.6})$ were selected as previously described [19] and the CA load was 2.16 g/cm^3 [45]. The cathode mixtures were placed in a ZrO_2 pot (45 ml) containing a ZrO_2 ball (2.0 mm diameter; 34 g) in an argon-filled glovebox for dry ball-milling. The mixing condition was the same as in our previous study [19].

Reprinted with permission from Journal of Solid State Electrochemistry

4.2.2 All-solid-state battery fabrication and electrochemical measurements

We fabricated a battery with a Li｜$Li_{5.4}(PS_4)(S_{0.4}Cl_{1.0}Br_{0.6})$ | $Li(Ni_{0.8}Co_{0.1}Mn_{0.1})O_2$–$Li_{5.4}(PS_4)(S_{0.4}Cl_{1.0}Br_{0.6})$–CA structure. The total amount of cathode active material was 18 mg. Lithium foil (10 mm diameter, 0.2 mm thickness; Honjo Metal, Osaka, Japan) was used as the anode. The solid electrolyte (100 mg) was pressed into 10-mm-diameter pellets at 300 MPa. The cathode mixtures were pressed into 10-mm-diameter pellets at 600 MPa to form a cathode electrode layer. Finally, lithium metal was attached to the opposite side of the cathode and pressed at 100 MPa.

Electrochemical measurements were performed while the battery pellets were loaded at 20 MPa using a screw and torque wrench. The battery was charged and discharged between 2.5 and 4.3 V at 298 K using a potentio-galvanostat (VMP-3, Biologic, Seyssinet-Pariset, France). The atmosphere contained less than 1 ppm moisture and oxygen. The current density was fixed at 0.24 or 1.2 mA/cm^2, corresponding to 0.1 C and 0.5 C, respectively. Impedance spectra were collected using the potentio-galvanostat. The charge and discharge capacity values at the 1st, 2nd, 10th, 20th, 30th, 40th, and 50th cycles were measured at 0.1 C. The values at all other cycles were measured at 0.5 C to accelerate the capacity degradation. Impedance spectra were collected at the 1st, 10th, 20th, 30th, 40th, and 50th cycles under a state of charge (SOC) of 0%, 50%, and 100%. Before conducting the impedance measurements, the charge and discharge operations were stopped for 5 min. Impedance spectra were measured for the open-cell state with a voltage amplitude of 10 mV over a frequency range of 10^6 to 0.01 Hz at 298 K. All measurements were conducted under 1 ppm of moisture and oxygen. For an all-solid-state battery comprising a sulfide solid electrolyte, 300 to 600 MPa can be applied to manufacture the pellet and 10 to 70 MPa during cycling [18, 19, 46-48]. Impedance

Reprinted with permission from Journal of Solid State Electrochemistry

spectra were fitted using Zmeam software (Zmeam_v109002) [49].

4.2.3 Partial ionic and electronic conductivity measurements of cathode mixtures

The ionic and electronic conductivities of the cathode mixtures were measured as previously described [19]. The ionic conductivities of the cathode mixtures were measured using an electron-blocking cell with a Li | $Li_{5.4}(PS_4)(S_{0.4}Cl_{1.0}Br_{0.6})$ | $Li(Ni_{0.8}Co_{0.1}Mn_{0.1})O_2$–$Li_{5.4}(PS_4)(S_{0.4}Cl_{1.0}Br_{0.6})$–CA | $Li_{5.4}(PS_4)(S_{0.4}Cl_{1.0}Br_{0.6})$ | Li structure. Cathode mixtures (total weight: 200 mg) sandwiched with 50 mg of $Li_{5.4}(PS_4)(S_{0.4}Cl_{1.0}Br_{0.6})$ from both sides were pressed into 10-mm-diameter pellets at 600 MPa. Subsequently, Li foil (10 mm φ, thickness: 0.2 mm; Honjo Metal) was applied on both ends and pressed at 100 MPa. Constant voltages (E_{app_i}) of 10, 20, 30, 40, and 50 mV were applied for 2 h. The resistance of the electron-blocking cell was calculated from the slope between E_{app_i} and current using the current and voltage values obtained after 2 h. The electron-blocking cell resistance includes the solid electrolyte and mixture resistances. The resistance of the solid electrolyte and cell length of $Li_{5.4}(PS_4)(S_{0.4}Cl_{1.0}Br_{0.6})$ (equivalent to 16.2 Ω and 7.4×10^{-2} cm at 100 mg, respectively) were calculated [18] and subtracted from the electron-blocking cell resistance. The ionic conductivity was calculated using the surface area (0.785 cm^2), subtracted resistance, and cell length. The measurements were performed while the electron-blocking cell was compressed at 20 MPa using a screw and torque wrench in an atmosphere with 1 ppm moisture and oxygen.

The electronic conductivity of the cathode composites was measured using an ion-blocking electrode of stainless steel (SUS) | $Li(Ni_{0.8}Co_{0.1}Mn_{0.1})O_2$–$Li_{5.4}(PS_4)(S_{0.4}Cl_{1.0}Br_{0.6})$–CA | SUS. The ion-blocking electrode (total weight: 200 mg)

Reprinted with permission from Journal of Solid State Electrochemistry

was pressed into 10-mm-diameter pellets under 600 MPa. Thereafter, constant voltages (E_{app_e}) of 10, 20, 30, 40, and 50 mV were applied to the electrode pellets for 2 h, and the resistance of the composite was calculated from the slope between E_{app_e} and current. This calculation does not require correction of the solid electrolyte resistance. The measurements were performed while the electrode pellets were compressed at 20 MPa using a screw and torque wrench in an atmosphere with 1 ppm moisture and oxygen.

4.3 Results and Discussion

4.3.1 Charge and discharge capacities of Li｜$Li_{5.4}(PS_4)(S_{0.4}Cl_{1.0}Br_{0.6})$｜$Li(Ni_{0.8}Co_{0.1}Mn_{0.1})O_2$–$Li_{5.4}(PS_4)(S_{0.4}Cl_{1.0}Br_{0.6})$-CA batteries

In our previous study, the battery using $LiNbO_3$-coated $Li(Ni_{0.8}Co_{0.1}Mn_{0.1})O_2$ and $Li_{5.4}(PS_4)(S_{0.4}Cl_{1.0}Br_{0.6})$ in weight ratios of 70:30 without CA exhibited the lowest discharge capacity among the batteries comprising different ratios of $Li(Ni_{0.8}Co_{0.1}Mn_{0.1})O_2$ and $Li_{5.4}(PS_4)(S_{0.4}Cl_{1.0}Br_{0.6})$ [19]. The discharge capacity and capacity retention rate of the battery using 70:30 $LiNbO_3$-coated $Li(Ni_{0.8}Co_{0.1}Mn_{0.1})O_2$ and $Li_{5.4}(PS_4)(S_{0.4}Cl_{1.0}Br_{0.6})$ after 50 cycles were 3.1 mAh/g and 99.1%, respectively. Compared with that when using 0 vol% CA in the cathode mixture [$LiNbO_3$-coated $Li(Ni_{0.8}Co_{0.1}Mn_{0.1})O_2$ and $Li_{5.4}(PS_4)(S_{0.4}Cl_{1.0}Br_{0.6})$ in weight ratios of 70:30], the discharge capacity increased from 3.1 to 167 mAh/g after 50 cycles when using 5 vol% (Figure. 1(a)). The capacity retention rate and coulombic efficiency after 50 charge/discharge cycles were 95.4% and 99.9% when using 0.1 C and 0.5 C, respectively. This represents a much higher capacity retention rate compared with that

Reprinted with permission from Journal of Solid State Electrochemistry

of the In-Li｜$Li_{6.0}(PS_4)(S_{1.0}Cl_{1.0})$ | $Li(Ni_{0.6}Co_{0.2}Mn_{0.2})O_2$– $Li_{6.0}(PS_4)(S_{1.0}Cl_{1.0})$ battery [42] after 50 cycles (79%). However, the discharge capacity decreased when the amount of CA exceeded 5 vol%. The discharge capacity of the battery using 25 vol% was 25 mAh/g at most in the initial cycle and the battery suddenly short-circuited after 6 cycles. The first explanation for this phenomenon is that decomposed products formed at the SE/CA interface, such as the decomposition of solid electrolyte observed by cyclic voltammogram in the Li | β-Li_3PS_4 | β-Li_3PS_4-CA configuration [43]. The bonding of terminal sulfur such as PS_4 tetrahedra in β-Li_3PS_4 was experimentally confirmed to be decomposed into bridged sulfur compounds (-S-) above 3.5 V [43, 44]. This indicated that PS_4 tetrahedra containing solid electrolyte decomposed at high voltage. In our previous study, $Li_{5.4}(PS_4)(S_{0.4}Cl_{1.0}Br_{0.6})$ was stable above 10 V without CA. This suggests that an increased probability of reaction between the CA and $Li_{5.4}(PS_4)(S_{0.4}Cl_{1.0}Br_{0.6})$ exists in batteries using the 25 vol% cathode. Notably, 10 vol% corresponded to a high discharge capacity, almost equivalent to that at 5 vol%. This suggests that $Li_{5.4}(PS_4)(S_{0.4}Cl_{1.0}Br_{0.6})$ is stable and its decomposition is negligible in the 10 vol% cathode. The second explanation is that decomposed products were formed at the $Li(Ni_{0.8}Co_{0.1}Mn_{0.1})O_2$/$Li_{5.4}(PS_4)(S_{0.4}Cl_{1.0}Br_{0.6})$ interface. We previously reported amorphous impurities generated at the $Li(Ni_{0.8}Co_{0.1}Mn_{0.1})O_2$/$Li_{5.4}(PS_4)(S_{0.4}Cl_{1.0}Br_{0.6})$ interface during cycling, which increased impedance. Because we used a similar composition of cathode active material and solid electrolyte, we presumed that amorphous impurities formed in systems with high CA contents [19]. A third explanation is that impurities were generated at the $Li(Ni_{0.8}Co_{0.1}Mn_{0.1})O_2$/CA interface, though this requires validation [23]. Consequently, we hypothesized that the short circuit in 25 vol% CA batteries was due to the decomposition reactions at the

Reprinted with permission from Journal of Solid State Electrochemistry

$Li_{5.4}(PS_4)(S_{0.4}Cl_{1.0}Br_{0.6})$/CA and $Li(Ni_{0.8}Co_{0.1}Mn_{0.1})O_2/Li_{5.4}(PS_4)(S_{0.4}Cl_{1.0}Br_{0.6})$ interfaces.

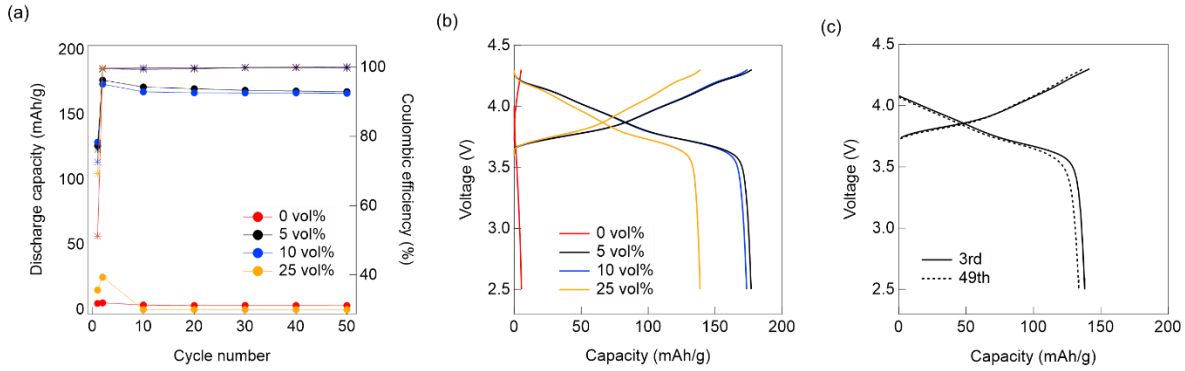

Figure. 1 (a) Cycling durability (filled circles) and coulombic efficiency (asterisks) of the all-solid-state battery using (red) 0 vol%, (black) 5 vol%, (blue) 10 vol%, and (orange) 25 vol% cathode mixtures measured at 0.1 C. (b) Charge/discharge curve of 2nd cycle at 0.1 C. The red, black, blue, and orange lines represent 0 vol%, 5 vol%, 10 vol%, and 25 vol%, respectively. (c) Capacity curve of all-solid-state battery using 5 vol% cathode at 3rd and 49th cycle charged/discharged at 0.5 C

We previously measured the electronic and ionic conductivities of cathode mixtures without CA and found that changing the cathode active material content from 70 to 90 wt% promoted electronic conductivity while reducing ionic conductivity. Because electronic conductivity changed more drastically than ionic conductivity, it is likely that electronic conductivity was the key factor affecting discharge capacity [19]. We adjusted the amount of CA (from 0 to 25 vol%) in the battery comprising 70:30 $LiNbO_3$-coated $Li(Ni_{0.8}Co_{0.1}Mn_{0.1})O_2$ and $Li_{5.4}(PS_4)(S_{0.4}Cl_{1.0}Br_{0.6})$ and found that the electronic conductivities of the cathode mixtures increased greatly from 2.6×10^{-8} to 1.1 S/cm with a CA modification (Figure. 2).

Reprinted with permission from Journal of Solid State Electrochemistry

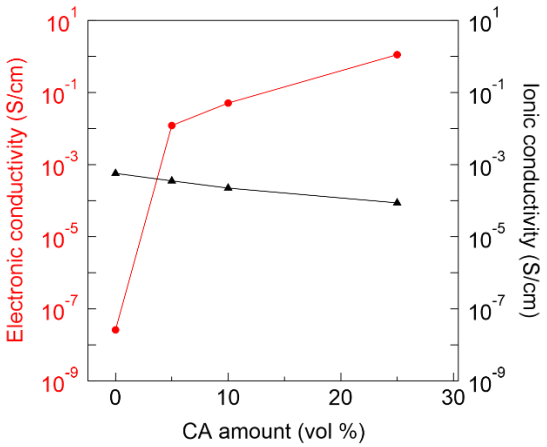

Figure. 2 Partial ionic and electronic conductivities of the cathode mixture with increasing amounts of CA

The lithium-ion conductivity between 0 and 25 vol% was about 2.9×10^8 times smaller than the electronic conductivity. The small degree of change in ionic conductivity was likely due to the weak influence on $Li_{5.4}(PS_4)(S_{0.4}Cl_{1.0}Br_{0.6})$ conduction path structure [18, 19].

The all-solid-state battery using the $Li(Ni_{0.8}Co_{0.1}Mn_{1.0})O_2$ and β-Li_3PS_4 cathode (ionic conductivity: ~0.1 mS/cm) mixture showed a high capacity (120 mAh/g) without CA [50-53]. In contrast, we measured 3.1 mAh/g after 50 cycles in our all-solid-state battery using a high-ion-conductive solid electrolyte, $Li_{5.4}(PS_4)(S_{0.4}Cl_{1.0}Br_{0.6})$ (12 mS/cm), without a CA-modified cathode. Battery capacity may decrease even if the ionic or electronic conductivity of the cathode is high [54, 55], likely because the charge/discharge reaction caused by charge transfer involves both lithium-ion and electron conduction in the electrode [54, 55]. These results emphasize the importance of the electronic conductivity of the cathode mixture when optimizing battery capacity in a system incorporating a high-ion-conductive $Li_{5.4}(PS_4)(S_{0.4}Cl_{1.0}Br_{0.6})$ solid electrolyte. This high ionic conductivity is also attributed to the high discharge capacity at 0.5 C

Reprinted with permission from Journal of Solid State Electrochemistry

[54, 55]. Compared with the discharge capacity (<10 mAh/g) of the Li | β-Li_3PS_4 | $Li(Ni_{0.8}Co_{0.1}Mn_{1.0})O_2$–β-$Li_3PS_4$ battery [50], the all-solid-state battery with 5 vol% CA recorded 137 mAh/g and 134 mAh/g at the 3rd and 49th cycles, respectively. (Figure. 1 (c))

4.3.2 Impedance spectra of Li｜$Li_{5.4}(PS_4)(S_{0.4}Cl_{1.0}Br_{0.6})$ | $Li(Ni_{0.8}Co_{0.1}Mn_{0.1})O_2$–$Li_{5.4}(PS_4)(S_{0.4}Cl_{1.0}Br_{0.6})$-CA batteries

Impedance spectra are shown in Figure. 3(a)-(d). We previously reported that $Li_{5.4}(PS_4)(S_{0.4}Cl_{1.0}Br_{0.6})$ showed constant resistance at high frequency due to its high chemical stability [19]. In the present study, we found that $Li_{5.4}(PS_4)(S_{0.4}Cl_{1.0}Br_{0.6})$ was stable even at up to 10 vol% CA in the all-solid-state battery comprising Li｜$Li_{5.4}(PS_4)(S_{0.4}Cl_{1.0}Br_{0.6})$ | $Li(Ni_{0.8}Co_{0.1}Mn_{0.1})O_2$–$Li_{5.4}(PS_4)(S_{0.4}Cl_{1.0}Br_{0.6})$-CA. Table 1-4 show the impedance estimates calculated using an equivalent circuit model (Figure. 4 (a)-(d)).

Reprinted with permission from Journal of Solid State Electrochemistry

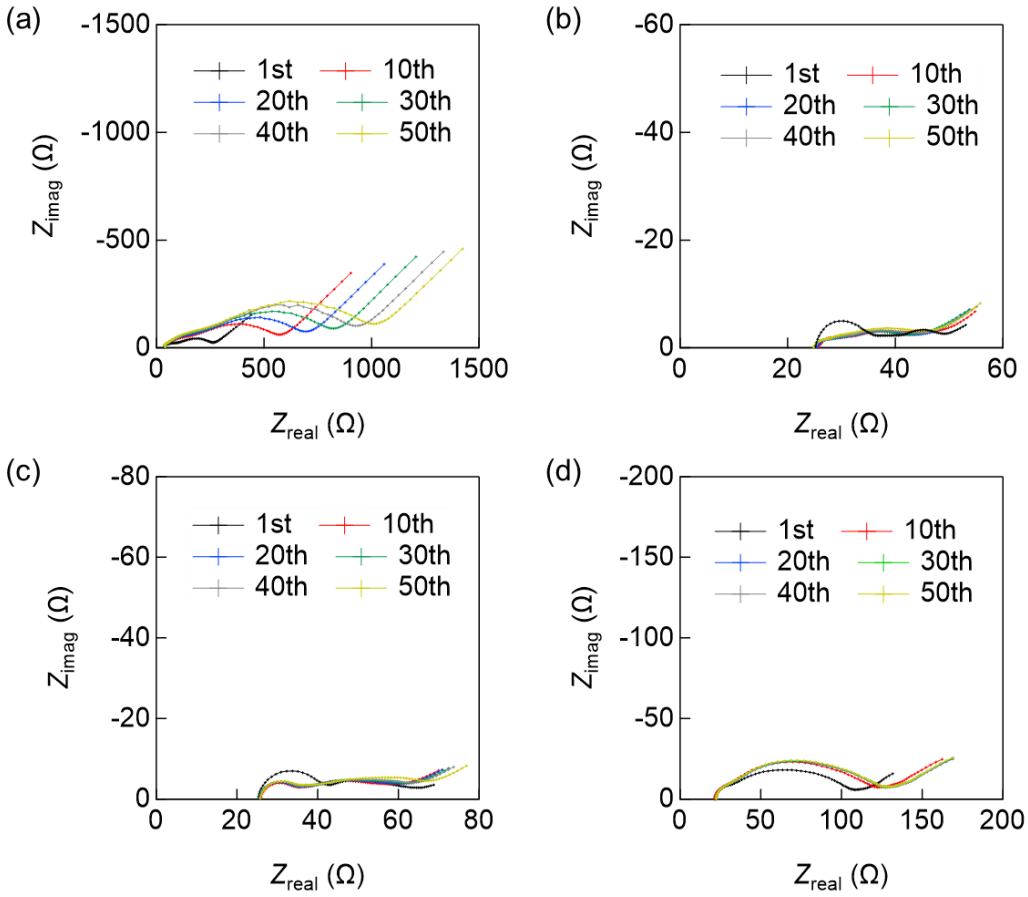

Figure. 3 Impedance spectra of battery using (a) 0 vol%, (b) 5 vol%, (c) 10 vol%, and (d) 25 vol% CA, respectively, after 50 cycles

Table 1 Equivalent circuit parameters obtained by fitting the impedance spectrum of the battery using 0 vol% CA cathode mixture

Cycle	R0 (Ω)	R1 (Ω)	T1 (F $s^{(1-\alpha1)}$)	α1	R2 (Ω)	T2 (F $s^{(1-\alpha2)}$)	α2	T3 (F $s^{0.5}$)
1^{st}	25.12	76.55	2.13×10^{-5}	0.51	164.43	1.92×10^{-4}	0.58	1.77×10^{-2}
10^{th}	25.21	212.30	4.29×10^{-5}	0.47	317.88	1.77×10^{-5}	0.67	8.64×10^{-3}
20^{th}	25.16	263.31	4.39×10^{-5}	0.46	384.57	8.59×10^{-5}	0.70	7.75×10^{-3}
30^{th}	25.15	292.23	4.10×10^{-5}	0.47	476.43	7.89×10^{-5}	0.69	7.15×10^{-3}
40^{th}	25.16	326.91	4.10×10^{-5}	0.47	546.79	7.21×10^{-5}	0.70	6.73×10^{-3}
50^{th}	25.17	343.92	4.03×10^{-5}	0.47	604.40	7.21×10^{-5}	0.70	6.56×10^{-3}

Reprinted with permission from Journal of Solid State Electrochemistry

Table 2 Equivalent circuit parameters obtained by fitting the impedance spectrum of the battery using 5 vol% CA cathode mixture

Cycle	R0 (Ω)	R1 (Ω)	T1 ($F\ s^{(1-\alpha1)}$)	α1	R2 (Ω)	T2 ($F\ s^{(1-\alpha2)}$)	α2	T3 ($F\ s^{0.5}$)
1st	25.82	9.61	2.26×10^{-6}	0.85	19.49	3.93×10^{-3}	0.40	0.403
10th	25.44	3.16	5.26×10^{-6}	0.88	20.13	5.22×10^{-3}	0.40	0.371
20th	25.35	2.15	5.87×10^{-6}	0.91	18.66	4.75×10^{-3}	0.40	0.363
30th	25.49	1.49	6.63×10^{-6}	0.99	19.58	5.92×10^{-3}	0.40	0.366
40th	24.75	2.01	3.98×10^{-6}	0.94	20.58	5.80×10^{-3}	0.40	0.351
50th	25.77	2.87	3.58×10^{-6}	0.91	23.14	4.97×10^{-3}	0.40	0.330

Table 3 Equivalent circuit parameters obtained by fitting the impedance spectrum of the battery using 10 vol% CA cathode mixture

Cycle	R0 (Ω)	R1 (Ω)	T1 ($F\ s^{(1-\alpha1)}$)	α1	R2 (Ω)	T2 ($F\ s^{(1-\alpha2)}$)	α2	T3 ($F\ s^{0.5}$)
1st	24.93	11.85	5.62×10^{-7}	1.00	26.30	5.60×10^{-3}	0.40	0.383
10th	25.43	6.98	3.34×10^{-7}	1.00	28.47	3.57×10^{-3}	0.40	0.346
20th	25.47	6.84	3.21×10^{-7}	1.00	30.55	3.85×10^{-3}	0.40	0.356
30th	25.03	7.89	3.06×10^{-7}	1.00	30.54	3.72×10^{-3}	0.40	0.356
40th	25.62	8.52	3.05×10^{-7}	1.00	31.84	4.85×10^{-3}	0.40	0.352
50th	24.91	11.80	3.42×10^{-7}	0.82	33.97	5.99×10^{-3}	0.40	0.400

Table 4 Equivalent circuit parameters obtained by fitting the impedance spectrum of the battery using 25 vol% CA cathode mixture

Cycle	R0 (Ω)	R1 (Ω)	T1 ($F\ s^{(1-\alpha1)}$)	α1	R2 (Ω)	T2 ($F\ s^{(1-\alpha2)}$)	α2	T3 ($F\ s^{0.5}$)
1st	25.00	7.48	4.40×10^{-7}	1.00	78.77	1.03×10^{-4}	0.61	0.118
10th	24.91	7.21	4.46×10^{-7}	1.00	96.09	1.22×10^{-4}	0.58	0.0725
20th	25.05	6.31	3.85×10^{-7}	1.00	97.68	1.23×10^{-4}	0.56	0.0715
30th	25.02	6.21	5.33×10^{-7}	1.00	105.64	1.21×10^{-4}	0.53	0.0729
40th	25.47	6.43	3.77×10^{-7}	1.00	99.63	1.21×10^{-4}	0.56	0.0701
50th	24.31	5.92	4.51×10^{-7}	1.00	106.24	1.39×10^{-4}	0.53	0.0713

Reprinted with permission from Journal of Solid State Electrochemistry

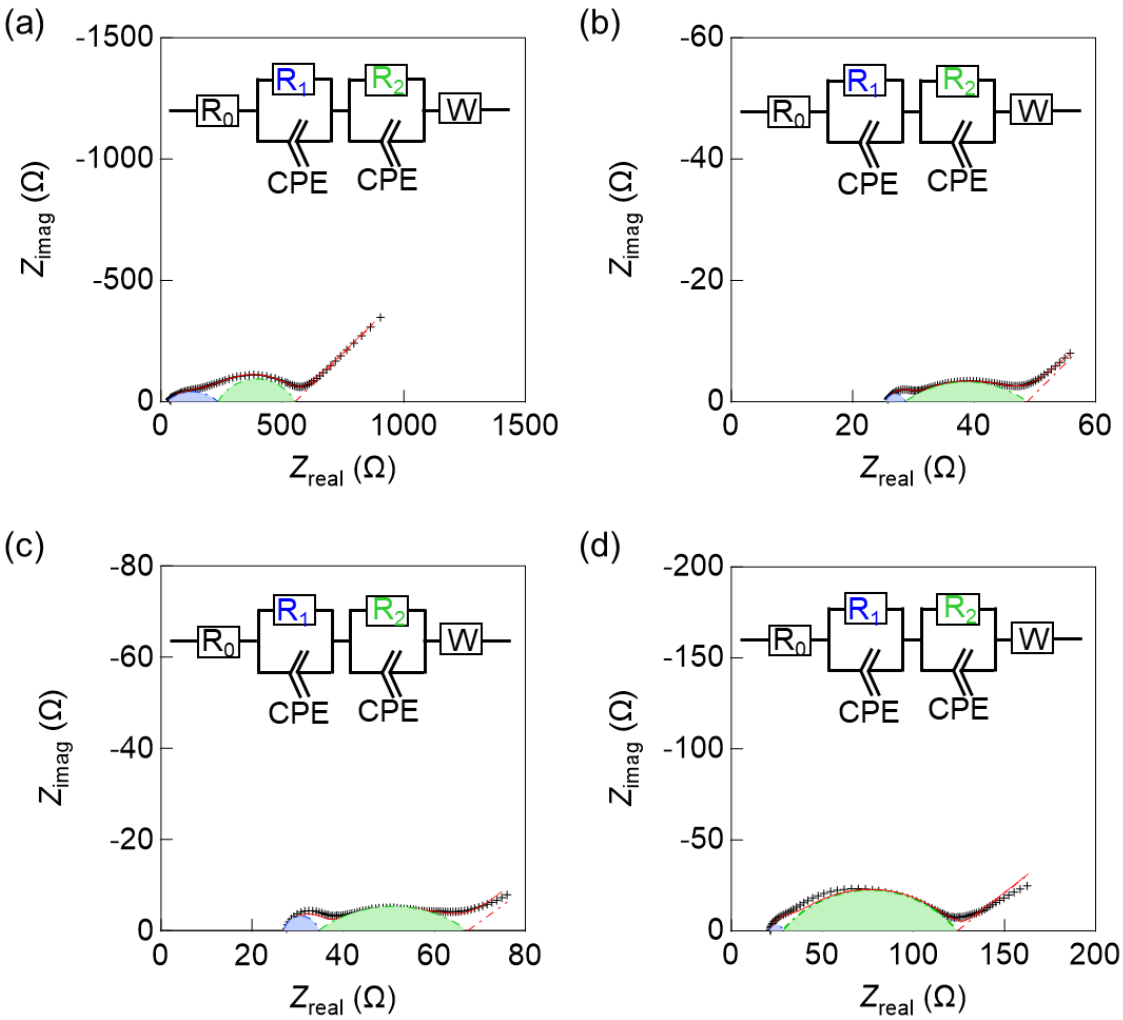

Figure. 4 Impedance spectra at the 10th cycle using (a) 0 vol%, (b) 5 vol%, (c) 10 vol%, and (d) 25 vol% CA cathode mixture fitted using the inset equivalent circuit models, as previously reported [19]. The spectra were fitted using Zmeam software [49]

In the battery using the highest-capacity 5-vol% CA cathode mixture, resistance increased from 53 to 56 Ω during 50 cycles. We previously reported that the impedance of a high-capacity battery increased from 85 to 135 Ω during 50 cycles [19], which was presumed to be due to the formation of amorphous impurities. We also found that $Li_{5.4}(PS_4)(S_{0.4}Cl_{1.0}Br_{0.6})$ was stable against Li metal [18]. $Li_{5.4}(PS_4)(S_{0.4}Cl_{1.0}Br_{0.6})$ is electrochemically stable during cycling because the calculated resistances at high

Reprinted with permission from Journal of Solid State Electrochemistry

frequency using an equivalent circuit model remained unchanged during 50 cycles (Figure. 4(a)-(d), Table 1-4). Previous results indicated that the battery using the 5 vol% CA cathode mixture was highly stable after 50 cycles.

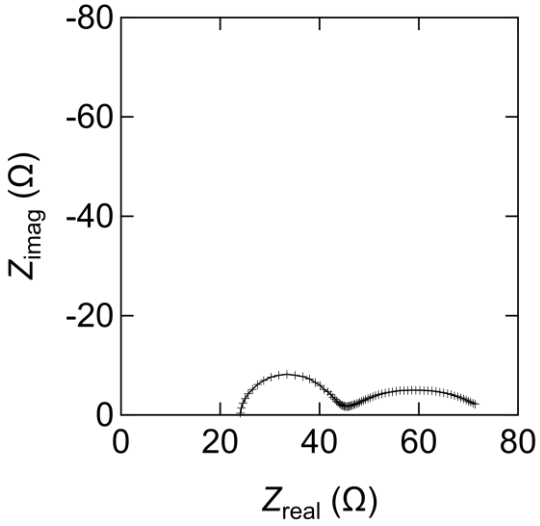

Figure. 5 Impedance spectrum of Li | $Li_{5.4}(PS_4)(S_{0.4}Cl_{1.0}Br_{0.6})$ | Li cell configuration. This cell was fabricated using the same method as an all-solid-state battery, except in replacing Li with a cathode

Assuming a homogeneous electrode, Warburg impedance can be measured at low frequencies as a finite length of material diffusion [56, 57]. In all-solid-state batteries, the Warburg coefficient reflects the ease with which lithium-ion diffuses within the electrode [58]. Warburg impedance did not appear when measuring impedance in a Li | SE | Li cell configuration after flowing a current equivalent to 50% of SOC (Figure. 5). When the Warburg coefficients were compared, it was observed that lithium-ion tended to diffuse more easily into positive electrodes incorporating 5 and 10 vol% CA-modified cathodes. In contrast, Li diffusion was limited at 0 and 25 vol% (Table 1-4), reflecting the change in capacity. Although Warburg impedance in this study is assumed to be homogeneous in cathodes, actual cathodes are composites of cathode active

Reprinted with permission from Journal of Solid State Electrochemistry

materials, solid electrolytes, and CA. In the case of a composite structure, macroscopic Li diffusion would be strongly influenced by its morphology [56, 57]. However, we did not analyze morphology-dependent changes in Li diffusion during cycling. Therefore, clarifying the relationship between cathode performance, impedance spectra, and cathode morphology will be the next step in manufacturing high-performance composite cathodes.

CA modification was previously reported to increase capacity by increasing cathode active material [$Li(Ni_{0.6}Co_{0.6}Mn_{0.6})O_2$] utilization rates. However, as the utilization rate increased, deterioration reactions at the β-Li_3PS_4/CA interface progressed, causing a decrease in capacity during cycling [23]. In this study, the utilization rate of $Li(Ni_{0.8}Co_{0.1}Mn_{0.1})O_2$ increased by adding CA, capacity decrease during cycling was small, and there was little increase in impedance, indicating limited decomposition reactions at the $Li_{5.4}(PS_4)(S_{0.4}Cl_{1.0}Br_{0.6})$/CA interface.

4.4 Conclusion

This study evaluated the discharge capacity of an all-solid-state battery with a Li｜$Li_{5.4}(PS_4)(S_{0.4}Cl_{1.0}Br_{0.6})$ | $Li(Ni_{0.8}Co_{0.1}Mn_{0.1})O_2$–$Li_{5.4}(PS_4)(S_{0.4}Cl_{1.0}Br_{0.6})$-CA structure. In conventional all-solid-state batteries, the initial capacity was high with a CA but decreased with cycling. The CA improved the electronic conductivity of the cathode mixture and increased the discharge capacity from 3.1 to 167 mAh/g after 50 cycles. The resistance of the battery increased from 53 to 56 Ω during 50 charge/discharge cycles. These findings demonstrate that the battery capacity of an all-solid-state battery employing a high-ionic conductive $Li_{5.4}(PS_4)(S_{0.4}Cl_{1.0}Br_{0.6})$ can be increased with a CA modification that enhances the electronic conductivity of the cathode. This study

Reprinted with permission from Journal of Solid State Electrochemistry

presents a proven framework for developing an all-solid-state battery comprising halogen-rich argyrodite ($Li_{7-\alpha}(PS_4)(S_{2-\alpha}X_\alpha)$; $\alpha > 1$) with enhanced ionic conductivities by controlling the electronic conductivity of the cathode. We plan to further improve battery performance by elucidating the relationship between the battery performance, actual cathode structure, and impedance during cycling in a future study.

4.5 References

1. Jacobson MZ (2009) Review of solutions to global warming, air pollution, and energy security. Energy Environ Sci 2:148–173. https://doi.org/10.1039/B809990C

2. Hannan MA, Lipu MSH, Hussain A, Mohamed A (2017) A review of lithium-ion battery state of charge estimation and management system in electric vehicle applications: Challenges and recommendations. Renew Sustain Energy Rev 78:834–854. https://doi.org/10.1016/j.rser.2017.05.001

3. Janek J, Zeier WG (2016) A solid future for battery development. Nat Energy 1:16141. https://doi.org/10.1038/nenergy.2016.141

4. Kato Y, Hori S, Saito T, Suzuki K, Hirayama M, Mitsui A, Yonemura M, Iba H, Kanno R (2016) High-power all-solid-state batteries using sulfide superionic conductors. Nat Energy 1:16030. https://doi.org/10.1038/nenergy.2016.30

5. Boulineau S, Tarascon JM, Leriche JB, Viallet V (2013) Electrochemical properties of all-solid-state lithium secondary batteries using Li-argyrodite Li_6PS_5Cl as solid electrolyte. Solid State Ionics 242:45–48. https://doi.org/10.1016/j.ssi.2013.04.012

6. Wang P, Liu H, Patel S, Feng X, Chien P-H, Wang Y, Hu YY (2020) Fast ion conduction and its origin in $Li_{6-x}PS_{5-x}Br_{1+x}$. Chem Mater 32:3833–3840. https://doi.org/10.1021/acs.chemmater.9b05331

Reprinted with permission from Journal of Solid State Electrochemistry

7. Feng X, Chien P-H, Wang Y, Patel S, Wang P, Liu H, Immediato-Scuotto M, Hu YY (2020) Enhanced ion conduction by enforcing structural disorder in Li-deficient argyrodites $Li_{6-x}PS_{5-x}Cl_{1+x}$. Energy Stor Mater 30:67–73. https://doi.org/10.1016/j.ensm.2020.04.042

8. Adeli P, Bazak JD, Park KH, Kochetkov I, Huq A, Goward GR, Nazar LF (2019) Boosting solid-state diffusivity and conductivity in lithium superionic argyrodites by halide substitution. Angew Chem Int Ed Engl 58:8681–8686. https://doi.org/10.1002/anie.201814222

9. Adeli P, Bazak JD, Huq A, Goward GR, Nazar LF (2021) Influence of aliovalent cation substitution and mechanical compression on Li-ion conductivity and diffusivity in argyrodite solid electrolytes. Chem Mater 33:146–157. https://doi.org/10.1021/acs.chemmater.0c03090

10. Suyama M, Kato A, Sakuda A, Hayashi A, Tatsumisago M (2018) Lithium dissolution/deposition behavior with Li_3PS_4-LiI electrolyte for all-solid-state batteries operating at high temperatures. Electrochim Acta 286:158–162. https://doi.org/10.1016/j.electacta.2018.07.227

11. Epp V, Gün Ö, Deiseroth HJ, Wilkening M (2013) Highly mobile ions: Low-temperature NMR directly probes extremely fast Li^+ hopping in argyrodite-type Li_6PS_5Br. J Phys Chem Lett 4:2118–2123. https://doi.org/10.1021/jz401003a

12. Gautam A, Sadowski M, Ghidiu M, Minafra N, Senyshyn A, Albe K, Zeier WG (2021) Engineering the site-disorder and lithium distribution in the lithium superionic argyrodite Li_6PS_5Br. Adv Energy Mater 11:2003369. https://doi.org/10.1002/aenm.202003369

13. Patel SV, Banerjee S, Liu H, Wang P, Chien PH, Feng X, Liu J, Ong SP, Hu YY

Reprinted with permission from Journal of Solid State Electrochemistry

(2021) Tunable lithium-ion transport in mixed-halide argyrodites $Li_{6-x}PS_{5-x}ClBr_x$: An unusual compositional space. Chem Mater 33:1435–1443. https://doi.org/10.1021/acs.chemmater.0c04650

14. De Klerk NJJ, Rosłoń I, Wagemaker M (2016) Diffusion mechanism of Li argyrodite solid electrolytes for Li-ion batteries and prediction of optimized halogen doping: The effect of Li vacancies, halogens, and halogen disorder. Chem Mater 28:7955–7963. https://doi.org/10.1021/acs.chemmater.6b03630

15. Kraft MA, Culver SP, Calderon M, Böcher F, Krauskopf T, Senyshyn A, Dietrich C, Zevalkink A, Janek J, Zeier WG (2017) Influence of lattice polarizability on the ionic conductivity in the lithium superionic argyrodites Li_6PS_5 X (X = Cl, Br, I). J Am Chem Soc 139:10909–10918. https://doi.org/10.1021/jacs.7b06327

16. Yu C, Li Y, Li W, Adair KR, Zhao F, Willans M, Liang J, Zhao Y, Wang C, Deng S, Li R, Huang H, Lu S, Sham TK, Huang Y, Sun X (2020) Enabling ultrafast ionic conductivity in Br-based lithium argyrodite electrolytes for solid-state batteries with different anodes. Energy Stor Mater 30:238–249. https://doi.org/10.1016/j.ensm.2020.04.014

17. Subramanian Y, Rajagopal R, Ryu KS (2022) Synthesis, air stability and electrochemical investigation of lithium superionic bromine substituted argyrodite ($Li_{6-x}PS_{5-x}Cl_{1.0}Br_x$) for all-solid-state lithium batteries. J Power Sources 520:230849. https://doi.org/10.1016/j.jpowsour.2021.230849

18. Masuda N, Kobayashi K, Utsuno F, Uchikoshi T, Kuwata N (2022) Effects of halogen and sulfur mixing on lithium-ion conductivity in $Li_{7-x-y}(PS_4)(S_{2-x-y}Cl_xBr_y)$ argyrodite and mechanism for enhanced lithium conduction. J Phys Chem C 126:14067–14074. https://doi.org/10.1021/acs.jpcc.2c03780

Reprinted with permission from Journal of Solid State Electrochemistry

19. Masuda N, Kobayashi K, Utsuno F, Uchikoshi T, Kuwata N (2023) Electrochemical stability of $Li_{5.4}(PS_4)(S_{0.4}Cl_{1.0}Br_{0.6})$ in an all-solid-state battery comprising $LiNbO_3$-coated $Li(Ni_{0.8}Co_{0.1}Mn_{0.1})O_2$ cathode and lithium metal anode. J Electrochem Soc 170:090529. https://doi.org/10.1149/1945-7111/acf880

20. Yubuchi S, Uematsu M, Hotehama C, Sakuda A, Hayashi A, Tatsumisago M (2019) An argyrodite sulfide-based superionic conductor synthesized by a liquid-phase technique with tetrahydrofuran and ethanol. J Mater Chem A 7:558–566. https://doi.org/10.1039/C8TA09477B

21. Park SW, Oh G, Park JW, Ha YC, Lee SM, Toon SY, Kim BG (2019) Graphitic hollow nanocarbon as a promising conducting agent for solid-state lithium batteries. Small 15:1900235. https://doi.org/10.1039/C8TA09477B

22. Wang CW, Ren FC, Zhou Y, Yan PF, Zhou XD, Zhang SJ, Liu W, Zhang WD, Zou MH, Zeng LY, Yao XY, Huang L, Li JT, Sun SG (2021) Engineering the interface between $LiCoO_2$ and $Li_{10}GeP_2S_{12}$ solid electrolytes with an ultrathin $Li_2CoTi_3O_8$ interlayer to boost the performance of all-solid-state batteries. Energy Environ Sci 14:437–450. https://doi.org/10.1039/D0EE03212C

23. Walther F, Randau S, Schneider Y, Sann J, Rohnke M, Richter FH, Zeier WG, Janek J (2020) Influence of carbon additives on the decomposition pathways in cathodes of lithium thiophosphate-based all-solid-state batteries. Chem Mater 32:6123–6136. https://doi.org/10.1021/acs.chemmater.0c01825

24. Randau S, Walther F, Neumann A, Schneider Y, Negi RS, Mogwitz B, Sann J, Becker-Steinberger K, Danner T, Hein S, Latz A, Richter FH, Janek J (2021) On the additive microstructure in composite cathodes and alumina-coated carbon microwires for improved all-solid-state batteries. Chem Mater 33:1380–1393.

Reprinted with permission from Journal of Solid State Electrochemistry

https://doi.org/10.1021/acs.chemmater.0c04454

25. Walther F, Strauss F, Wu X, Mogwitz B, Hertle J, Sann J, Rohnke M, Brezesinski T, Janek J (2021) The working principle of a Li_2CO_3/$LiNbO_3$ coating on NCM for thiophosphate-based all-solid-state batteries. Chem Mater 33:2110–2125. https://doi.org/10.1021/acs.chemmater.0c04660

26. Kitsche D, Tang Y, Ma Y, Goonetilleke D, Sann J, Walther F, Bianchini M, Janek J, Brezesinski T (2021) High performance all-solid-state batteries with a Ni-Rich NCM cathode coated by atomic layer deposition and lithium thiophosphate solid electrolyte. ACS Appl Energy Mater 4:7338–7345. https://doi.org/10.1021/acsaem.1c01487

27. Choi JH, Choi S, Embleton TJ, Ko K, Saqib KS, Ali J, Jo M, Hwang J, Park S, Kim M, Hwang M, Lim H, Oh P (2023) The effect of conductive additive morphology and crystallinity on the electrochemical performance of Ni-Rich cathodes for sulfide all-solid-state lithium-ion batteries. Nanomaterials (Basel) 13:3065. https://doi.org/10.3390/nano13233065

28. Lee KJ, Byeon YW, Lee HJ, Lee Y, Park S, Kim HR, Kim HK, Oh SJ, Ahn JP (2023) Revealing crack-healing mechanism of NCM composite cathode for sustainable cyclability of sulfide-based solid-state batteries. Energy Storage Mater 57:326–333. https://doi.org/10.1016/j.ensm.2023.01.012

29. Cangaz S, Hippauf F, Reuter FS, Doerfler S, Abendroth T, Althues H, Kaskel S (2020) Enabling high-energy solid-state batteries with stable anode interphase by the use of columnar silicon anodes. Adv Energy Mater 10:2001320. https://doi.org/10.1002/aenm.202001320

30. Li Y, Wu Y, Ma T, Wang Z, Gao Q, Xu J, Chen L, Li H, Wu F (2022) Long-life sulfide all-solid-state battery enabled by substrate-modulated dry-process binder. Adv

Reprinted with permission from Journal of Solid State Electrochemistry

Energy Mater 12:2001732. https://doi.org/10.1002/aenm.202201732

31. Minnmann P, Quillman L, Burkhardt S, Richter FH, Janek J (2021) Editors' Choice—Quantifying the impact of charge transport bottlenecks in composite cathodes of all-solid-state batteries. J Electrochem Soc 168:040537. https://doi.org/10.1149/1945-7111/abf8d7

32. Ann J, Choi S, Do J, Lim S, Shin D (2018) Effects of binary conductive additives on electrochemical performance of a sheet-type composite cathode with different weight ratios of $LiNi_{0.6}Co_{0.2}Mn_{0.2}O_2$ in all-solid-state lithium batteries. J Ceram Process Res 19:413

33. Poetke S, Hippauf F, Baasner A, Dörfler S, Althues H, Kaskel S (2021) Nanostructured Si−C composites as high-capacity anode material for all-solid-state lithium-ion batteries. Batteries Supercaps 4:1323–1334. https://doi.org/10.1002/batt.202100055

34. Jun S, Nam YJ, Kwak H, Kim KT, Oh DY, Jung YS (2020) Operando differential electrochemical pressiometry for probing electrochemo-mechanics in all-solid-state batteries. Adv Funct Mater 30:2002535. https://doi.org/10.1002/adfm.202002535

35. Fang R, Liu Y, Li Y, Manthiram A, Goodenough JB (2023) Achieving stable all-solid-state lithium-metal batteries by tuning the cathode-electrolyte interface and ionic/electronic transport within the cathode. Mater Today 64:52–60. https://doi.org/10.1016/j.mattod.2023.03.001

36. Kim KT, Woo J, Kim YS, Sung S, Park C, Lee C, Park YJ, Lee HW, Park K, Jung YS (2023) Ultrathin superhydrophobic coatings for air-stable inorganic solid electrolytes: toward dry room application for all-solid-state batteries. Adv Energy Mater 13:2301600. https://doi.org/10.1002/aenm.202301600

Reprinted with permission from Journal of Solid State Electrochemistry

37. Tan DHS, Wu EA, Nguyen H, Chen Z, Marple MAT, Doux JM, Wang X, Yang H, Banerjee A, Meng YS (2019) The detrimental effects of carbon additives in $Li_{10}GeP_2S_{12}$-based solid-state batteries. ACS Energy Lett 4:2418–2427. https://doi.org/10.1021/acsenergylett.9b01693

38. Zhang W, Leichtweiß T, Culver SP, Koerver R, Das D, Weber DA, Zeier WG, Janek J (2017) The detrimental effects of carbon additives in Li10GeP2S12-based solid-state batteries. ACS Appl Mater Interfaces 9:35888–35896. https://doi.org/10.1021/acsami.7b11530

39. Teo JH, Strauss F, Tripkovi Đ, Schweidler S, Ma Y, Bianchini M, Janek J, Brezesinski T (2021) Design-of-experiments-guided optimization of slurry-cast cathodes for solid-state batteries. Cell Rep Physiol Sci 2:100465. https://doi.org/10.1016/j.xcrp.2021.100465

40. Yamamoto M, Terauchi Y, Sakuda A, Takahashi M (2018) Slurry mixing for fabricating silicon-composite electrodes in all-solid-state batteries with high areal capacity and cycling stability. J Power Sources 402:506–512. https://doi.org/10.1016/j.jpowsour.2018.09.070

41. Kim AY, Strauss F, Bartsch T, Teo JH, Janek J, Brezesinski T (2021) Effect of surface carbonates on the cyclability of $LiNbO_3$-coated NCM622 in all-solid-state batteries with lithium thiophosphate electrolytes. Sci Rep 11:5367. https://doi.org/10.1038/s41598-021-84799-1

42. Embleton TJ, Yun J, Choi JH, Kim J, Ko K, Kim J, Son Y, Oh P (2023) Lithium-enhanced functionalized carbon nanofibers as a mixed electronic/ionic conductor for sulfide all solid-state batteries. Appl Surf Sci 610:155490. https://doi.org/10.1016/j.apsusc.2022.155490

Reprinted with permission from Journal of Solid State Electrochemistry

43. Swamy T, Chen X, Chiang YM (2019) Electrochemical redox behavior of Li ion conducting sulfide solid electrolytes. Chem Mater 31:707–713. https://doi.org/10.1021/acs.chemmater.8b03420

44. Hakari T, Deguchi M, Mitsuhara K, Ohta T, Saito K, Orikasa Y, Uchimoto Y, Kowada Y, Hayashi A, Tatsumisago M (2017) Structural and electronic-state changes of a sulfide solid electrolyte during the Li deinsertion–insertion processes. Chem Mater 29:4768–4774. https://doi.org/10.1021/acs.chemmater.7b00551

45. Rossman RP, Smith WR (1943) Density of carbon black by helium displacement. Ind Eng Chem 35:972–976. https://doi.org/10.1021/ie50405a008

46. Ohta N, Takada K, Sakaguchi I, Zhang L, Ma R, Fukuda K, Osada M, Sasaki T (2007) $LiNbO_3$-coated $LiCoO_2$ as cathode material for all solid-state lithium secondary batteries. Electrochem Commun 9:1486–1490. https://doi.org/10.1016/j.elecom.2007.02.008

47. Gao X, Liu B, Hu B, Ning Z, Jolly DS, Zhang S, Perera J, Bu J, Liu J, Doerrer C, Darnbrough E, Armstrong D, Grant PS, Bruce PG (2022) Solid-state lithium battery cathodes operating at low pressures. Joule 6:636–646. https://doi.org/10.1016/j.joule.2022.02.008

48. Walther F, Koerver R, Fuchs T, Ohno S, Sann J, Rohnke M, Zeier WG, Janek J (2019) Visualization of the interfacial decomposition of composite cathodes in argyrodite-based all-solid-state batteries using time-of-flight secondary-ion mass spectrometry. Chem Mater 31:3745–3755. https://doi.org/10.1021/acs.chemmater.9b00770

49. Kobayashi K, Sakka Y, Suzuki TS (2016) Development of an electrochemical impedance analysis program based on the expanded measurement model. J Ceram Soc

Reprinted with permission from Journal of Solid State Electrochemistry

Jpn 124:943–949. https://doi.org/10.2109/jcersj2.16120

50. Koerver R, Aygün I, Leichtweiß T, Dietrich C, Zhang W, Binder JO, Hartmann P, Zeier WG, Janek J (2017) Capacity fade in solid-state batteries: Interphase formation and chemomechanical processes in nickel-rich layered oxide cathodes and lithium thiophosphate solid electrolytes. Chem Mater 29:5574–5582. https://doi.org/10.1021/acs.chemmater.7b00931

51. Tachez M, Malugani JP, Mercier R, Robert G (1984) Ionic conductivity of and phase transition in lithium thiophosphate Li_3PS_4. Solid State Ion 14:181–185. https://doi.org/10.1016/0167-2738(84)90097-3

52. Liu Z, Fu W, Payzant EA, Yu X, Wu Z, Dudney NJ, Kiggans J, Hong K, Rondinone AJ, Liang C (2013) Anomalous high ionic conductivity of nanoporous β-Li_3PS_4. J Am Chem Soc 135:975–978. https://doi.org/10.1021/ja3110895

53. Marchini F, Porcheron B, Rousse G, Albero Blanquer LA, Droguet L, Foix D, Koç T, Deschamps M, Tarascon JM (2021) The hidden side of nanoporous β-Li_3PS_4 solid electrolyte. Adv Energy Mater 11:2101111. https://doi.org/10.1002/aenm.202101111

54. Hayakawa E, Nakamura H, Ohsaki S, Watano S (2022) Characterization of solid-electrolyte/active-material composite particles with different surface morphologies for all-solid-state batteries. Adv Powder Technol 33:103470. https://doi.org/10.1016/j.apt.2022.103470

55. Hayakawa E, Nakamura H, Ohsaki S, Watano S (2022) Dry mixing of cathode composite powder for all-solid-state batteries using a high-shear mixer. Adv Powder Technol 33:103705. https://doi.org/10.1016/j.apt.2022.103705

56. Kobayashi K, Terabe K, Sukigara T, Sakka Y (2013) Theoretical modeling of electrode impedance for an oxygen ion conductor and metallic electrode system based

Reprinted with permission from Journal of Solid State Electrochemistry

on the interfacial conductivity theory. Part II: Case of the limiting process by non steady-state surface diffusion. Solid State Ion 249–250:78–85. http://doi.org/10.1016/j.ssi.2013.07.022

57. Min YJ, Lee GE, Seong JY, Shin HC (2023) Advanced electrochemical analysis of all-solid-state battery electrodes using novel potential-controllable symmetric cell. Electrochim Acta 468:143154. https://doi.org/10.1016/j.electacta.2023.143154

58. Zhang J, Zheng C, Li L, Xia Y, Huang H, Gan Y, Liang C, He X, Tao X, Zhang W (2020) Unraveling the intra and intercycle interfacial evolution of Li6PS5Cl-based all-solid-state lithium batteries. Adv Energy Mater 10:1903311. https://doi.org/10.1002/aenm.201903311

Reprinted with permission from Journal of Solid State Electrochemistry

5. General conclusions

In this thesis, the crystal structure and lithium conduction path of novel halogen-rich argyrodite $Li_{5.4}(PS_4)(S_{0.4}Cl_{1.0}Br_{0.6})$ in a ternary system, $Li_7(PS_4)(S_2)$–$Li_5(PS_4)(Cl_2)$–$Li_5(PS_4)(Br_2)$, with high ionic conductivity were investigated and examined the stability of $Li_{5.4}(PS_4)(S_{0.4}Cl_{1.0}Br_{0.6})$ as a solid electrolyte for all-solid-state batteries. In addition, the enhanced discharge capacity of Li ｜ $Li_{5.4}(PS_4)(S_{0.4}Cl_{1.0}Br_{0.6})$ | $Li(Ni_{0.8}Co_{0.1}Mn_{0.1})O_2$–$Li_{5.4}(PS_4)(S_{0.4}Cl_{1.0}Br_{0.6})$ was examined. The following results and considerations were obtained.

1. There are the optimum compositions of $Li_{7-x-y}(PS_4)(S_{2-x-y}Cl_xBr_y)$ to obtain a high lithium-ion conductivity when ($x + y = 1.6$) because impurity was not formed and Li site vacancy promoted ionic conductivity. The highest conductivity was obtained when $x = 0.6$–1.0 ($y = 0.6$–1.0) in $Li_{7-x-y}(PS_4)(S_{2-x-y}Cl_xBr_y)$.
2. The crystal structure of novel halogen-rich argyrodite was elucidated combining the Rietveld refinement of Synchrotron XRD, neutron diffraction, ICP and ^{31}P NMR. For the anion composition, bigger anions preferably occupy 4a site and smaller anions occupy 4d site. The vacant space around 4a site is bigger than 4d site. This is derived from the space size around 4a site and 4d site. For the lithium existing site, the existence of the 16e site has been revealed, in addition to the previously reported 48h, 48h’ and 24g sites.
3. The study also revealed that the 48h′–48h′ (T2–T2) is not the path for the inter-cage conduction in the halogen-rich $Li_{7-x-y}(PS_4)(S_{2-x-y}Cl_xBr_y)$ with ($x + y > 1$); instead, it is the 48h–16e–48h conduction path that is used because the 48h site shows the greatest occupancy. This result was supported by the combined BVS and MEM

calculations. This is the first study to propose such a difference in the inter-cage conduction path of halogen-rich argyrodite. This difference in the conduction path comes from the existence of 16e site.

4. The electrochemical stability of a investigated solid electrolyte, $Li_{5.4}(PS_4)(S_{0.4}Cl_{1.0}Br_{0.6})$, against Li metal was confirmed by prolonged stripping/plating in symmetric cells. The $Li_{5.4}(PS_4)(S_{0.4}Cl_{1.0}Br_{0.6})$ also has high stability within the applied voltage window (0 - 10V).
5. The electrochemical stability of a investigated solid electrolyte, $Li_{5.4}(PS_4)(S_{0.4}Cl_{1.0}Br_{0.6})$, mixed with the $Li(Ni_{0.8}Co_{0.1}Mn_{0.1})O_2$ cathode active material was evaluated for an all-solid-state battery with a Li | $Li_{5.4}(PS_4)(S_{0.4}Cl_{1.0}Br_{0.6})$ | $Li(Ni_{0.8}Co_{0.1}Mn_{0.1})O_2$–$Li_{5.4}(PS_4)(S_{0.4}Cl_{1.0}Br_{0.6})$ structure. At a high frequency of ~10^6 Hz, the resistance of the solid electrolyte remained unchanged during 50 charge/discharge cycles. No evidence of the formation of crystalline byproducts was observed in the XRD patterns of any cathode mixtures from the all-solid-state batteries after 50 cycles. These results demonstrate the superior stability of $Li_{5.4}(PS_4)(S_{0.4}Cl_{1.0}Br_{0.6})$ against $Li(Ni_{0.8}Co_{0.1}Mn_{0.1})O_2$ for all tested cathode compositions.
6. The discharge capacity of an all-solid-state battery with a Li | $Li_{5.4}(PS_4)(S_{0.4}Cl_{1.0}Br_{0.6})$ | $Li(Ni_{0.8}Co_{0.1}Mn_{0.1})O_2$–$Li_{5.4}(PS_4)(S_{0.4}Cl_{1.0}Br_{0.6})$ was enhanced by CA modification to the cathode. In conventional all-solid-state batteries, the initial capacity was high with a CA but decreased with cycling. The CA improved the electronic conductivity of the cathode mixture and increased the discharge capacity from 3.1 to 167 mAh/g after 50 cycles. The resistance of the battery increased from 53 to 56 Ω during 50 charge/discharge cycles. These findings

demonstrate that the battery capacity of an all-solid-state battery employing a high-ionic conductive $Li_{5.4}(PS_4)(S_{0.4}Cl_{1.0}Br_{0.6})$ can be increased with a CA modification that enhances the electronic conductivity of the cathode.

These results revealed that the crystal structure and lithium conducting path of novel $Li_{5.4}(PS_4)(S_{0.4}Cl_{1.0}Br_{0.6})$ and the high stability of $Li_{5.4}(PS_4)(S_{0.4}Cl_{1.0}Br_{0.6})$ in all-solid-state batteries. It has also proved that the discharge capacity of all-solid-state batteries using $Li_{5.4}(PS_4)(S_{0.4}Cl_{1.0}Br_{0.6})$ can be enhanced with CA modification to the cathode. Therefore, halogen-rich ($Li_{7-\alpha}(PS_4)(S_{2-\alpha}X_\alpha)$; $\alpha > 1$) is considered as a candidate solid electrolyte for the all-solid-state battery with enhanced discharge capacity.

These studies present a fundamental understanding of crystal structure and lithium conduction path of ($Li_{7-\alpha}(PS_4)(S_{2-\alpha}X_\alpha)$; $\alpha > 1$). These studies also presents a proven framework for developing an all-solid-state battery comprising halogen-rich argyrodite ($Li_{7-\alpha}(PS_4)(S_{2-\alpha}X_\alpha)$; $\alpha > 1$) with enhanced ionic conductivities. The present study must contribute to further development of all-solid-state batteries.

Acknowledgements

I would like to express my greatest appreciation to Professor Naoaki Kuwata of Hokkaido University and Professor Kiyoshi Kobayashi of National Institute for Materials Science for their insightful suggestions and discussion, and continuous encouragement during the course of this study.

I am grateful to Professor Hiroshi Kageyama of Kyoto University, Associate Professor Yoji Kobayashi of King Abdullah University of Science and Technology, Professor Tassel Cédric of Institute of Condensed Matter Chemistry of Bordeaux, Associate Professor Takafumi Yamamoto of Institute of Science Tokyo and Associate Professor Ryo Horikoshi of Osaka Sangyo University for their insightful discussion and suggestions of the crystal chemistry and mixed anion compounds.

I am deeply fortunate to give valuable advice of Rietveld refinement and maximum entropy method analysis from Associate Professor Olivier Hernandez of University of Rennes 1.

I would like to thank Idemitsu Kosan Co., Ltd for financial support and also thank Mr. Atsushi Yao, Mr. Hiroshi Yamaguchi, Dr. Nobuhito Nakaya, Dr. Toshiaki Kusaba, Mr. Toru Sukigara, Dr. Takeshi Makino, Mr. Tokuaki Miwa, Mr. Masahiro Sekiguchi, Mr. Hiroyuki Tamura, Mr. Yoshikazu Tanaka, Ms. Komachi Hirano, Mr. Makoto Onoda, Dr. Hiroyuki Higuchi and Dr. Futoshi Utsuno and other co-workers of Idemitsu Kosan Co., Ltd for valuable discussion and supports.

Finally, I want to thank my family for their immeasurable support and encouragement.

List of publications

Original articles regarding this study are as follows:

1. “Effects of halogen and sulfur mixing on lithium-ion conductivity in $Li_{7-x-y}(PS_4)(S_{2-x-y}Cl_xBr_y)$ argyrodite and mechanism for enhanced lithium conduction”
   N. Masuda, K. Kobayashi, F. Utsuno, T. Uchikoshi, N. Kuwata, *J. Phys. Chem. C*, **126**, 14067, (2022).
   (Chapter2)

2. “Electrochemical Stability of $Li_{5.4}(PS_4)(S_{0.4}Cl_{1.0}Br_{0.6})$ in All-Solid-State Battery Comprising $LiNbO_3$-Coated $Li(Ni_{0.8}Co_{0.1}Mn_{0.1})O_2$ Cathode and Lithium Metal Anode”
   N. Masuda, K. Kobayashi, F. Utsuno, N. Kuwata, *J. Electrochem. Soc.* **170**, 090529. (2023).
   (Chapter3)

3. “Enhanced Capacity of All-Solid-State Battery Comprising $LiNbO_3$-Coated $Li(Ni_{0.8}Co_{0.1}Mn_{0.1})O_2$ Cathode, $Li_{5.4}(PS_4)(S_{0.4}Cl_{1.0}Br_{0.6})$ Solid Electrolyte and Lithium Metal Anode”
   N. Masuda, K. Kobayashi, F. Utsuno, N. Kuwata, J. Solid State Electrochem. **28**, 4409, (2024).
   (Chapter4)